N00014-96-1-0024

MONOLITHICALLY INTEGRATED TRANSMITTERS FOR 1.5μm OPTICAL COMMUNICATION APPLICATIONS

TECHNICAL REPORT NO. SSEL-274

1997

By

Yahsing Yuan

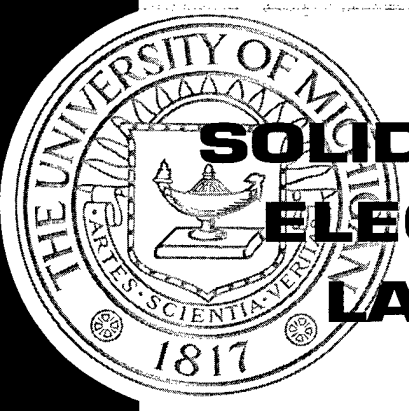

SOLID-STATE ELECTRONICS LABORATORY

DEPARTMENT OF ELECTRICAL ENGINEERING
AND COMPUTER SCIENCE
THE UNIVERSITY OF MICHIGAN, ANN ARBOR

This report has also been submitted as a dissertation in partial fulfillment of the requirements for the degree of Doctor of Philosophy in the University of Michigan, 1997.

TABLE OF CONTENTS

LIST OF FIGURES

Figure

CHAPTER I

INTRODUCTION AND OVERVIEW

1.1 Forward

Multimedia services, cable and antenna television (CATV), high definition television (HDTV), and computer links have ushered into every aspect of our lives and have become virtually indispensible. Large amounts of data transmission through the information highway have and will indoubtedly continue to benefit us by improving the way of life. The demands on a network which can accommodate the entire communication traffic in a cost effective manner have drawn considerable attention and tremendous effort has been exerted on this issue. Single-mode optical fibers widely deployed in today's telecommunication networks have the potential to carry 30 Tb/s. However, it is largely underutilized by even the most dense telecommunication system (2.5 Gb/s) commercially available at the present time [1],[2]. Unlike traditional time-division-multiplexing (TDM) techniques, wavelength division multiplexing (WDM) techniques offer a cost effective utilization of the fiber bandwidth directly in the wavelength domain, rather than in the time domain. Furthermore, the wavelengths can be used to perform functions as routing and switching [3], which are attractive for realization of all-optical transparent network layers in the future networks [4].

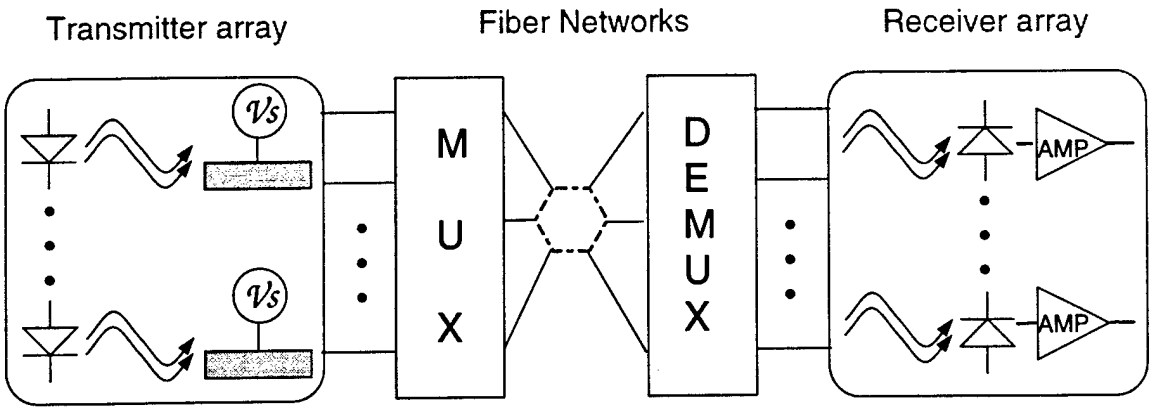

Figure 1.1: Optical communication systems architecture.

At this stage, there are still a lot of obstacles to be overcome before all-optical WDM networks can be put into practical applications. On the other hand, due to the maturity of present electronics and optoelectronics technology, WDM realized by wavelength (O/E–E/O) conversion, potentially with $\leq$ 100 Gb/s bandwidth, is still feasible and is being investigated for immediate deployment [2].

This thesis is concerned primarily with the development of high performance light sources and integrated transmitters suitable for WDM applications. A typical transmitter in a modern communication system, shown in Fig.1.1, consists of a light source, such as light-emitting diode (LED) or laser diode (LD), modulation switches , e.g. modulators, and peripheral driving and control circuits. For long distance communication apllications, laser diodes are required to overcome fiber dispersion. The monolithical integration of a laser, modulator, and driving circuits on the same chip is a compact and cost-effective method of realizing an effective transmitter.

1.2 Wavelengths of Interest

Single-mode optical fibers have become the most important propagation medium to transmit information in the modern communication systems. Information carrying capability of a communication link is characterized by (1) the transmission rate and (2) the maximum transmission distance. The bandwidth-distance product is therefore used as a figure of merit to evaluate the performance of a communication link [5].

In general, there is a trade-off between bandwidth and distance in designing a system and this relation can be approximately expressed as

$$DL\Delta\lambda \leq \frac{1}{2f}, \tag{1.1}$$

$$D = \frac{d(1/v_g)}{d\lambda} \tag{1.2}$$

where D is the dispersion parameter, L is the transmission distance, $\Delta\lambda$ is the light source linewidth, f is the transmission rate, v_g is the group velocity, and λ is the light source wavelength. Fig. 1.2 [7] shows a typical fiber loss curve and the dispersion spectrum of typical fibers is shown in Fig.1.3 [8]. It may be noted that there are windows at 1.3μm and 1.5μm in which the lowest losses are located and, hence, those are the regions where the highest performance systems operate. In addition, as the erbium-doped fiber amplifier (EDFA) becomes practical [6], pumping lasers at 0.98μm have emerged as important devices. Light sources at these wavelengths constitue the essential elements in modern long-haul optical communication systems.

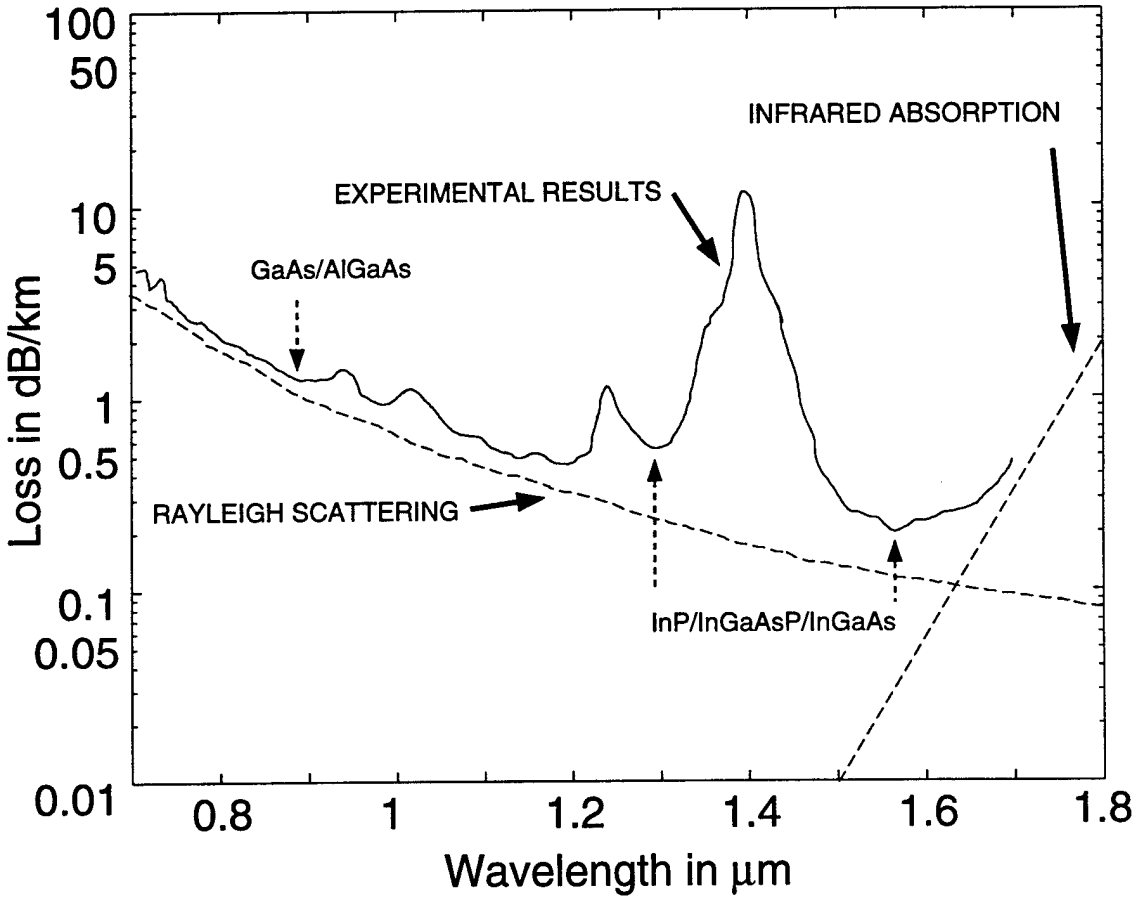

Figure 1.2: Measured loss spectrum of a typical single-mode silica fiber.

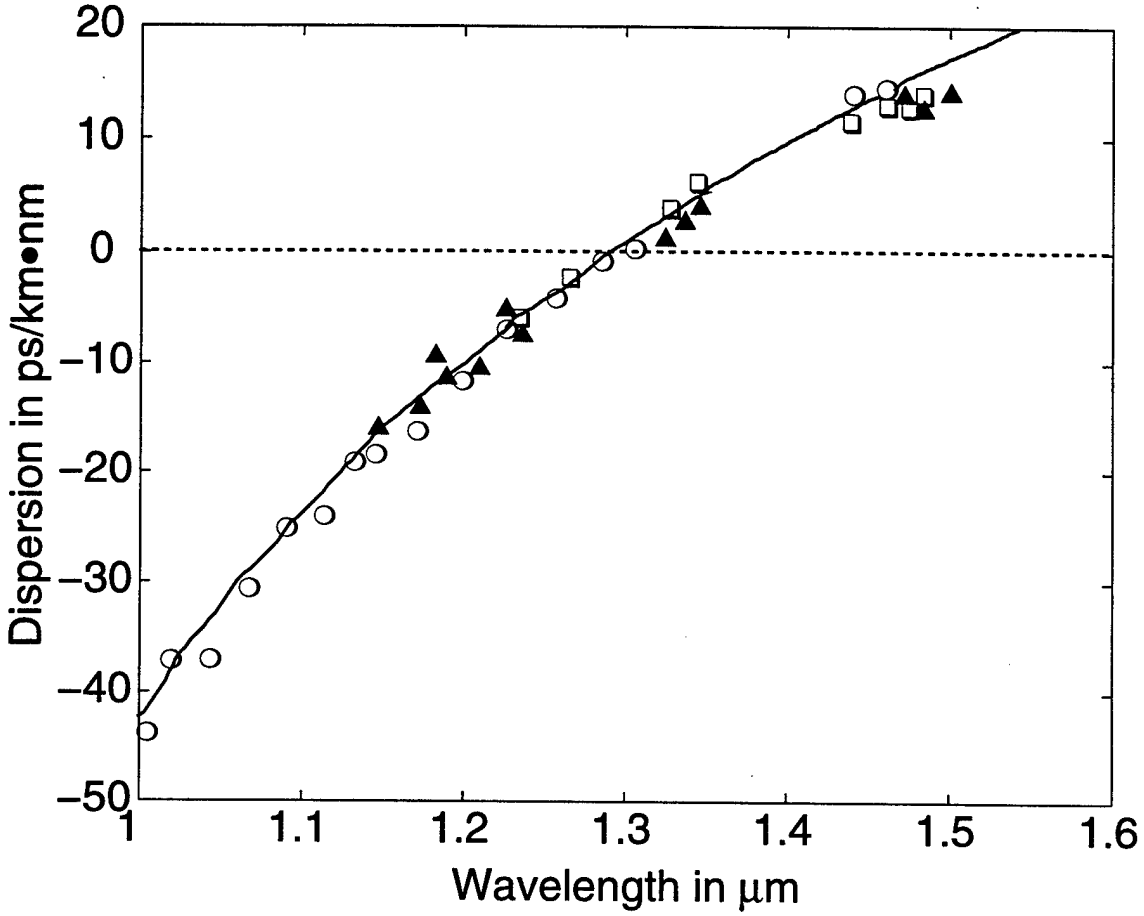

Figure 1.3: Measured material dispersion for typical single-mode silica fibers. Note that at $\lambda \sim 1.3\mu$m, there is a zero cross point.

1.3 Distributed Feedback (DFB) or Distributed Bragg Reflector (DBR) Lasers

As mentioned above, the information transmission rate is mainly limited by chromatic dispersion in the fibers, which results from the broadening of optical pulses during propagation inside a single-mode fiber. Therefore, a single frequency light source is essential and necessary for high data rate transmitters. Distributed Feedback (DFB) lasers, first demonstrated by Kogelnik and Shank in 1971 [9], provide a good solution in producing single frequency light by introducing periodic perturbation of refractive index (known as index coupled mechanism), gain (gain coupled mechanism), or combination of both refractive index and gain (complex coupled mechanism). This periodic structure functions like a filter and selects only the mode which satisfys the Bragg condition. InP-based multiwavelength DFB laser arrays [10], which provide the ability to generate well-defined single-mode optical signals for WDM systems, have therefore emerged as important components in transmitter design.

Distributed Bragg reflector (DBR) lasers, in contrast to DFB lasers, have the gratings etched outside the active region. The grating region, together with the facet, forms an effective mirror reflectivity which varies with wavelength and, thus, selects the lasing mode at its maximum gain region.

An important objective of this work was to investigate the design, fabrication, and characterization of 0.98μm GaAs-based and 1.55μm InP-based tunneling injection multiple quantum well (MQW) DBR and DFB lasers.

1.4 External Intensity Modulators

Direct modulation of semiconductor lasers gives rise to a serious chirp problem which limits its application in high-bit-rate transmission in single-mode fiber systems. In addition, the damping peak incurred in direct modulation is not suitable for real applications, which requires relatively flat response. At the present time, the direct modulation scheme has only been adapted commercially in SONET/SDH OC-48 systems at 2.5Gb/s or other systems below this transmission rate, while OC-192 systems at 10Gb/s or other systems beyond 10Gb/s [1] tend to use external modulation techniques. Figure 1.4 shows several different types of external intensity modulators which are either in a development stage or are commonly used [11].

The principle of a total internal reflection type modulator [12] is that a reflected light or transmitted light is modulated by varying the amplitude reflectivity at the boundary due to the refractive index change in different regions. Mach-Zehnder interferometer modulators [13] have been widely used in various appilcations because of their superior chirp performance (they have zero or negative chirp parameters). Here chirp parameter α is defined as:

$$\alpha = \frac{\Delta n'}{\Delta n''} \tag{1.3}$$

and $\Delta n'$ is the relative change of real part of the refractive index and $\Delta n''$ is the relative change of imaginary part of the refractive index. The incoming light is separated equally in a "Y waveguide" and then recombined together at the output port. The light is modulated according to the net phase-shift difference between the two arms, which are under different bias. An optical wave can be switched in a directional-coupler [14] from the straight-through state to the crossover state by applying electric fields to the waveguides. Their detailed switching characteristics

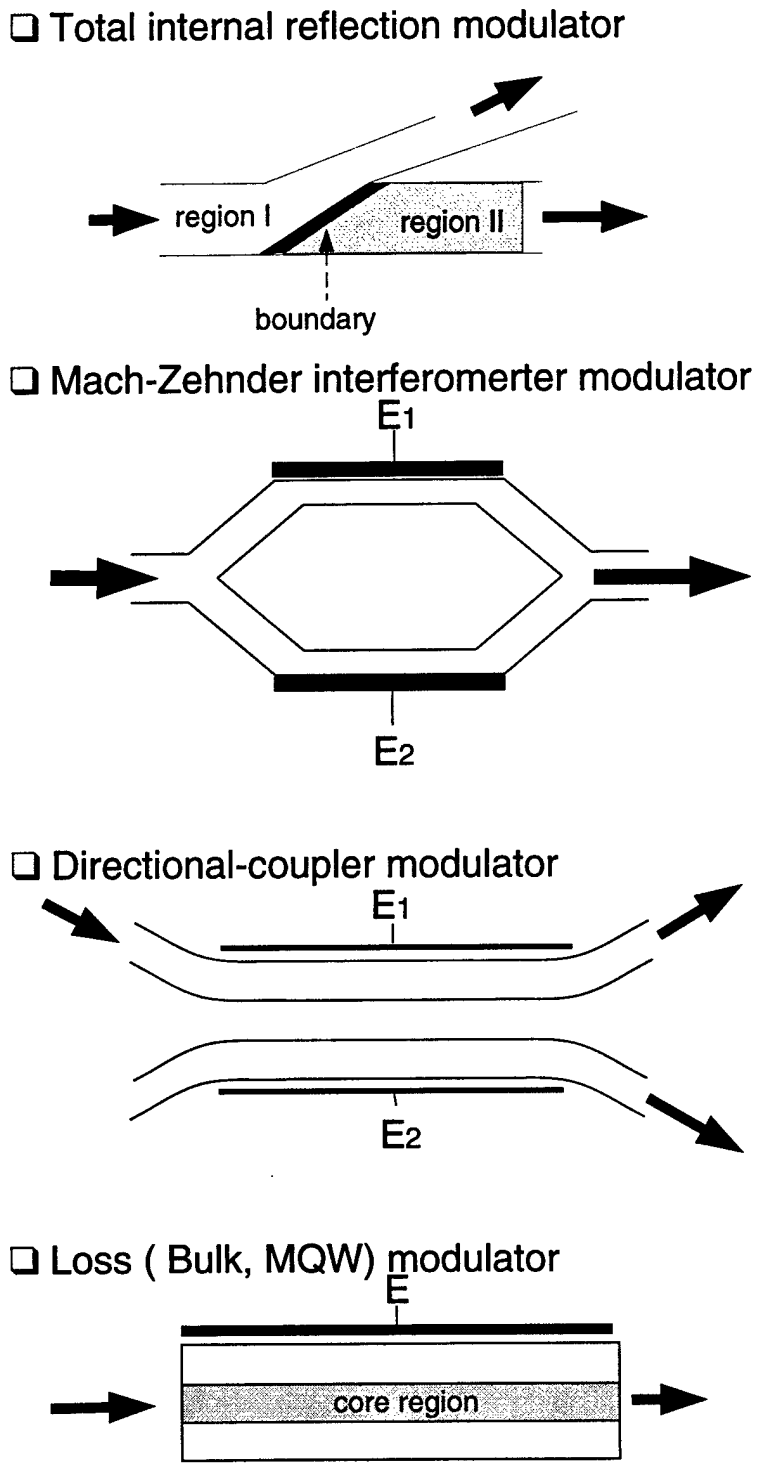

Figure 1.4: Schematic strucutures of external intensity modulators.

can be analyzed by using coupled mode theory. A loss modulator operates with a variable loss (or gain) to laser light passing through the core region. Their operation is based on the Franz-Keldysh effect (FKE) [15] for the bulk materials, or quantum Confined Stark effect (QCSE) for quantum wells [16], and are also called electroabsorption modulators. This type of modulator has many advantages, such as small size, costly effectiveness, high modulation bandwidth ($\geq$ 50Gb/s), low chirp parameter ($0.3 \sim 0.6$) if the appropriate bias condition is chosen and properly designed structure is used, and has thus become a promising candidate for WDM networks applications in the near future [2].

In this work, only GaAs and InP-based QCSE multiple quantum well (MQW) modulators were considered and studied.

1.5 Integrated Laser and Modulator

A typical transmitter used in the external modulation mode usually suffers a severe insertion loss ($\geq$ 10dB) [17] if discrete components are used. Even with a carefully designed waveguide structure and fiber tip, there is still a 6–8dB loss [18]. In addition, from the packaging point of view, it takes enormous labor cost and delicate equipment to achieve an acceptable optical alignment. To avoid the above shortcomings, monolithic integration of laser and semiconductor external modulator provides an effective and promising solution. Several different integration schemes have been proposed and successfully demonstrated, as illustrated in Fig.1.5 [19].

The integrated coupled-cavity laser/modulator [20] is the simplest approach and can be realized by one-step epitaxy. The different cavities with the same active region are separated by dry etching techniques to form the coupling facets. Lasing and modulation can be achieved by choosing appropriate bias conditions in the different

- Cleaved-Coupled-Cavity (C^3) Lasers.

(same active region)

- Selective Area Growth (SAG) to integrate DFB/DBR laser with EA modulator.

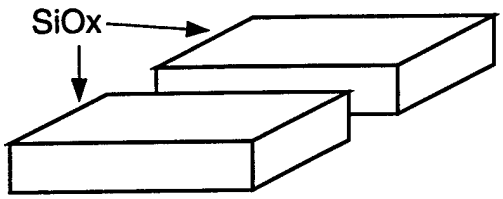

(one-step growth on SiO_x patterned substrate)

- Butt-coupling of Integrated DFB/DBR laser with EA modulator.

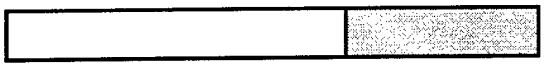

(two steps growth, grow laser first then grow modulator)

- Quantum Wells Interdiffusion by Dielectric Encapsulant..

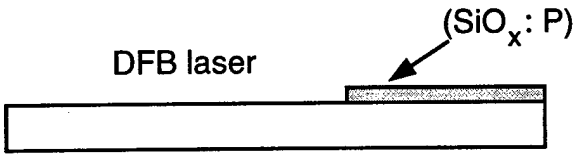

(same active region, annealed at ~800°C to cause blue-shift in the covered region)

- Changing Laser Wavelength by DFB or DBR Grating Periods.

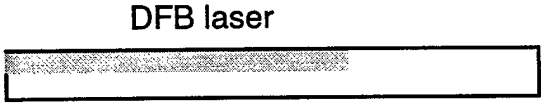

(one step epitaxy, DFB grating $\Lambda > \lambda(E_g)$)

Figure 1.5: Different approaches for realizing laser/modulator integration.

cavities through amplification and absorption, respectively. The gap distance and the bias conditions can also determine mode selectivity as well as wavelength tunability. In reality, the laser linewidth generated in this scheme is too broad compared with that generated from DFB lasers and often a forward bias has to be applied to the modulator to obtain an adequate extinction ratio. These drawbacks ,which not only cause a large power consumption problem, but degrade the chirp performance, make it impossible to meet the requirements of modern communication systems. As the materials growth technology progresses and the single frequency operation required in long-haul transmission systems becomes more stringent, the DFB laser has become an essential component in the integrated laser-modulator transmitter. Owing to the intrinsic feedback characteristics of the DFB gratings, no additional feedback facet is needed for laser operation in this integration scheme.

Selective Area Growth (SAG) technique [21] takes advantages of the variation of the bandgap of MQW material in the same plane with a single growth step by metal-organic vapor phase epitaxy (MOVPE) over a plasma enhanced chemical vapor deposited (PECVD) SiO_x masked substrate. The bandgap variation results from a local growth rate enhancement where the source material does not nucleate on the masked area and is deposited in the unmasked trenches. High performance integrated devices have been demonstrated and obviously, it has the advantage of processing simplicity. One potential drawback of this scheme is the difficulty of independent optimization of each component.

The butt-coupling scheme [22] is a promising approach which generally requires multiple epitaxial growth steps for the individual active regions of the two devices. Usually the laser structure is first grown on the entire wafer and is selectively etched away in selected regions. The modulator structure is next grown. This approach

provides the flexiblity to optimize each device separately. However, critical etching and regrowth steps are required to achieve efficient optical coupling.

Another simple approach to achieve the integration is to grow the same active MQW active region with wider bandgap (suitable for the modulator) and tune the laser emission wavelength by the DFB grating period [23]. Such design, however, has to compromise the laser gain spectra and, thus, suffers from a higher laser threshold current and insufficient modulator extinction ratio.

Recently, a novel yet relatively simple approach that has been proposed employs the quantum well intermixing method to realize the integration. An identical active region is used [24]. By selectively patterning the laser heterostructure with PECVD SiO_x:P and rapid thermal annealing at a high temperature ($\sim$800°C for 5–10sec), selective-area interdiffusion of the P-dopants between the well and barrier materials is induced. This results in a blue shift of the absorption edge in the dielectric encapsulated area. Further investigation of the device reproducibility and reliablity, made by this technique, is needed.

This work is primarily focused on the coupled-cavity and butt-coupling schemes.

1.6 Lightwave-Communication Integrated Circuits

Very-high-speed optical-fiber transmission experiments have currently been conducted with speeds $\geq$ 100Gb/s [25]. Such high transmission speeds result mainly from all-optical switches (MUX/DEMUX) and these technologies are still in their infancy. Electronic devices, on the other hand, have some advantages over optical devices: high functionality, small size, low cost, and high reliability. Figure 1.6 shows the performance of state-of-the-art lightwave communication integrated circuits (IC) [26] used in transmitters. From the current results, Si technology seems to demon-

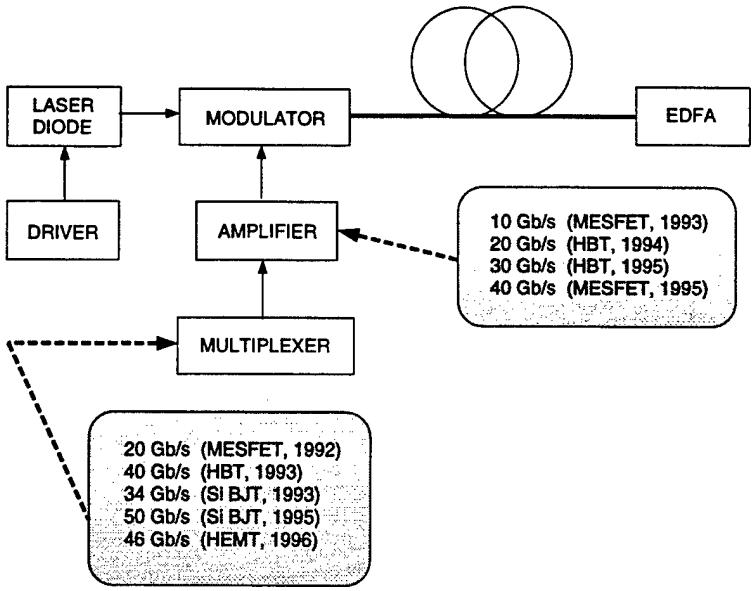

Figure 1.6: State-of-the-art lightwave communication transmitter IC performance.

strate comparable or superior performance to their III-V counterparts in multiplexers. For the driver circuits, III-V devices obviously have better performance. Among the III-V technologies, heterojunction bipolar transistors (HBT) have some advantages over metal semiconductor field effect transistors (MESFET) or high electron mobility transistors (HEMT) in power handling as well as current driving capability and linearity. For operation under 20 GHz, HBTs also shows lower 1/f noise. These are the major concerns in designing the driving circuits. InP-based electronic devices can be further integrated with other optoelectronic devices at 1.3–1.5μm range to make the systems very compact. In the present study driver circuits with HBTs were investigated.

1.7 Organization of This Thesis

The work presented in this dissertation is organized into three major components: optical sources, modulation devices, and integrated transmitters.

Chapter II describes the design and fabrication of a novel 0.98μm short-cavity

semiconductor/air DBR laser. The extremely impressive results obtained from the devices are reported and discussed.

Chapter III focuses on the design and fabrication of a 1.55μm tunneling injection DFB laser. The tunneling injection mechanism, conceived at the University of Michigan, has been incorporated in a DFB laser for the first time. The device characteristics are described and discussed.

Chapter IV describes the design and characterization of InP-based InAlAs/InGaAs QCSE MQW modulator. Specific considerations for designing the modulator are addressed. A dramatic reduction in photoresponsivity of the device, which is a serious problem, is demonstrated with selective Er-doping of the quantum wells for the first time.

Chapter V demonstrates a coupled-cavity integrated laser/modulator. Detailed device fabrication procedures and analysis of device performance are described.

Chapter VI presents my design of integrated transmitters. Two simple HBT circuits designed for driving the laser and modulator will be discussed. The design and analysis of monolithical integration of laser, modulator, and HBT driver circuits are addressed as well.

Finally, in Chapter VII, I summarize the current work and provide suggestions on future directions for the continuation of this work.

CHAPTER II

EDGE-EMITTING LASERS WITH SHORT-PERIOD SEMICONDUCTOR/AIR DISTRIBUTED BRAGG REFLECTOR MIRRORS

2.1 Background and Motivation

Large-bandwidth tunable semiconductor diode lasers, with the possiblity of near-zero bias small-signal modulation [27], are attractive for long-distance wavelength division multiplexed (WDM) transmission, short-distance optical interconnection, and other optoelectronic applications. It is also becoming increasingly important to make these lasers integrable with other optical and opto-electronic components. Such coupling necessitates devices with non-cleaved mirrors. Large bandwidths are obtained under very high level injection conditions, or a large photon density, and the common wisdom is to make the cavity length of the edge-emitting device as small as possible. A small cavity length will also ensure a low threshold current I_{th} [28]. From the point of view of manufacturability, cavity lengths smaller than 200μm, unless realized by dry etching techniques, such as reactive ion etching (RIE), reactive ion beam etching (RIBE), chemically-assisted ion beam etching (CAIBE) [29],[30], etc., are impractical. These problems can be addressed and solved in a simple and

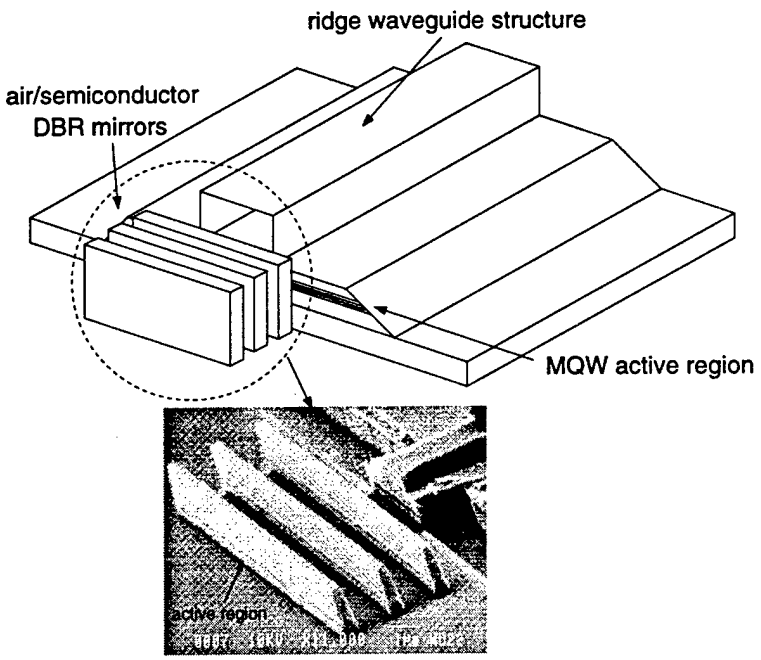

Figure 2.1: Schematics and photomicrograph of edge-emitting laser with air / semiconductor DBR mirror delineated by RIE.

elegant manner.

In this chapter a new technique of realizing a short-cavity edge-emitting semiconductor/air distributed Bragg reflector (DBR) laser is described. State-of-the-art device performance is demonstrated. The laser structure is schematically shown in Fig.2.1.

The DBR mirrors are fabricated by RIE from the laser heterostructure. Instead of using high-reflectivity (HR) coatings on the laser facet, this laser incorporates deeply etched DBR gratings to increase the mirror reflectivity and the device fabrication does not involve epitaxial regrowth or dielectric deposition steps. In addition, the DBR mirrors make the realization of short cavity lengths possible. Preliminary results ($J_{th} \sim 5$ kA/cm^2) of a broad area laser based on the same concept have been recently reported by Baba *et al* [31]. A low threshold current and reasonably high small signal modulation bandwidth 100μm long device is demonstrated in this work.

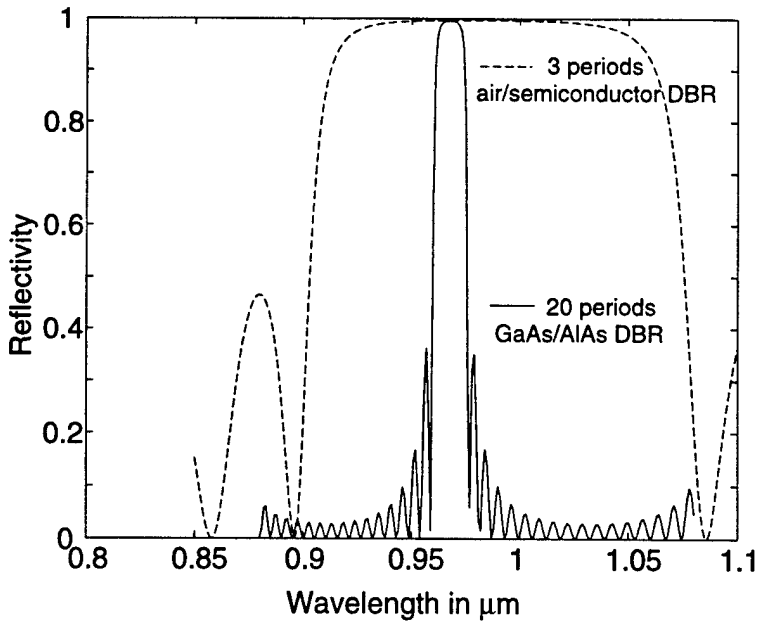

Figure 2.2: Calculated DBR reflectivity spectrum.

Much smaller cavities can be delineated, leading to the possiblity of realizing true gain-compression limited bandwidth ($\sim$ 80GHz) in semiconductor lasers [32].

2.2 Design of Distributed Bragg Reflectors

2.2.1 Mirror Reflectivity

Distributed Bragg Reflectors, which consists of a number of periodic quarter-wavelength stacks with different refractive indices, are widely used in producing single-mode semiconductor lasers, vertical cavity surface emitting lasers (VCSELs), and optical filters, etc. By solving the Maxwell's equations and applying the appropriate boundary conditions, the DBR reflectivity can be calculated [33] for a given number of period at a particular wavelength. Fig.2.2 depicts the calculated reflectivity spectrum for a 20 periods GaAs/AlAs (n=3.54/2.95) DBR and a 3 periods air/semiconductor (n=1/3.31) DBR. Here we assume plane waves propagating inside the periodic medium. Due to the large difference of refractive index between

air (n_{air}=1) and semiconductor ($n_{semiconductor} \simeq 3.5$), the DBR reflectivity spectrum shows a very wide high reflectivity band ($\sim 1000\mathring{A}$), which allows us to have higher tolerance to lithographical error, imperfect etching, and off-design wavelength lasing. On the other hand, the mode-selectivity would be very poor in such a wide passband. In this structure the lengths corresponding to $\lambda/4$ in the semiconductor and in the air are about 740 Å and 2460 Å, respectively.

2.2.2 Experimental Considerations

In reality, the mechanical strength or stability of the $\sim$ $700\mathring{A}$ wide and $\sim$ 2μm high semiconductor material, needed for a first-order grating, would be very fragile. In addition, the loading effect during etching these deep trenches will be very severe. In other words, the etched byproducts during dry etching cannot be removed efficiently. Hence, a $5\lambda/4$ grating has been used in this laser. However, there are some tradeoffs with this design. From modeling studies [34] the reflectivity tends to saturate beyond 2 periods of the DBR and the maximum reflectivity decreases from 0.93 for the 2-period $\lambda/4$ DBR to 0.66 for the 2-period $5\lambda/4$ DBR. This reduction in reflectivity is mainly due to the divergence of the propagating optical wave. Besides, the absorption will increase as the semiconductor thickness increases and this absorption leads to further reduction in effective reflectivity.

2.3 Devices Structure and Fabrication

2.3.1 Structure

The laser heterostructure, shown in Fig.2.3, was grown by atmospheric pressure metal-organic vapor phase epitaxy (AP-MOVPE) on (001)-GaAs substrate. It is a tunneling injection multiquantum well structure [35], which is known to minimize hot-carrier effects in high-speed lasers. This is because by designing a thin tunneling

0.2μm	GaAs	p $\doteq$ 3 $\times 10^{19}$
1.0μm	Al $_{0.6}$Ga$_{0.4}$As	p : 5 $\times 10^{17}$
250Å	Al $_{0.1}$Ga$_{0.9}$As	i
48Å	In $_{0.2}$Ga$_{0.8}$As	i
70Å	GaAs	i
50Å	In $_{0.2}$Ga$_{0.8}$As	i
70Å	GaAs	i
54Å	In $_{0.2}$Ga$_{0.8}$As	i
70Å	GaAs	i
64Å	In $_{0.2}$Ga$_{0.8}$As	i
30Å	AlAs	i
500Å	GaAs	i
1.0μm	Al $_{0.6}$Ga$_{0.4}$As	n : 5 $\times 10^{17}$
0.5μm	GaAs	n $\doteq$ 3 $\times 10^{19}$
	S. I. GaAs Substrate	

Figure 2.3: Device heterostructure grown by atmospheric pressure MOVPE.

barrier for electrons to be injected into the laser quantum well active region, the carrier capture time becomes shorter and the escape time becomes longer, as opposed to the conventional separate confinement heterojunction (SCH) laser structures.

2.3.2 Formation of DBR gratings

The DBR gratings are defined by direct electron beam writing with $\sim$ $250nm$ thick polymethymethacrylate (PMMA) resist coated on the sample. After e-beam lithography, a 1000Å Ni was evaporated on the sample as an RIE etch mask.

The gases chosen to etch this structure (GaAs/InGaAs/AlGaAs) are BCl_3 and Ar mixtures in the RIE chamber. In order to achieve nearly vertical walls in such a narrow trenches ($\sim$ 1μm), a high rf power (180-200W) and proper gases flow ratio (BCl_3 : Ar = 21 : 25) are required. The chamber pressure is maintained at 10-20mT. The DC bias generated in this condition is -450 $\sim$ 470 V.

One can imagine that under this high bias voltage, a durable etching mask is necessary to provide good protection during etching and, in addition, it must be able to be removed easily for the subsequent laser process. Experimental results indicates that Si_xN_y is an effective etching mask and can be removed by buffered HF (BHF) without attacking the epilayers of the structure.

2.3.3 Devices Fabrication

Devices are fabricated as follows: first, the p-ohmic contact metal (Pd/ Zn/ Pd/ Au/ Ni) is deposited on the wafer. A thick plasma enhanced chemical vapor deposited (PECVD) Si_xN_y ($\sim$ 8000Å) layer is then deposited and patterned on the laser regions. The $5\lambda/4$ air/semiconductor (1.23μm/0.37μm) is defined by direct e-beam writing and is followed by evaporation of $\sim$ 1000Å Ni on the sample as an etch mask. Fig.2.4 illustrates the e-beam lithography alignment marks and Fig.2.5

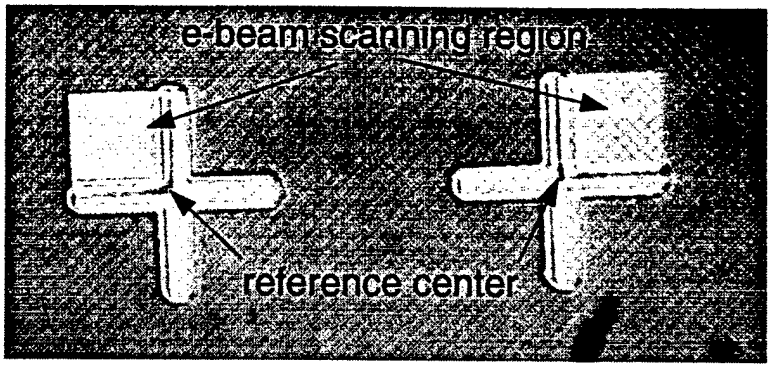

Figure 2.4: Alignment mark for e-beam lithography.

indicates the device layout design. The gratings are formed by reactive ion etching (RIE) using the recipe mentioned above and the etch depth is about 2μm. After the formation of the gratings, the single mode ridge waveguide is etched by the combination of RIE (BCl_3 : Ar=11:21, 15mT, 50W) and wet etching (H_3PO_4 : H_2O_2). The n-contact metal (Ni /Ge /Au /Ti /Au) and interconnection metal are finally deposited. High-speed lasers for small-signal modulation experiments are formed in a coplanar ground-signal-ground contact geometry. The lasers are then cleaved into lengths of 100–400μm for testing. A photomicrograph of the DBR mirror region of a 100μm long device is also shown in Fig.2.1 and an overview of a fabricated device is shown in Fig.2.6. The complete process flow in Fig.2.7 .

2.4 DC Characteristics

The measured light-current (L-I) characteristics of the laser for different cavity (active region) lengths are shown in Fig.2.8. The emission wavelength is 0.98μm. The lasers have a cleaved mirror at one end and the DBR at the other. The output is taken from the cleaved end. These lasers had 2-4 periods of DBR and an effective reflectivity of $\sim$0.6 is obtained from the measured slope of threshold current density versus inverse cavity length, shown in Fig.2.9. The slightly lower effective reflectivity,

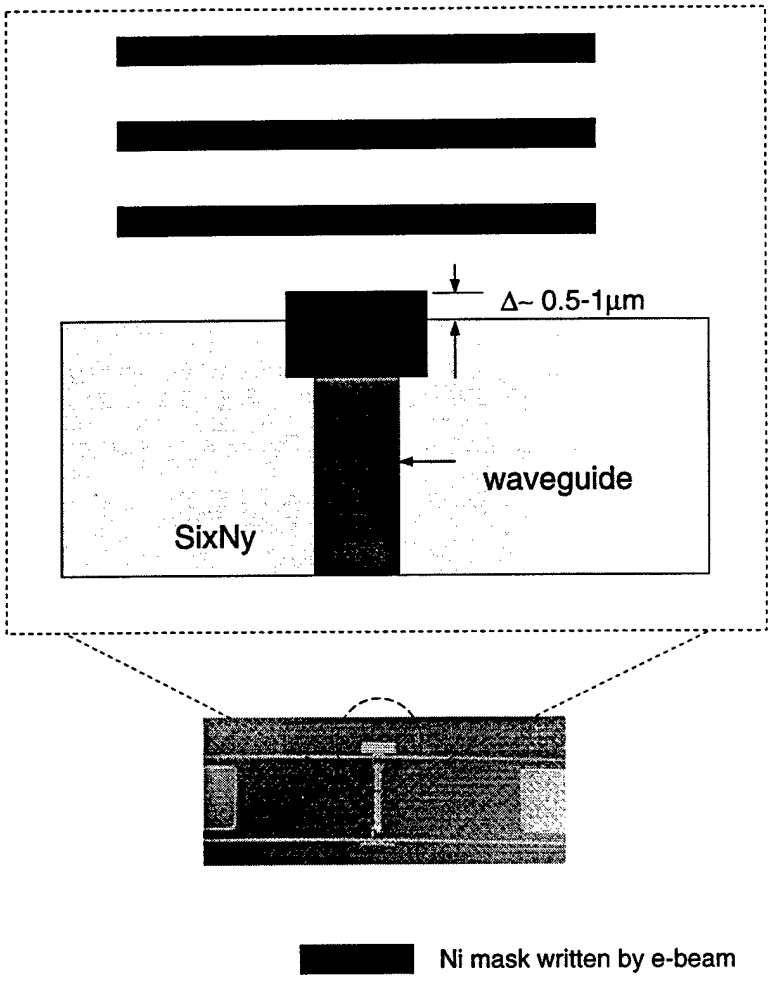

Figure 2.5: Device layout design and micrograph picture.

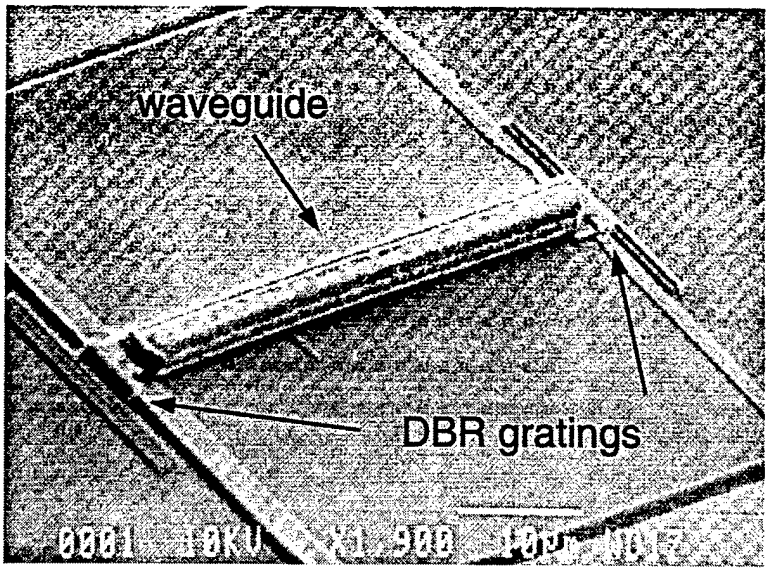

Figure 2.6: Overview of a fabricated device.

compared to the calculated value, is believed to be due to imperfect processing and surface scattering. Also there is no significant variation in the threshold current, for a given cavity length, with different DBR periods. The data of Fig.2.8 also depict the expected increase of slope efficiency with decrease of length. The threshold current I_{th} for the 100μm long device is 4.5mA and J_{th}=1.324 kA/cm^2. The slope efficiency is 0.28 W/A. The cavity loss coefficient α_i is obtained to be 13.5 cm^{-1} and the quantum efficiency η_i is 0.52. The transparency current is 370 A/cm^2. The surface damage caused by RIE of the DBR enhances the value of α_i in these structures.

2.5 Laser Far-Field Characteristics

The DBR mirror is expected to have a small diffractive effect on the light output, thereby reducing the width of the output mode. However, since the DBR was not covered with any anti-reflective (AR) coating, multiple reflections and scattering between the etched DBR mirrors may also take place. To investigate these issues the near and far-field patterns from both the cleaved end and the DBR end have been

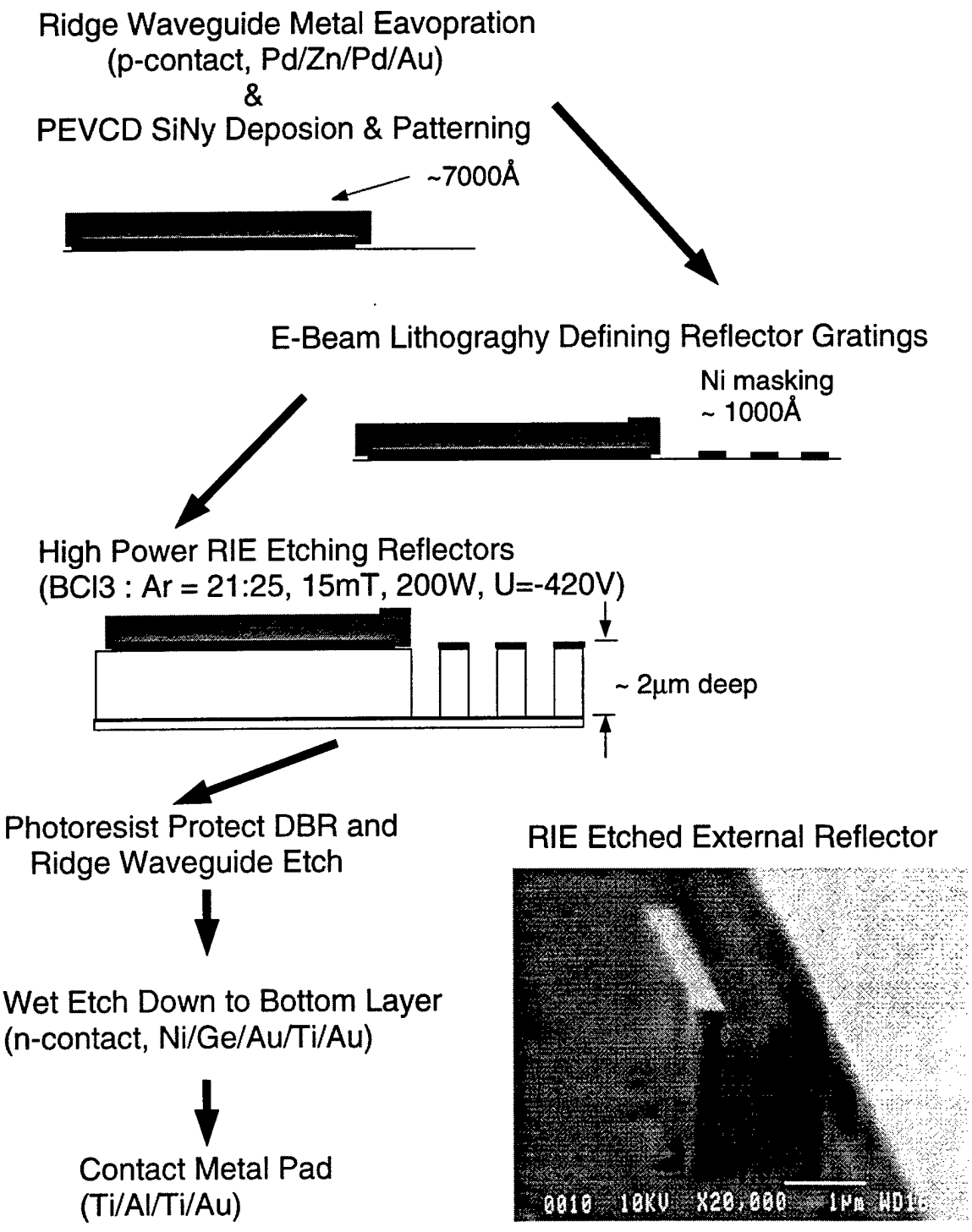

Figure 2.7: DBR laser process steps.

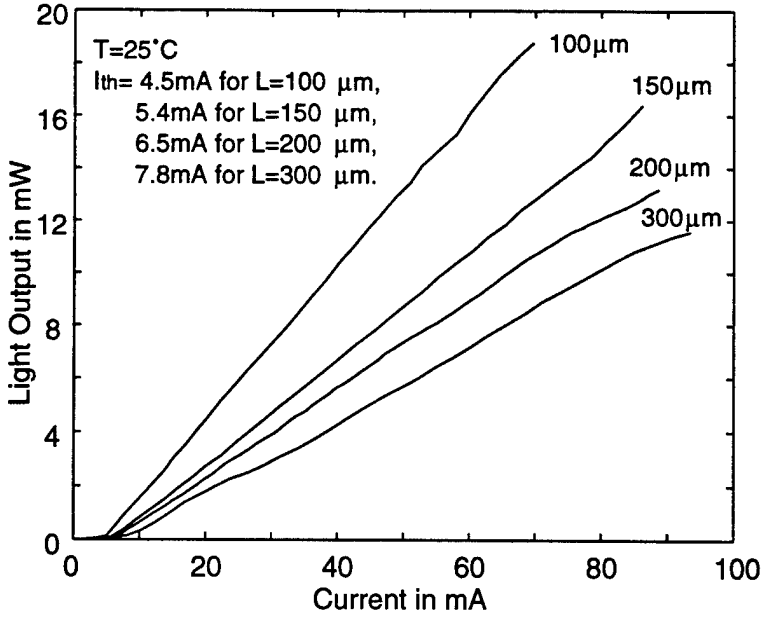

Figure 2.8: Measured L-I characteristics for devices with different cavity lengths and having a cleaved facet at one end and a DBR mirror at the other. The light output was taken from the cleaved side.

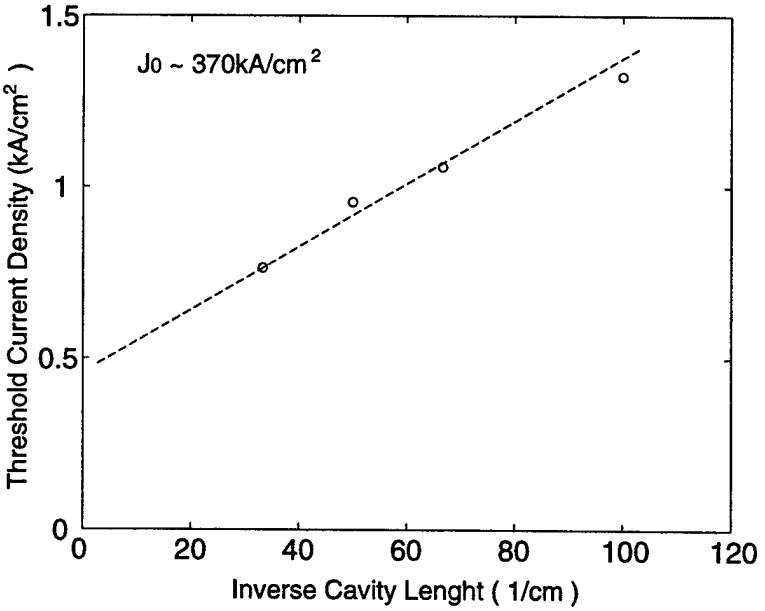

Figure 2.9: Measured threshold current density versus inverse cavity length.

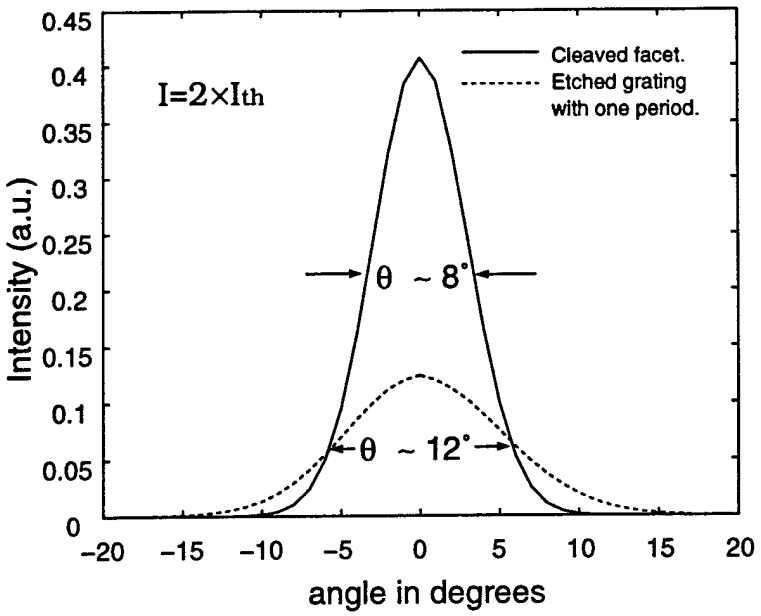

Figure 2.10: Measured far-field pattern in parallel direction.

measured. The near field pattern at both ends from the IR camera shows single-mode characteristics (TE_{00}). The measured lateral far-field patterns, at a distance of 5 *cm* from the mirrors, are shown in Fig.2.10. The parallel and perpendicular angular spread of the output from the cleaved facet is as expected, with $\Theta_{||} \sim 8°$ and $\Theta_{\perp} \sim 25°$, as is shown in Fig.2.11. The output from the DBR in the perpendicular direction could not be measured since the mirrors terminated on the wafer at a distance of $\sim 50\mu$m from the end. The parallel output shows two distinct features. The intensity is smaller than that from the cleaved end. Also, the angular spread is actually a little larger ($\Theta_{||} \sim 12°$) than that for the cleaved facet. The former is probably due to multiple reflections and defocusing and the latter is also probably due to reflections and scattering. However, the slight broadening in the transverse direction can actually make the output more symmetric (circular) and therefore more amenable to focusing and coupling with conventional optical fibers.

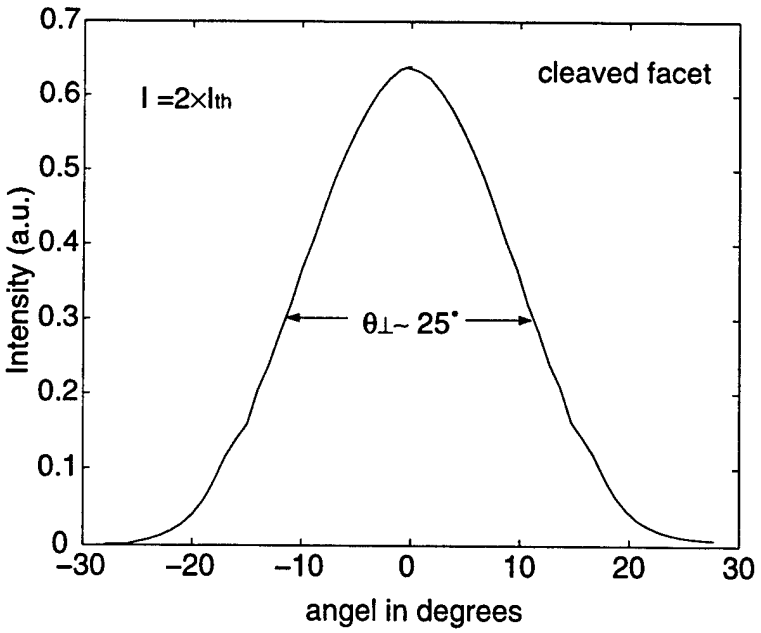

Figure 2.11: Measured far-field pattern in perpendicular direction.

2.6 Small-Signal Modulation

The small signal modulation characteristics of the lasers were measured under pulsed bias condition with an HP8350B sweep oscillator, bias Tee, wide bandwidth amplifiers, a 40 GHz New Focus detector and an HP8593A spectrum analyzer. The power of the microwave signal modulating the laser was set at -5 dBm. The curve in Fig.2.12 shows the fitted data of the modulation frequency response for differnt bias currents, using the optical modulation response equation [37]. The modulation response used to fit the experimental data is expressed as

$$|M(f)|^2 = |M_{p,t}|^2 \frac{f_r^4}{(f_r^2 - f^2)^2 + (\gamma/2\pi)^2 f^2} \tag{2.1}$$

where f_r is the relaxation frequency, γ is the damping rate, $M_{p,t}$ is a transfer function accounting for both device layout parasitics and carrier-transport-related effects and the second term explains the intrinsic frequency response. The relaxation frequency derived from small-signal analysis of the coupled rate equations for charge carriers

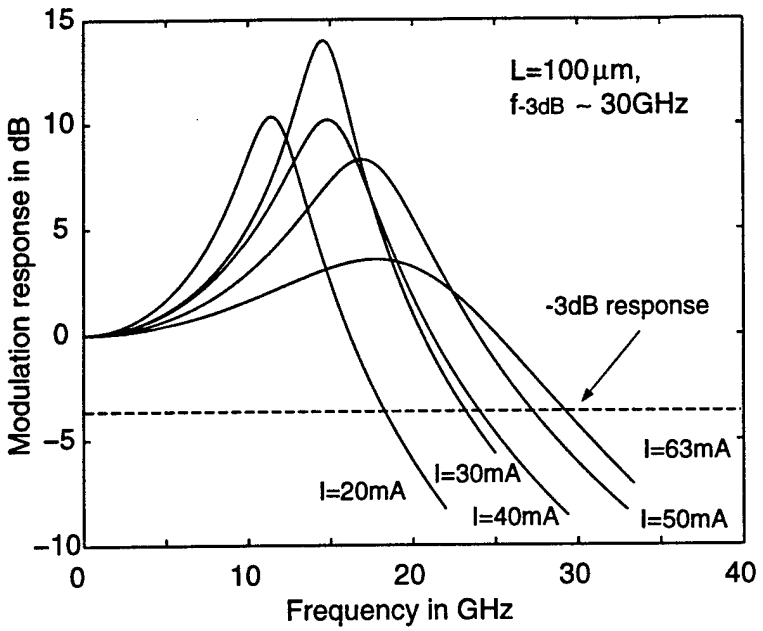

Figure 2.12: Small-signal current modulation response of a 100μm long laser at different bias currents under pulsed conditions.

and photons can be defined as:

$$f_r = \frac{1}{2\pi}\sqrt{\frac{\Gamma \partial g/\partial n v_g \eta_i (I - I_{th})}{qLwd_{act}}} \tag{2.2}$$

where Γ is the confinement factor, ∂g/∂n is the differential gain, v_g is the group velocity of the lasing mode in the laser cavity, η_i is the internal differential quantum efficiency, I_{th} is the laser threshold current, and Lwd_{act} is laser active region volume. The damping rate which is a function of the effective carrier lifetime in the laser active region τ_c and the relaxation frequency can be written as:

$$\gamma = \frac{1}{\tau_c} + K f_r^2 \tag{2.3}$$

The damping factor K is a function of differential gain ∂g/∂n and the photon lifetime in the active region. A measured 3 dB bandwidth of $\sim$ 30GHz is reached at the highest driving current of 63 mA for a 100μm long device under pulsed conditions (1μs pulses with 1% duty cycle). Higher bandwidths can easily be achieved in this

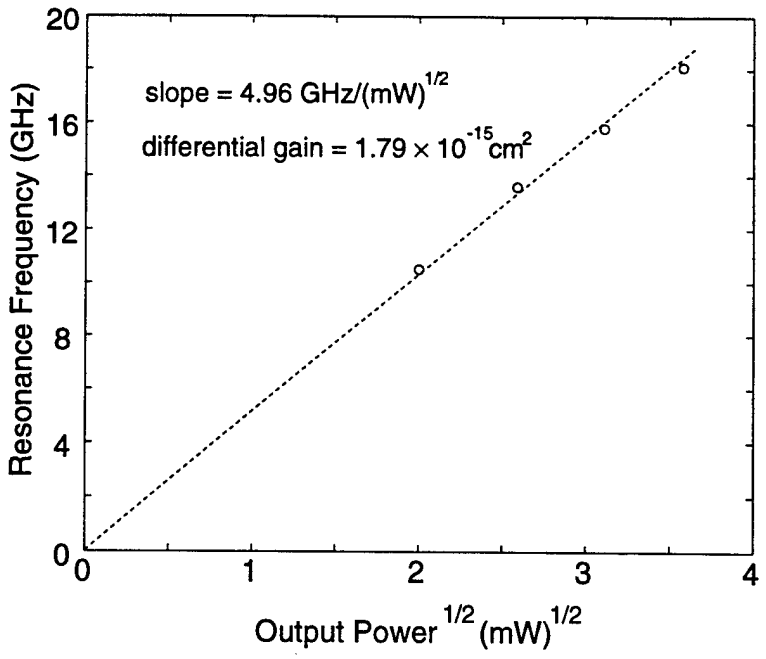

Figure 2.13: Relation of resonance frequency versus square root of output power.

device with proper mounting and heat-sinking.

From analysis of the data of Fig.2.12 and the relation of relaxation frequency versus output power, plotted in Fig.2.13, the differential gain $\partial g/\partial n = 1.79 \times 10^{-15}$ cm^2. From the slope of the plot in Fig.2.14, the K factor [36] is 0.19 ns, and $f_{-3dB}(max) = 2\frac{3}{2}\pi/K = 47$ GHz. The modulation response of this device will be very similar to that of a Fabry-Perot device [35]. There is no intrinsic reason for it to be better. However, the design of the DBR laser allows for much smaller cavity lengths, from which higher modulation bandwidths can be derived.

2.7 Summary

A novel short cavity edge-emitting 0.98μm GaAs-based laser with semiconductor/air DBR mirrors made by reactive ion etching (RIE) has been demonstrated. The dc and small-signal modulation properties of 100μm long lasers have been measured and are characterized by I_{th}=4.5 mA and f_{-3dB}=30 GHz under pulsed conditions ,

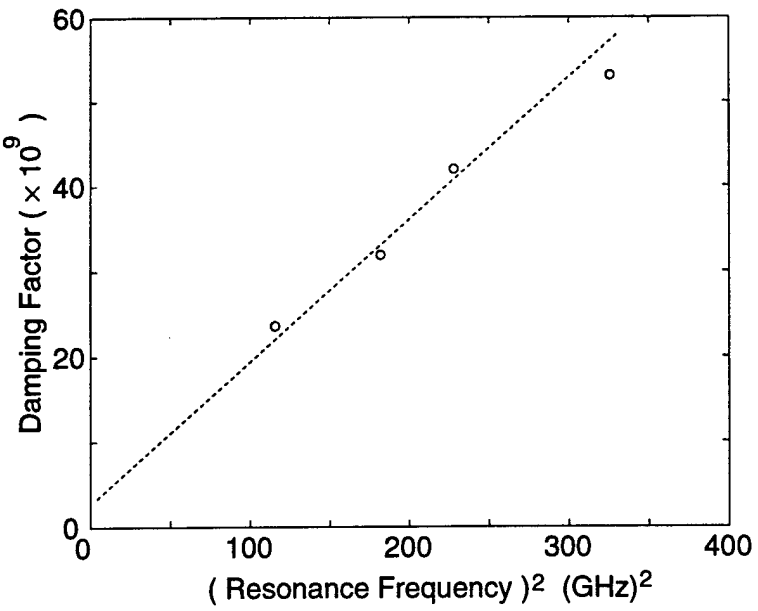

Figure 2.14: Damping factor versus resonance frequency square.

respectively. The far-field pattern of light emanating from the DBR is also measured. From current results, it is clear that with proper DBR reflectivities at both ends, it is possible to shrink the length to $\leq 10\mu$m. Thus, edge-emitting microcavity lasers can become feasible. In addition, the individual elements of the deeply etched DBR, functioning as a spatial filter can be reshaped, by lithography, to tailor the near-field pattern of the optical mode and, thus, to incorporate better focusing of the output light, Fig.2.15 or addressing the light toward certain directions, [38] Fig.2.16, which have great potentials in light multiplexing and demultiplexing applications.

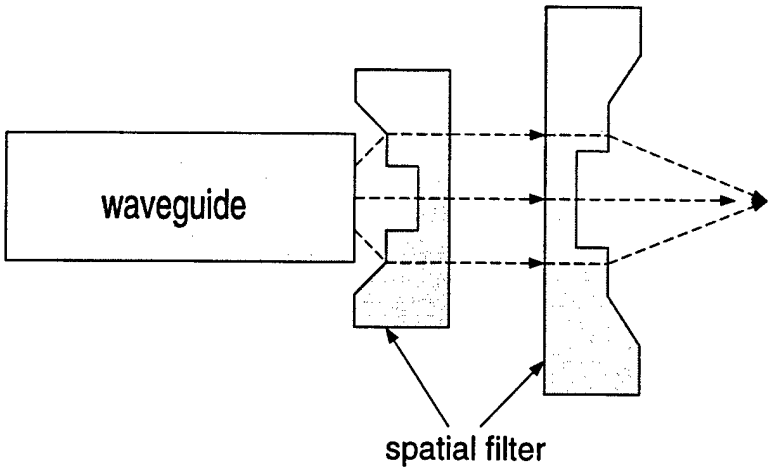

Figure 2.15: Schematic of proposed spatial filter.

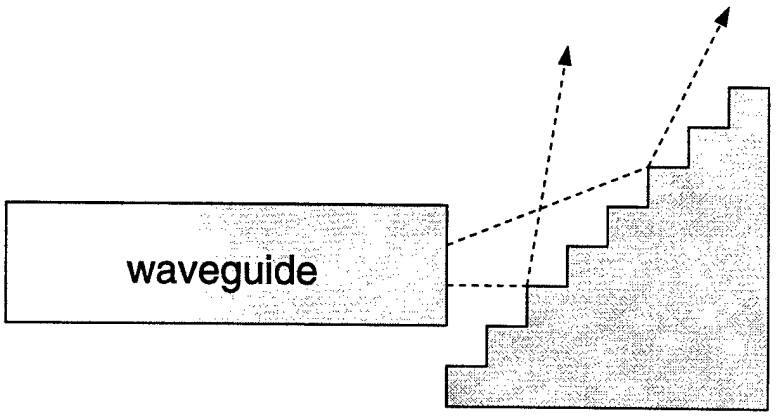

Figure 2.16: Schematic of proposed beam director.

CHAPTER III

Tunneling Injection Distributed Feedback Laser

3.1 Introduction

Semiconductor Distributed Feedback (DFB) lasers have attracted considerable attention since the DFB mechanism was first demonstrated by Kogelink and Shank in 1971. As the materials growth and lithography technologies progress, semiconductor DFB lasers have emerged as the most viable light sources in modern communication systems due to their unique characteristics, e.g., single frequency operation, narrow linewidth, and insensitivity to temperature variation [39]. Most importantly, the lasing wavelength can be precisely determined by the period of the corrugation and this makes wavelength division multipexing (WDM) very attractive with these devices.

In this chapter, only the index-guided DFB structure is considered. First, an overview of the coupled-mode theory is briefly described, including the fundamental principle of the DFB mechanism, threshold gain condition, and the coupling coefficient. The design of 1.55μm tunneling injection (TI) multiple quantum well (MQW) DFB lasers is next discussed. The device fabrication is described in detail. Finally, the device performance characteristics are described and discussed. This is the first time that the tunneling injection mechanism has been incorporated in a DFB laser.

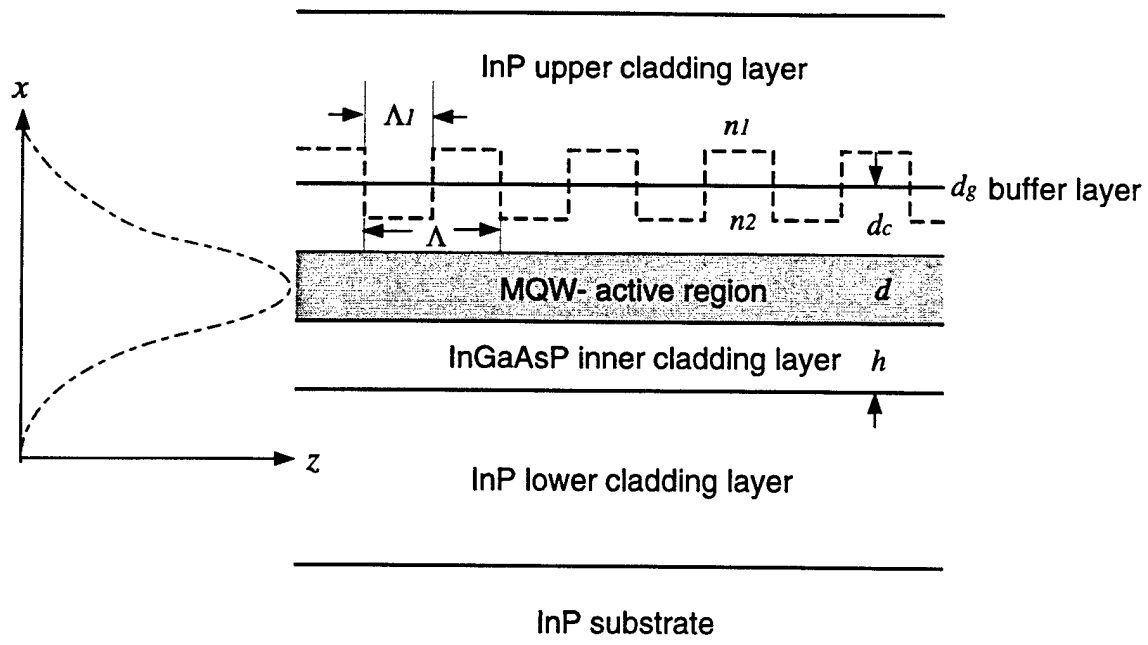

Figure 3.1: Schematic of a typical index-guided DFB laser.

3.2 Theory of DFB Lasers

Unlike conventional Fabry-Perot (FP) lasers which require end facets to provide lasing feedback, the DFB lasers utilize periodic corrugation to achieve optical feedback. The fundamental theory is based on the coupled-mode theory [5],[40], which solves the forward and backward propagating waves in the laser cavity. The lasing mode selected results from the Bragg condition,

$$\Lambda = \frac{m\lambda}{2n_{eff}} \tag{3.1}$$

where Λ is the grating period, m is the order of Bragg diffraction, λ is the operating wavelength, and n_{eff} is the effective-mode refractive index. The Bragg diffraction takes place when the forward and backward waves interact inside the cavity. The schematic of a typical index-guided DFB waveguide is illustrated in Fig.3.1.

3.2.1 Coupled Mode Theory

The time-independent wave equation is

$$\nabla^2 E + \epsilon(x,y,z)k_0^2 E = 0 \tag{3.2}$$

Here $k_0 = 2\pi/\lambda$ is the wave number and ϵ can be written as

$$\epsilon(x,y,z) = \epsilon_0(x,y) + \Delta\epsilon(x,y,z) \tag{3.3}$$

where $\epsilon_0(x,y)$ is the average value of ϵ and $\Delta\epsilon$ is the dielectric perturbation caused by the grating corrugation. To solve this problem, let us first consider the case of $\Delta\epsilon$=0, i.e., in the absence of perturbation. The general solution of Eq.(3.2) takes the form

$$E(x,y,z) = \hat{x}U(x,y)[E_f exp(i\beta z) + E_b exp(-i\beta z)] \tag{3.4}$$

where $U(x,y)$ can be obtained from solving

$$\frac{\partial^2 U}{\partial x^2} + \frac{\partial^2 U}{\partial y^2} + [\epsilon_0(x,y)k_0^2 - \beta^2]U = 0 \tag{3.5}$$

for a given device structure, and where β is the mode-propagation constant. It can be expressed as

$$\beta = n_{eff}k_0 - i\alpha/2 \tag{3.6}$$

where α is the mode-gain coefficient given by

$$\alpha = \Gamma g - \alpha_{int} \tag{3.7}$$

Γ is the confinement factor, g is the active-region gain, and α_{int} accounts for the internal loss.

In the presence of dielectric perturbation $\Delta\epsilon$, the amplitude of E_f and E_b of the forward and backward waves become z-dependent. Assume the weak perturbation

$\Delta\epsilon$ so that the spatial field distribution $U(x,y)$ is not affected. Substitute Eq.(3.4) in Eq.(3.2) and allow for slow axial variations of E_f and E_b. Multiplying the resulting equation with $U(x,y)$ and integrating over x and y, we obtain

$$\frac{dE_f}{dz}exp(i\beta z) - \frac{dE_b}{dz}exp(-i\beta z) = \frac{ik_0^2}{2\beta}\int\int \Delta\epsilon(x,y,z)U^2(x,y)\times$$

$$[E_f exp(i\beta z) + E_b exp(-i\beta z)]dxdy \tag{3.8}$$

Since $\Delta\epsilon$ is periodic in z with the grating period Λ, it can be expanded in a Fourier series to

$$\Delta\epsilon(x,y,z) = \sum_{l\neq 0} \Delta\epsilon_l(x,y)exp[i(2\pi/\Lambda)lz] \tag{3.9}$$

Substitue Eq.(3.9) into Eq.(3.8) and equate the coefficient of exp($\pm$iβz) on both sides. Assume for simplicity that $\Delta\epsilon$ is real and collect only the terms that are approximately phase-matched, we obtain

$$\frac{dE_f}{dz} = i\kappa E_b exp(-2i\Delta\beta z)$$

$$\frac{dE_b}{dz} = i\kappa^* E_f exp(2i\Delta\beta z) \tag{3.10}$$

and

$$\Delta\beta = \beta - m\pi/\Lambda = \beta - \beta_0 \tag{3.11}$$

is the phase mismatch and was assumed to be smallest for the term $l = m$ in Eq.(3.9). The contribution of the rest of the terms can be neglected due to their large phase mismatch. The coupling coefficient κ is defined as

$$\kappa = \frac{k_0^2}{2\beta}\frac{\int\int \Delta\epsilon_m(x,y)U^2(x,y)dxdy}{\int\int U^2(x,y)dxdy} \tag{3.12}$$

This equation means that the Fourier component $\Delta\epsilon_m$, for which the Bragg condition ($\beta \cong \pi/\Lambda$) is approximately satisfied, couples the forward and backward propagating

waves. It is called index-guided DFB if κ is real or gain-guided DFB if κ is imaginary. Otherwise, it is complex-guided DFB if κ is complex.

Instead of using complex β as the propagation constant in Eq.(3.2), it is easier to write the axially varying field in terms of the Bragg number $\beta_0 = m\pi/\Lambda$.

$$E(z) = A(z)exp(i\beta_0 z) + B(z)exp(-i\beta_0 z) \tag{3.13}$$

where

$$A(z) = E_f exp(i\Delta\beta z)$$

$$B(z) = E_b exp(-i\Delta\beta z) \tag{3.14}$$

Then the coupled-wave equations in Eq.(3.10) become

$$\frac{dA}{dz} = i\Delta\beta A + i\kappa B$$

$$-\frac{dB}{dz} = i\Delta\beta B + i\kappa A \tag{3.15}$$

A general solution of these equations can be expressed as

$$A(z) = A_1 exp(iqz) + A_2 exp(-iqz)$$

$$B(z) = B_1 exp(iqz) + B_2 exp(-iqz) \tag{3.16}$$

where q is the complex wave number to be determined from the boundary conditions. The constants A_1, A_2, B_1, and B_2 are interdependent. Substitue these general solutions to Eq.(3.15) and equate the coefficients of $exp(\pm qz)$, we obtain

$$(q - \Delta\beta)A_1 = \kappa B_1$$

$$(q + \Delta\beta)B_1 = -\kappa A_1$$

$$(q - \Delta\beta)B_2 = \kappa A_2$$

$$(q + \Delta\beta)A_2 = -\kappa B_2 \tag{3.17}$$

To obtain nontrivial solutions, a dispersion relation has to be satisfied.

$$q = \pm[(\Delta\beta)^2 - \kappa^2]^{1/2} \tag{3.18}$$

The plus and minus signs correspond to forward and backward propagating waves, respectively. The DFB reflection coefficient can be defined as

$$r(q) \equiv \frac{B_1}{A_1} = \frac{q - \Delta\beta}{\kappa} = -\frac{\kappa}{q + \Delta\beta} \tag{3.19}$$

Here the DFB reflection coefficient $r(q)$ is equivalent to the mirror reflection coefficient in F-P lasers. It is evident that the feedback mechanism is determined by the coupling coefficient κ. The general solution of the coupled-wave equations in Eq.(3.16) can be rewritten as

$$A(z) = A_1 exp(iqz) + r(q)B_2 exp(-iqz)$$

$$B(z) = B_2 exp(-iqz) + r(q)A_1 exp(iqz) \tag{3.20}$$

Therefore, the solution for an infinite DFB structure can be obtained as follows after substituting these equations into Eq.(3.13).

$$E(z) = A_1[exp(i\beta_0 z) + r(q)exp(-i\beta_0 z)]exp(iqz)$$

$$+ B_2[exp(-i\beta_0 z) + r(q)exp(i\beta_0 z)]exp(-iqz) \tag{3.21}$$

3.2.2 Threshold Condition

In reality, the finite-length laser cavity and the end-facets will alter the boundary conditions and thus, affect the laser characteristics. Consider a laser of length L. Since L is not necessarily an exact multiple of the grating period Λ, the last period of the grating close to the facet is generally not complete. The phase shift in this

region plays an important role in determining the laser performance and should be properly accounted for. Now assume the effective facet reflection coefficient can be written as

$$r_j = R_j^{1/2} exp(i\phi_j)$$

$$j = 1, 2 \tag{3.22}$$

where R_j is the facet reflectivity and ϕ_j accounts for the round-trip phase shift in the last incomplete grating period. The boundary condition at the two facets are

$$A(0) = r_1 B(0)$$

$$B(L) = r_2 A(L) \tag{3.23}$$

Applying these equations to Eq.(3.20) and we can obtain the following equations :

$$(r_1 - r)B_2 - (1 - rr_1)A_1 = 0$$

$$(r_2 - r)exp(2iqL)A_1 - (1 - rr_2)B_2 = 0 \tag{3.24}$$

These equations have a consistent nontrivial solution only for values of q satisfying the eigenvalue equation

$$\left(\frac{r_1 - r}{1 - rr_1}\right)\left(\frac{r_2 - r}{1 - rr_2}\right) exp(2iqL) = 1 \tag{3.25}$$

This is the threshold condition for DFB lasers. Given a coupling coefficient κ and facet reflectivities $r_{1,2}$, a self-consistent solution q can be calculated along with

$$\Delta\beta = \pm(q^2 + \kappa^2)^{1/2} \tag{3.26}$$

For a uniform DFB gratings, there are always two stable modes in the cavity as inferred in the above equations ($\pm$). An alternative, which can eliminate this double modes and excite only one stable mode, is to created a phase shift grating in the

center. The optimum phase shift is $\pi/2$. This can be understood as combining two uniform grating DFB together with an abrupt phase change in the center (180° in this caase). The net coupling coefficient κ is zero ($\kappa_+ + \kappa_- = 0$) and thus, only a single solution ($q = \Delta\beta$) can exist in the cavity from Eq.(3.26). This idea was first proposed by Haus and Shank [41] and is well-known as $\lambda/4$-shifted DFB lasers. The DFB threshold condition together with the material threshold gain

$$g_{th} = \frac{\alpha + \alpha_{int}}{\Gamma} \tag{3.27}$$

decides the overall laser threshold condition.

3.2.3 Calculation of the Coupling Coefficient

Refer to Eq.(3.12) and the notation in Fig.3.1, and assume the grating is laterally uniform so that the dielectric perturbation $\Delta\epsilon_m$ is independent of x. The κ can be rewritten as

$$\kappa = \frac{k_0}{2n_{eff}} \frac{\int_{-\infty}^{\infty} \Delta\epsilon_m(y)\phi^2(y)dy}{\int_{-\infty}^{\infty} \phi^2(y)dy} \tag{3.28}$$

here $\phi(y)$ is the field distribution in transverse direction. The Fourier component $\Delta\epsilon_m$ for the mth-order Bragg diffraction can be calculated as

$$\Delta\epsilon_m(y) = \frac{1}{\Lambda}\int_0^{\Lambda} \Delta\epsilon(y,z) exp(\frac{-2\pi imz}{\Lambda})dz \tag{3.29}$$

Hence, we can deduce several considerations to increase κ. Square gratings generally give the largest Fourier coefficient [42] and, therefore, are preferrable. This can only be produced by dry etching techniques. First order (m=1) gratings can significantly increase the κ as well. This inevitably, of course, adds more difficulty in lithography. In addition, deeper gratings (larger d_g) are an another way to improve the coupling coefficient. However, special care must be taken during the grating etching so that the defects generated during etching gratings will not affect the laser active region too much.

3.3 Heterostructure Design

The laser heterostructure , shown in Fig.3.2, was grown by metal-organic vapor phase epitaxy (MOVPE) on (100) semi-insulated InP substrate. Again, the tunneling injection structure is incorporated in the design and the corresponding conduction band diagram is shown in Fig.3.3. The 1000 Å InGaAsP (λ_g = 1.40μm) inner cladding, 30 Å InP tunneling barrier, together with the 5 quantum wells form a close system, which is solved by the Schrodinger equation. The inner cladding layer and the quantum well barrier are chosen such that the energy separation of the tunneling eigenstate and the quantum well ground states is about 30 meV, which is roughly the optical phonon energy in InP. The tunneling injection mechanism is assisted through longitudinal optical (LO) phonon resonance [35]. The quantum well sizes are properly chosen so that the wavefunction are uniformly distributed over the entire active region.

The active region consists of five 1 % strain-compensated quantum wells [80 Å InGaAsP (with a strain of +1.0 %) wells and 70 Å InGaAsP (with a strain of -1 %) barriers] with a photoluminescence (PL) peak calibrated at 1.53–1.54 μm. From the threshold gain point of view, 1 % strain-compensated quantum well is believed to be the optimum choice in 1.55μm range according to some experimental results and theoretical calculations [43]-[45]. In the multiwavelength DFB laser arrays applications, compressive-strained multiple quantum well active layers are more favorable since they have wider optical gain spectrum and thus, a wider wavelength span can be obtained [46].

For the real device, the depth of the ridge waveguide is targeted around 0.1–0.2 μm above the 0.2 μm InGaAsP (λ_g = 1.10μm) buffer layer. The DFB gratings

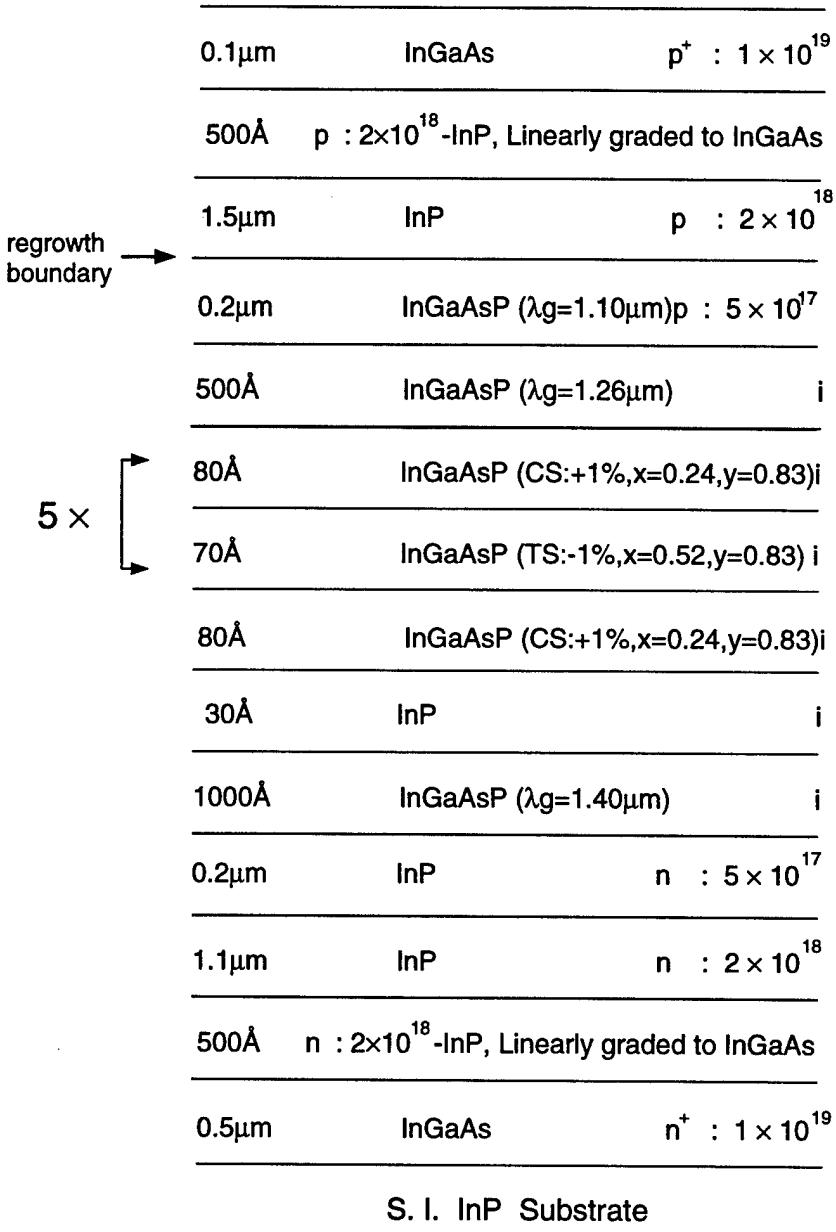

Figure 3.2: TI-MQW DFB laser heterostructure grown by MOVPE.

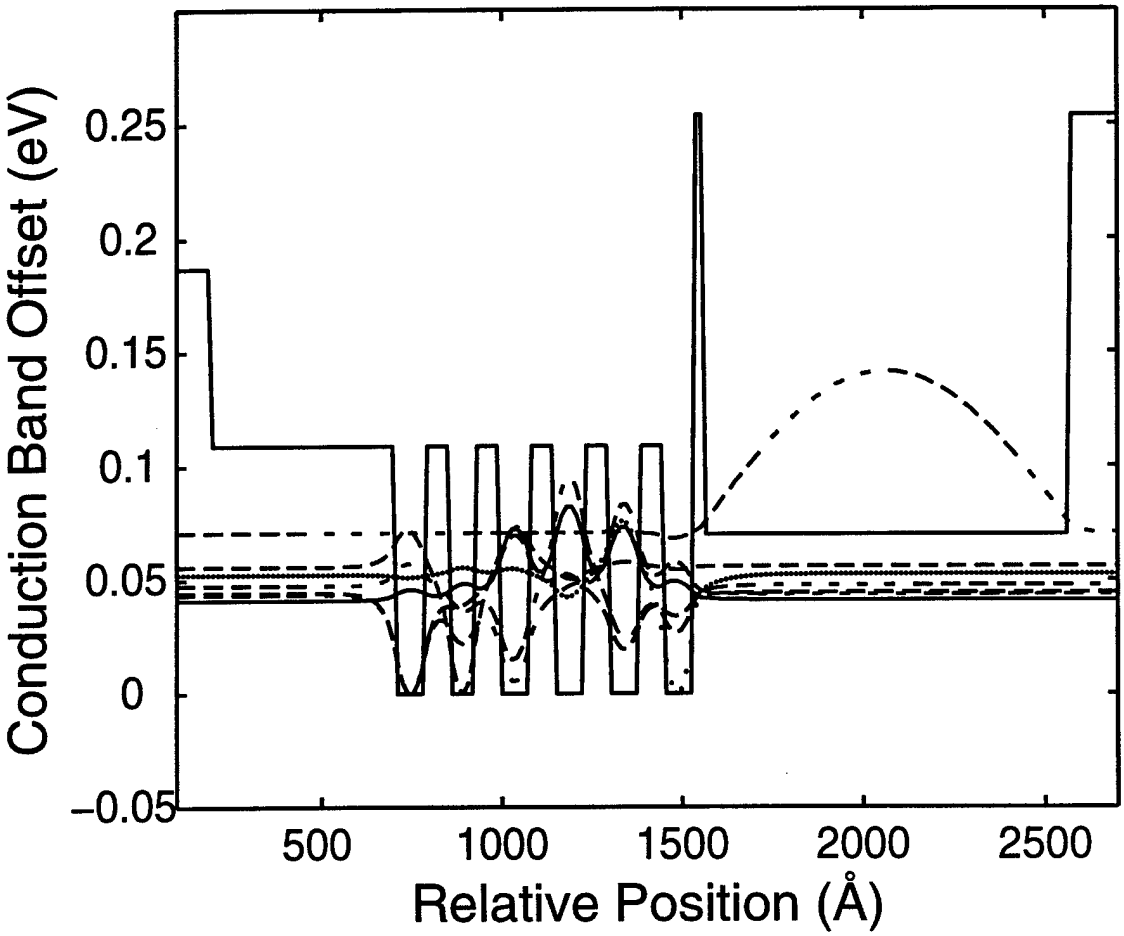

Figure 3.3: TI-MQW DFB laser conduction band diagram.

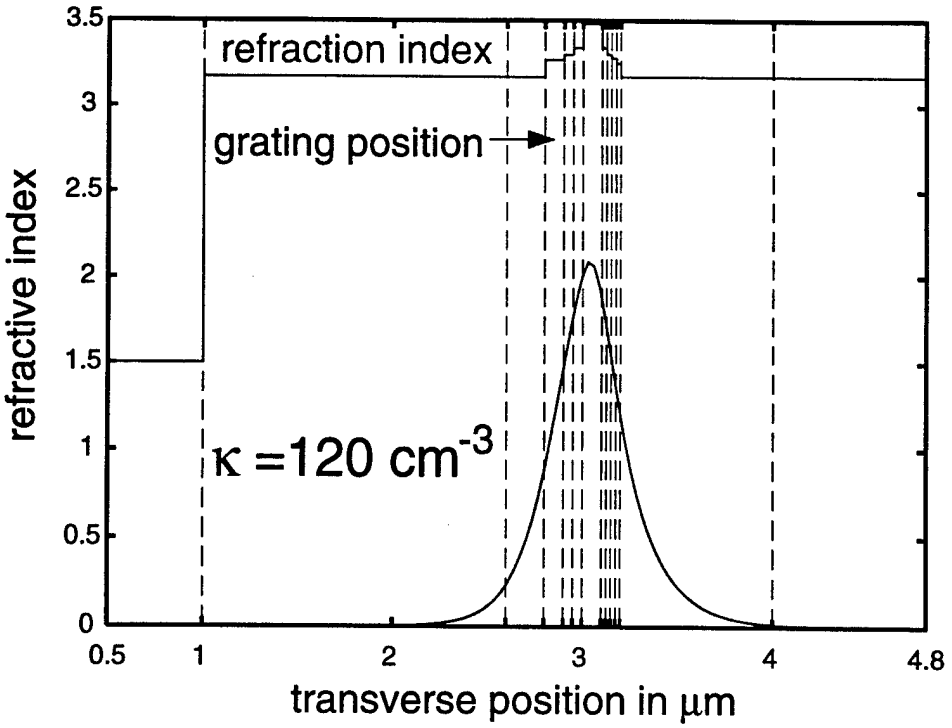

Figure 3.4: Calculated transverse mode profile.

are formed on this buffer layer. This ridge waveguide structure gives a propagation constant β=13.11 and the corresponding effective refractive index n_{eff}=3.23. For the 1.55 μm emission wavelength operation, the first-order grating period Λ is 240 nm. Figure 3.4 give the calculated mode profile in transverse direction. The goal is to achieve a low threshold gain in short cavity devices ($\sim$ 200μm long). Equivalently, the κL is shooting at 2–3. This means a very large $\kappa \geq 100\ cm^{-1}$ is needed. From the calculated transverse mode profile and the formula given above, the grating depth is around 800 Å deep. This would give a κ about 150 cm^{-1}. In reality, the regrowth roundoff and imperfection etching on the DFB grating will cause at least a 60–70 % degradation on κ [42]. Therefore, the actual coupling coefficient κ is estimated to be around 100 cm^{-1}. However, special care should be taken to assure that this relatively deep etch will not cause severe damages to the active region. To assure

a high performance working device, a low surface damage or damage-free etching technique is essential.

3.4 Device Fabrication

The entire DFB laser processing procedure is almost identical to the ridge waveguide laser except for some key steps: electron-beam lithography, low damage or damage-free etching, and regrowth. First, the sample was grown up to the InGaAsP ($\lambda_g = 1.10\mu$m) buffer layer. Then, the DFB gratings were formed on this buffer layer. In this work a direct e-beam writng and RIE etching were performed to generate the gratings. Next, an InP upper cladding layer and InGaAs cap layer are regrown on the sample. Finally, the standard ridge waveguide laser processing procedure was carried out to fabricate the device.

3.4.1 Electron Beam Lithography

There are several different techniques to generate the grating patterns: 1) stepping the window mask during multiple holographic exposures [47], 2) e-beam direct writing [48], 3) exposing an e-beam-generated grating mask with X-ray [49]], and 4) exposing an e-beam-generated phase mask with UV light (near-field holographic printing) [50]. In this work, direct e-beam writing technique was adopted since it provides more flexibility to vary the pitch distance. On the other hand, it is time-consuming and is not suitable for low-cost production. The direct electron beam writing technique was used in this work to generate grating patterns.

Electron Beam Lithography utilizing a single layer of 2% 950K polymethylmethacrylate (PMMA) was used to direct write the DFB grating structure. Since PMMA has relatively poor dry etch resistance, a lift-off mask was employed. After exposures and development in a solution of methylisobutylketone and isopropanol

(1:3) 30nm of titanium (Ti) was deposited and lifted off. Several factors related to the fabrication of a first-order grating structure were investigated in order to realize exact line/space relationship and grating uniformity. Parameters especially critical to the fabrication of this device concern electron beam diameter, off-axis scan distortions, field scaling errors and thermal instabilities.

Exposures of the resist were done with a JEOL JBX 5DII-U Electron Beam Lithography System in 4th lens mode. The grating lines were aligned in the $< 01\bar{1} >$ direction so that the waveguides can be formed in the $< 011 >$ on the grown wafer. Electron beam diameter is determined by accelerating voltage, beam current and final aperture size. Final parameters established were at 50KeV, 25pA and 180μm, respectively. Field scaling errors were reduced by scaling to a larger field size (800μm) and then limiting the writing area to 500μm. Each DFB structure was limited to a maximum 500μm cavity length to eliminate associated errors and to also obtain the best line width uniformity. Thermal instabilities induce positional beam drift that can be detrimental to DFB performance. As little as a 2 degree difference in temperature between the substrate and the E-beam System stage will result in significant pitch errors primarily due to positional beam drift. This problem can easily be corrected by implementing a delay that will allow the sample temperature to stabilize. Figure 3.5 shows a microphotograph of an e-beam written grating pattern. The quarter wavelength phase shifted position is also labeled.

3.4.2 Etching of Gratings

Etching the gratings is the most critical step in the DFB laser process. The surface damage due to the etching is always a concern for making a laser. In the early time people sometimes use chemical wet etch to form the gratings [42]. Wet etch has

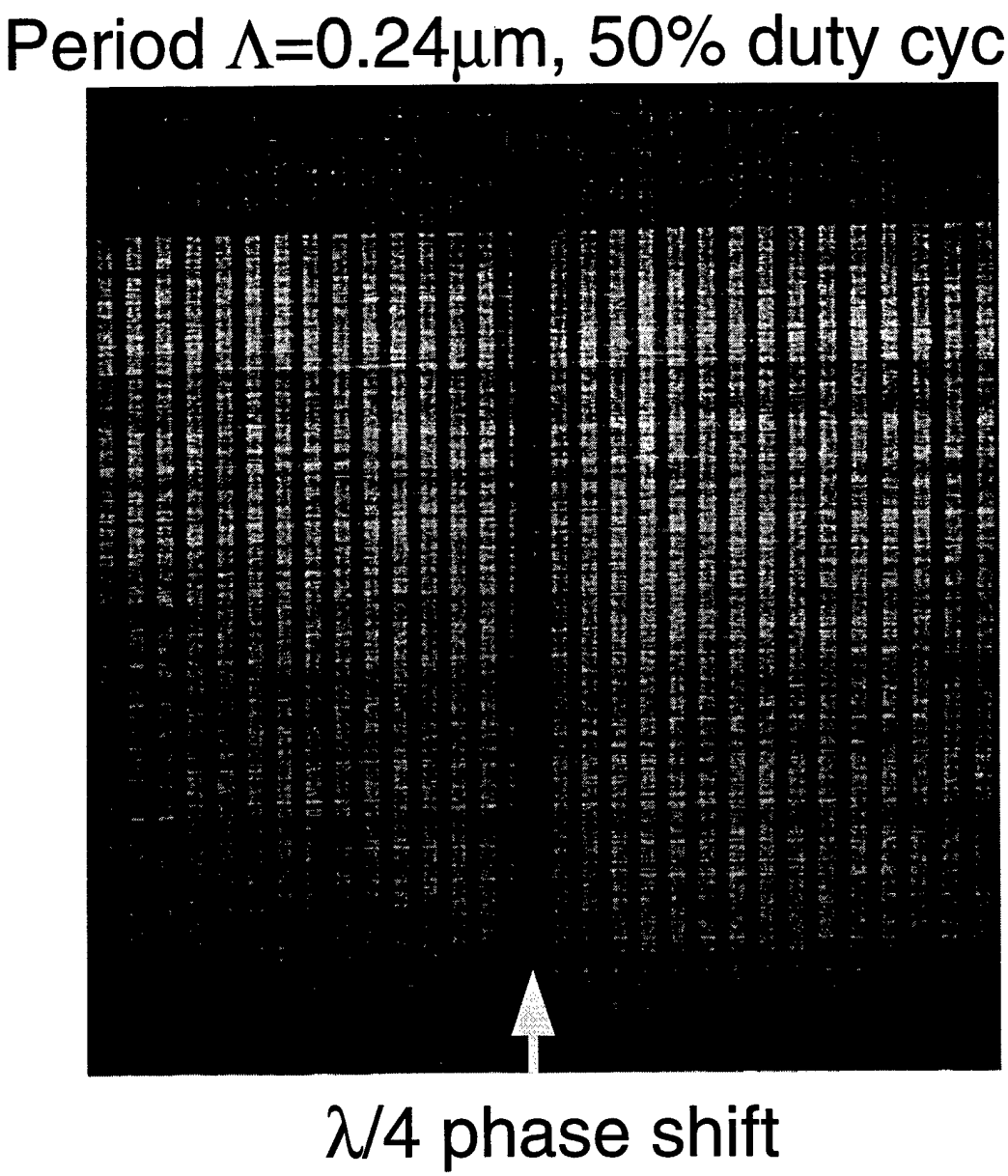

Figure 3.5: E-beam written gratings.

been a favorable choice for producing a damage-free surface. However, the inevitable undercut profile reduces the coupling coefficient dramatically. Furthermore, it can only be used in the higher-order grating cases. For the first-order DFB gratings cases, wet etch will smear out the corrugation features unless dry etch techniques are performed.

In this work reactive ion etching (RIE) is adopted in generating the first-order gratings due to its anisotropic property. Noncorrosive methane-hydrogen mixture [51],[52] has been widely reported to be an effective etchant to InP-based compounds in the plasma chamber. Normally a higher etch rate can be obtained by adding argon to the mix. The addition of argon, however, will increase the surface damage, which is prohibited in this application. The chemical reations taking place in the RF excited plasma are thought to be:

$$CH_4 \; -- \gg \; xCH_3^* + yCH_2^* + zCH^* + ions$$

$$H_2 \; -- \gg \; x'H_2^+ + y'H^* + protons \tag{3.30}$$

The methane and hydrogen split apart to form methyl and hydrogen groups. When reacted with the InP-based materials, the end products are methyl-indium or methyl-gallium compounds and hydrides such as phosphine or arsine, reversing the OMVPE process.

$$In + 3CH_3^* \; -- \gg \; In(CH_3)_3$$

$$P + 3H^* \; -- \gg \; PH_3 \tag{3.31}$$

Several test runs were conducted to determine the optimum etching condition. The gas mixture employed in these test are 15% methane and 85% hydrogen with the chamber pressure maintained at 15–20 mT. An InGaAsP ($\lambda_g = 1.1\mu$m) layer on InP substrate was etched by the RF powers of 150 W, 100 W, and 50 W, respectively.

An 0.5μm InP cap layer is then regrown on the etched sample. Compared with the original unetched InGaAsP ($\lambda_g = 1.1\mu$m) sample, the PL intensity of the regrown sample drops to 1/20 and 1/12 of the original intensity for the 150 W case and 100 W case, respectively. The 50 W case followed by a short wet etch sample preserves about the sampe order of PL intensity and is believed to be applicable in fabricating the lasers.

In order to minimize the surface damages, a combination of dry etch (RIE) and wet etch was adopted for the real device fabrication. A InGaAsP ($\lambda_g = 1.1\mu$m) layer was first etched 600Å thick by RIE ($CH_4 : H_2 = 6 : 34$, 20mT, and RF power is 50 W) and followed by a wet chemical etch (saturated bromine water : HBr : D.I. water) to remove another $\sim$ 400Å. The regrowth during heating the sample then rounds off about 200Å, leaving the total grating depth about 700–800Å deep. It is believed that the damage will also be self-healed a little bit during MOCVD regrowth. Figure 3.6 illustrates a micrograph of the etched gratings.

3.4.3 Preparation for Regrowth

After forming the DFB gratings, the p-doped InP upper cladding layer and p^+ InGaAs contact layer are regrown by OMVPE. In order to ensure a good quality of regrowth interface without creating too many dislocations, special attention has to be paid in preparing the sample for regrowth.

The sample was regrown at Bellcore and the sample preparation procedures are as follows: soak the sample in boiling solvents (isopropanol, trichlorethylene, acetone, methanol), then rinse it and soak it in sulfuric acid for about 40 seconds, then rinse for a long time. Sulfuric acid does not etch, but has some kind of cleaning effect. In the case when the samples have been submitted to damaging processing (plasma for

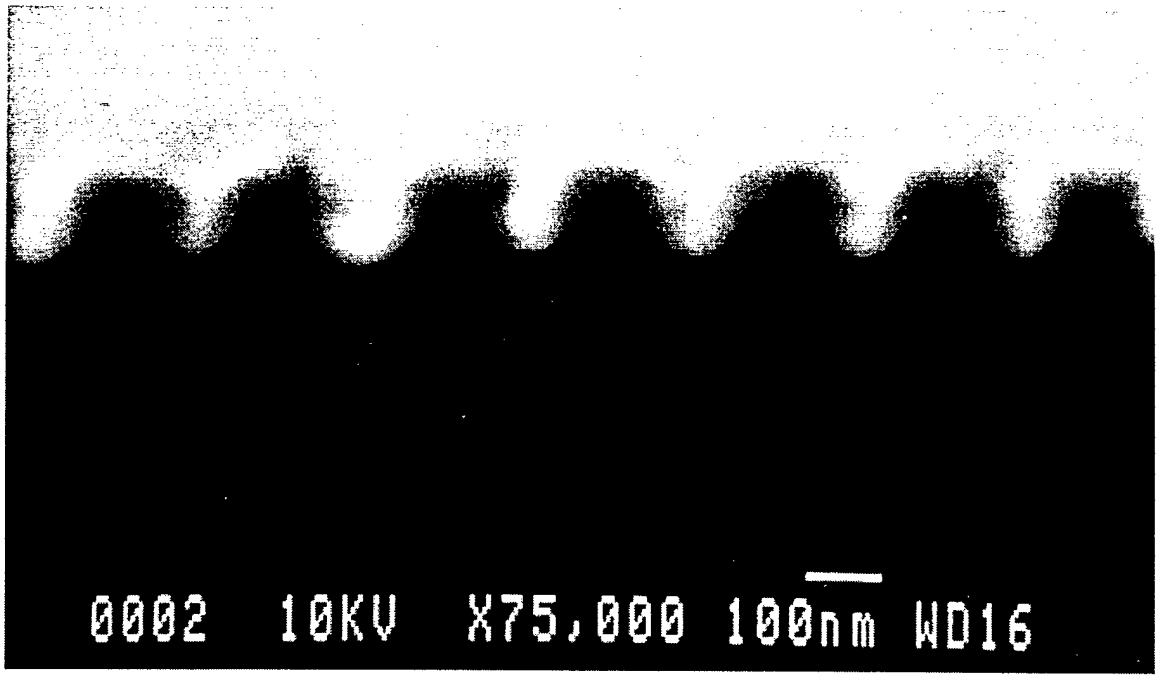

Figure 3.6: RIE and wet etched DFB gratings.

mask deposition or etching, ion beam, etc.), it is very beneficial to do 1/2 hour to 1 hour of Ultra-Violet Ozone cleaning before the sulfuric acid soaking.

3.4.4 Ridge Waveguide Laser Processing

After regrowing the top cladding layer and cap layer, the area where the gratings were formed can vaguely be seen. The waveguides were aligned on top of the grating areas, as shown in Fig.3.7 and the p-contact metal (Pt/Ti/Pt/Au) was then deposited. The ridge was formed by RIE (CH_4:H_2:Ar=6:56:4, 15mT, 150 W) and wet chemical (HCl:H_3PO_4) etching. After the etching, the sample was annealed at 430–450°C for 60 seconds to form a good ohmic contact as well as to drive off the residue hydrogen level during the RIE etching, which can degrade the device optical performance seriously. A mesa, down to the the bottom contact layer is formed by wet chemical etching and this is followed by evaporation of Ni/Ge/Au/Ti/Au as the n-contact metal. The ohmic contact is formed by annealing at $\sim$ 400°C. Finally, thick

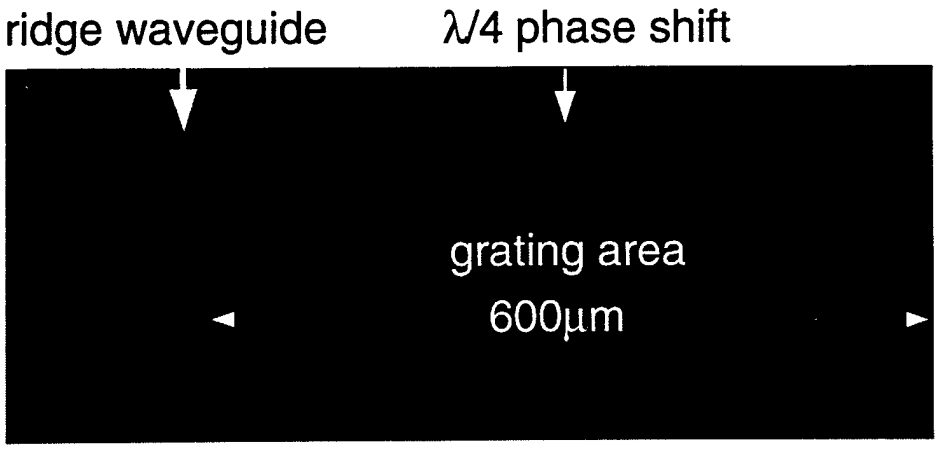

Figure 3.7: Formed ridge waveguide on top of the etched grating area. Note that the $\lambda/4$-shifted position is located at the center of the waveguide.

interconnection metal pads (Ti/Al/Ti/Au) are deposited for measurement probing.

3.5 Device Performance

The un-coated lasers have threshold currents of 20–27mA for 200μm long devices, 22–30mA for 300μm long devices, and 28–34mA for 600μm long devices. The relatively high threshold current and poor slope efficiency is believed mainly due to the surface damage caused during grating formation. These wide ranges of I_{th} are due to the ambigious phase factors at the cleaved facets. A measured temperature dependent L-I characteristics for a 300μm long device is shown in Fig.3.8. The device can still lase up to 50°C. The relation between temperature and threshold current density is also depicted in Fig.3.9. From analyzing the data, the characteristic temperature T_0, obtained by fitting with the empirical relation:

$$I_{th} = I_0 exp(T/T_0) \tag{3.32}$$

is estimated to be 70–120K at room temperature. This is higher than most 1.55μm lasers and is believed to result from the tunneling injection mechanism.

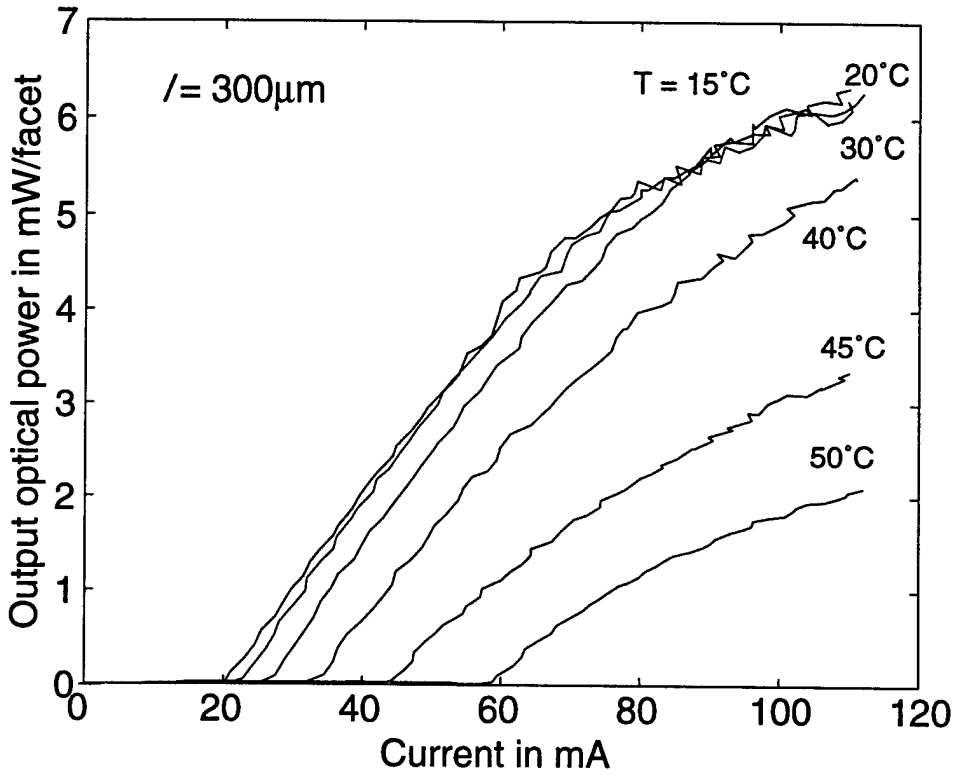

Figure 3.8: Measured DFB laser temperature dependent L-I characteristics.

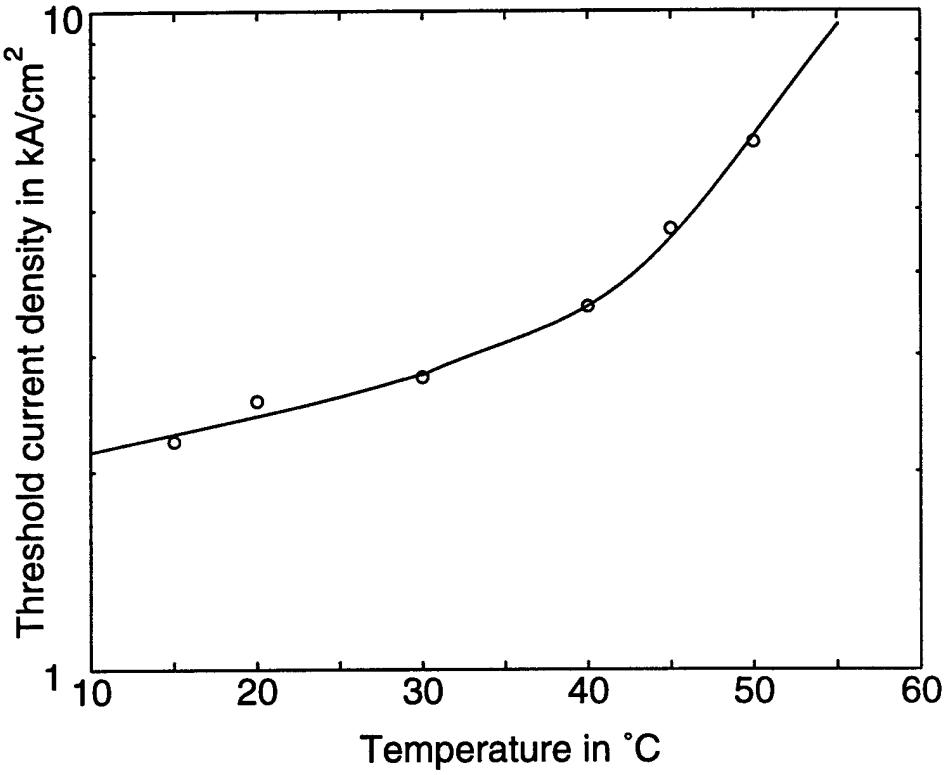

Figure 3.9: Measured TI-DFB laser threshold current density as a function of temperature.

To ensure that lasing is from the DFB mode, the temperature dependent spectral output is studied. Figure 3.10 shows the data taken from the spectrometer. The laser maintains the same single longitudinal mode while its wavelength shifts continuously at a rate of $\sim$1Å/°C, which is a typical value for DFB lasers. In the F-P laser, this number is $\geq$ 5Å [42]. This lasing wavelength shift is because the mode effective index varies with temperature. In the other words, the material effective bandgap shrinks as the temperature increases leading to this red-shift in lasing modes.

The laser shows a sidemode suppression ratio (SSR) of $\sim$ 30dB, from the output spectra shown in Fig.3.11. The device preserves single mode characteristics even up to 120mA as shown in Fig. 3.12. The red-shift in wavelength results from the carrier-induced bandgap narrowing effect. Another lasing spectrum taken from a uniform grating device, shown in Fig.3.13, indicates 2 stable DFB modes with $\sim$2 nm in separation, co-existing in the cavity beyond the threshold current. This phenomenon matches with the theoretical calculation for the uniform grating case. That is why for most practical applications, $\lambda/4$-shifted DFB laser is preferred to provide single mode operations [45]-[47]. However, the drawback is the severe spatial-hole burning under high level injection, which will generate multimode characteristics [53],[54]. This is because the mode intensity in $\lambda/4$ is highly non-uniform and peaks in the center of the cavity where the phase-shift region is located. Because of enhanced stimulated emission occurring near the cavity center, the gain, or equivalently the carrier density, is depleted more near the center than near the cavity ends.

The small-signal modulation of the lasers is characterized by a HP8510 network analyzer with a microwave signal supplied from HP8340B synthesized sweeper and the laser optical light output pigtailed into HP83420A lightwave test set. A 300μm long DFB laser diode small-signal modulation response at different bias levels under

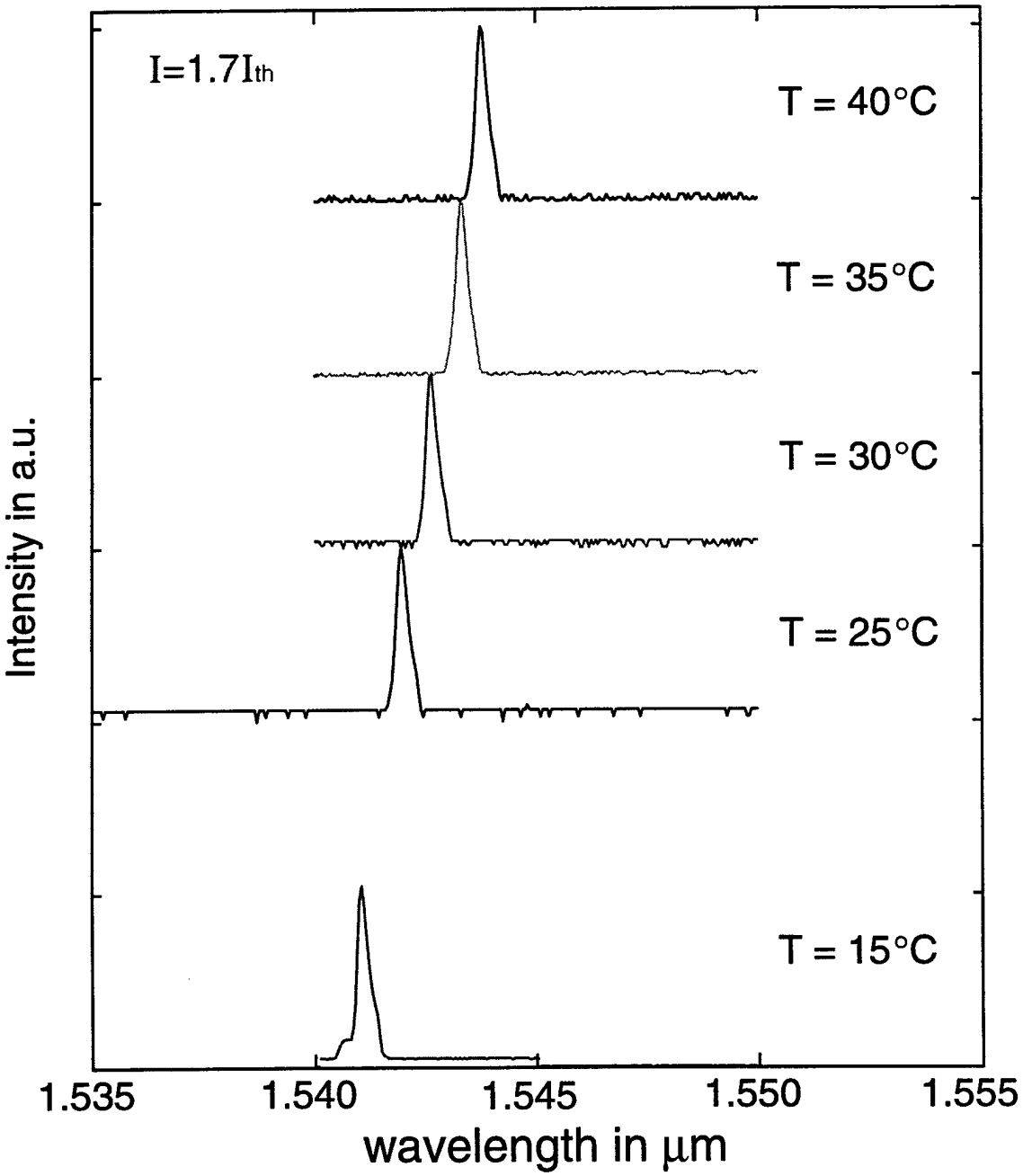

Figure 3.10: DFB laser temperature dependent spectrum.

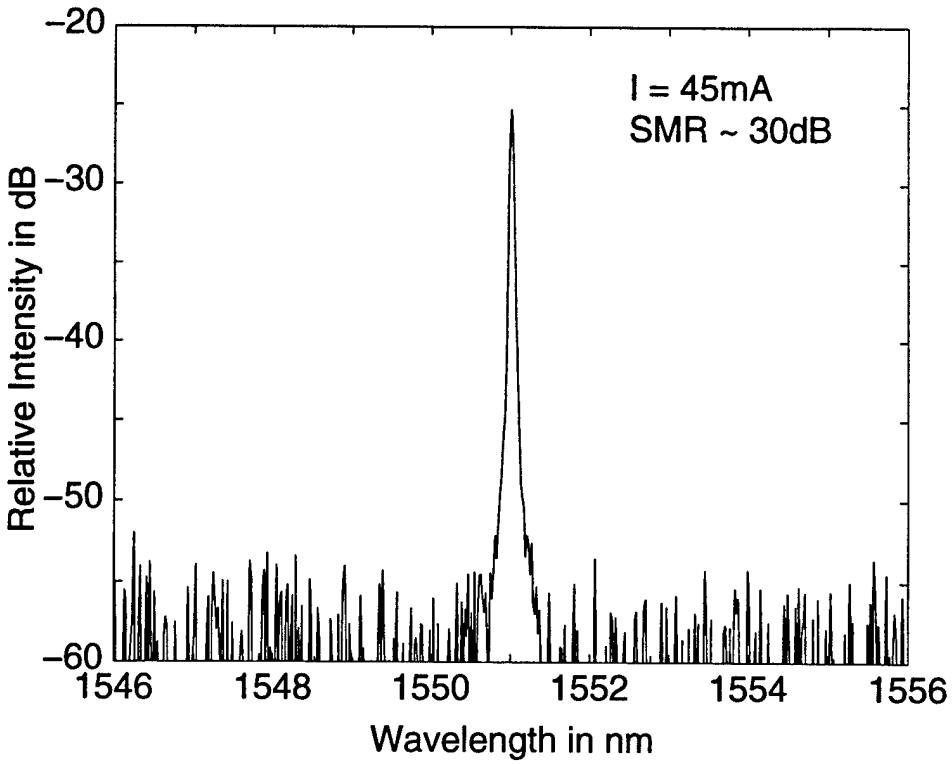

Figure 3.11: A typical DFB optical spectrum.

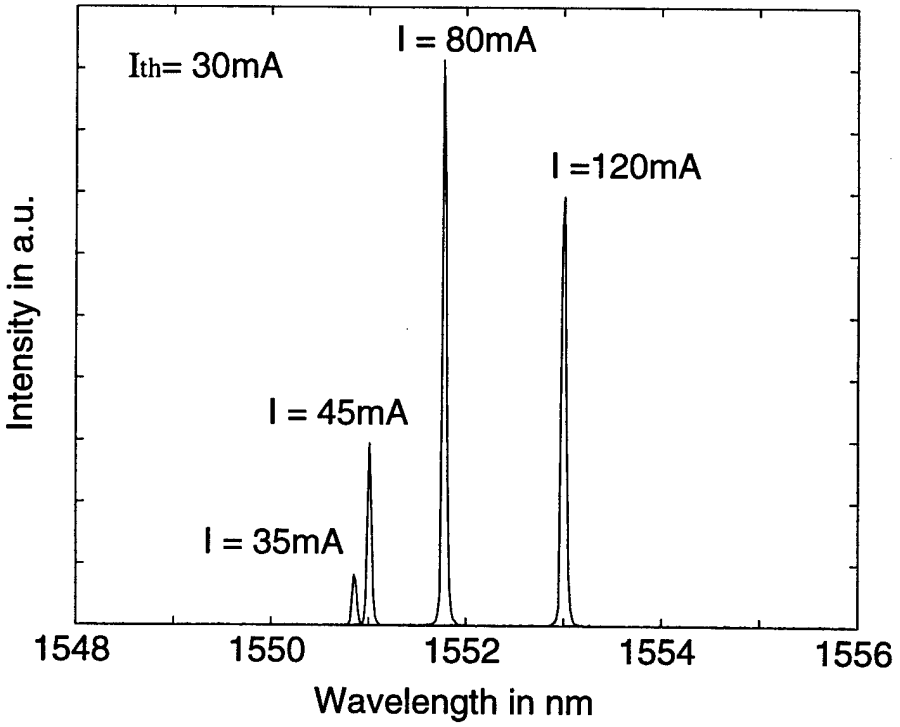

Figure 3.12: Current dependent DFB lasing spectrum.

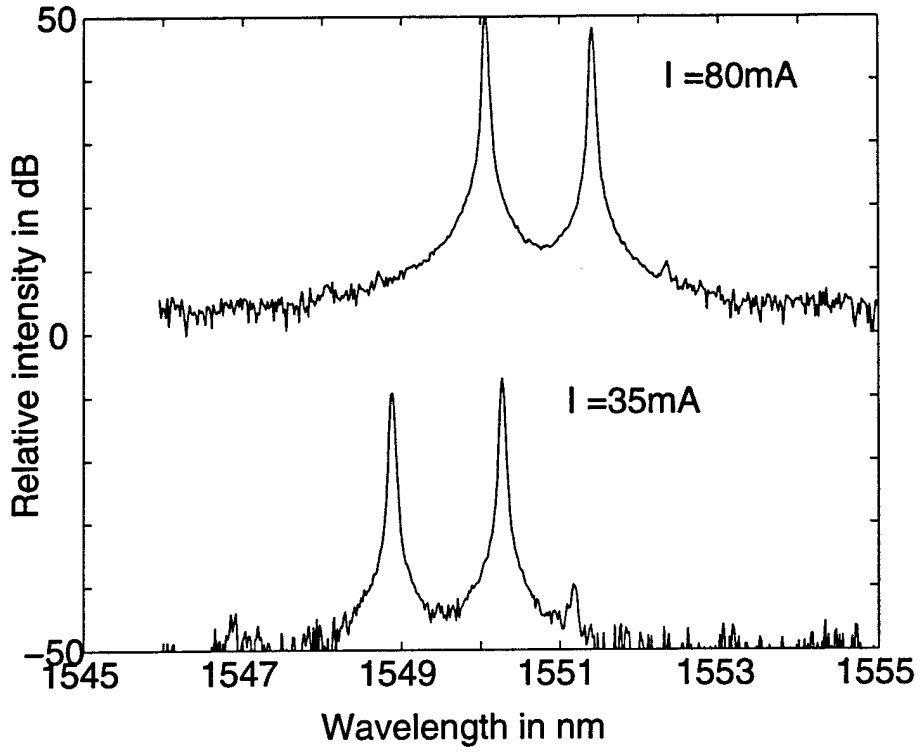

Figure 3.13: Two stable modes resonate in the laser cavity.

CW operation is shown in Fig.3.14. A maximum small signal modulation bandwidth of 7.5 GHz was obtained at a bias current of 90 mA. This relatively poor bandwidth is believed mainly due to the poor differential gain, which is caused by severe surface damage during grating formation.

The device microwave impedance characteristics are important parameters for the design of the driver circuits, to be discussed in Chapter 6. The measured device impedance characteristics, shown in Fig.3.15, indicate an equivalent resistance of $\sim 7\Omega$ when the laser is biased above threshold.

3.6 Summary

A tunneling injection DFB laser at 1.55μm is demonstrated for the first time. Perliminary results were characterized and analyzed. An effective device fabrication

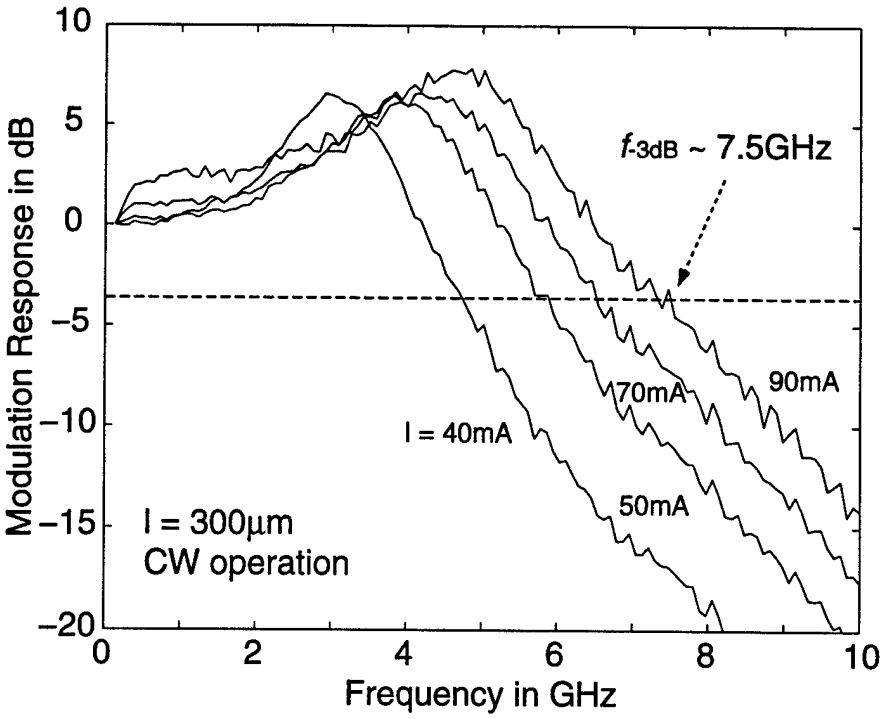

Figure 3.14: Measured DFB laser small-signal modulation response under CW operation.

processing procedure has been developed. Typical threshold currents are between 25–35mA for 200–400μm long uncoated devices. Stable single longitudinal modes have been observed and can be preserved up to 120mA in $\lambda/4$-shifted DFB lasers. The laser shows a temperature tunability of 1Å/°C. The relatively high threshold current and poor modulation bandwidth are believed due to the surface damage during etching the gratings. Also, the lasing linewidth appears to be a little bit wider and is believed primarily to be due to slight-nonuniformity in the gratings. Due to limited resolution ($\sim$ 0.2Å) of our optical spectrum analyzer, the laser linewidth cannot be determined precisely, as an accurate measurement of the linewidth has to be done by interferometric techniques. Nonetheless, the laser characteristics are suitable for short-haul ($\leq$ 100km) WDM links.

Further investigation in fabrication techniques, such as development of an low

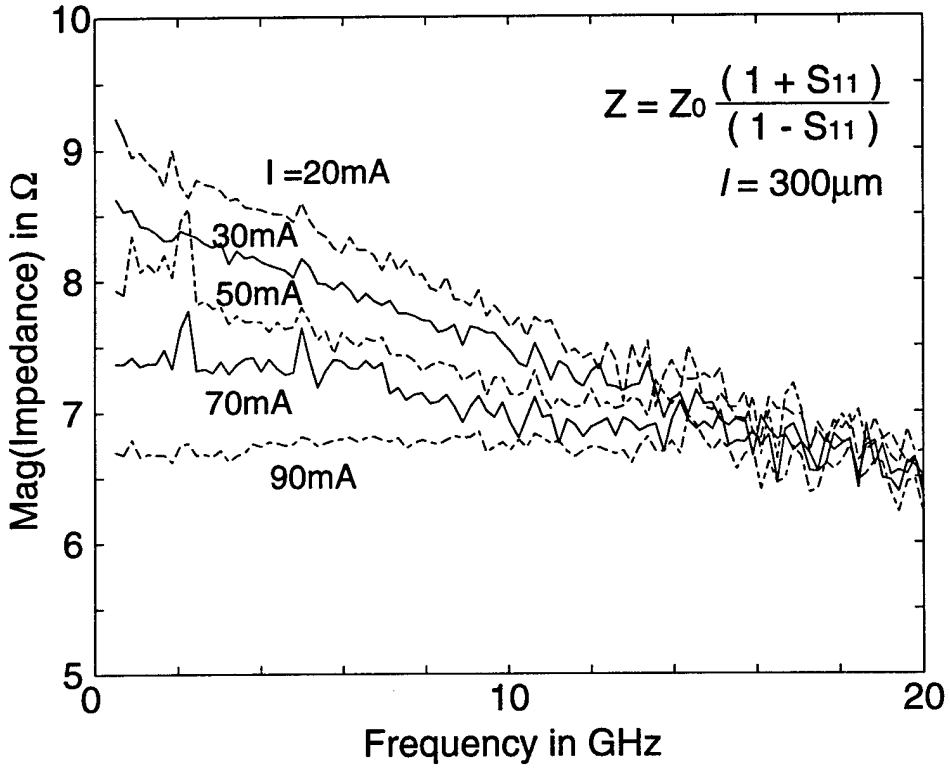

Figure 3.15: Measured DFB laser diode impedance characteristics.

surface damage or damage-free dry etching recipes for generating the DFB gratings, and improvement of e-beam lithographic technology to produce high throughput and large area uniform grating patterns, is needed to improve the device performance. Besides, effective measurement techniques are necessary to carefully characterize the device performance. These include laser linewidth, coupling coefficient, chirp parameters, and large signal modulation in long distance transmission.

Recently, the research trends have been shifting towards complex-guided [55], chirped grating [56], or multi-section DFB lasers [57],[58], which have been experimentally and theoretically demonstrated to have great potential in producing narrower linewidth, high yield of single frequecy operation, and wider tunable range in lasing wavelengths.

CHAPTER IV

InAlAs/InGaAs Quantum Confined Stark Effect Modulators

4.1 Introduction

External modulation of light sources at high frequencies, or bit rates, is being investigated as a viable alternative to internal (current) modulation of lasers, where chirp can be quite severe. The electroabsorption-type semiconductor modulator, particularly a multiple quantum well (MQW) structure, using the change of bandgap energy due to an applied electric field have advantages over electro-optical modulators (e.g., $LiNbO_3$ or Nd:YAG) [59] because they can achieve high-speed modulation and large extinction ratio under a relatively low driving voltage and have much smaller size. Furthermore, they can be monolithically integrated with laser diodes. MQW modulators, known also as quantum confined Stark effect (QCSE) modulators, show promising performance and have become the most important candidate for use in the next generation lightwave communication systems.

Compared with other material systems compatible with InP, suitable in the 1.5μm regime, InAlAs/InGaAs heterostructures have a large conduction band offset and a small valence band offset ($\Delta E_c : \Delta E_v = 0.5\text{eV} : 0.2\text{eV}$). These properties allow the incorporation of wider well widths than with InGaAsP/InP heterostructure systems

($\Delta E_c : \Delta E_v \sim 0.35\text{eV} : 0.65\text{eV}$) [60]-[63], while maintaining a strong exciton binding energy and quantum confined Stark effect (QCSE). Furthermore, the carrier pile-up effects [64],[65], which have a significant influence on the modulation bandwidth and power handling capability, can be expected to be small because of the smaller valence band offset.

In this chapter, the physics of QCSE is briefly reviewed first, followed by discussion of some of the considerations in designing modulators. Next, the design and fabrication of InAlAs/InGaAs waveguide modulators are described along with some of the device performance. Finally, a novel technique to reduce photocurrent responsivity by doping the quantum wells with erbium is demonstrated with a GaAs-based device. This device has a photocurrent responsivity (0.005 A/W) two orders of magnitude lower than conventional devices and solves a serious system problem. The large photoresponsivity of QCSE modulators translates to a large power drain in systems using these devices. The Er-doped modulator demonstrated here solves this problem effectively for the first time [62].

4.2 Physics of QCSE

In semiconductors, some very important properties are modified by carrier interactions. The electron-hole interaction is important for optical properties of semiconductors and devices with strong charge injection. This electron-hole system, coupled through Columbic interaction, is called exciton. The exciton binding energy E_{ex} can be calculated by employing an analogy with the Bohr hydrogen atom model [66].

$$E_{ex}^{l} = \frac{-m^{\star}q^4}{32\pi^2(\epsilon_r\epsilon_0\hbar)^2}\frac{1}{l^2} \tag{4.1}$$

where $m^{\star}$ is the reduced effective mass of the exciton and l is an integer (l=1,2,3,...). The appearance of electron-hole pairs, or excitons, modifies the original unperturbed

bandstructures, and thus alters the material optical transition characteristics. The optical excitation and formation of excitons generally manifest themselves as a series of sharp resonances (peaks) at the low energy side of the band edge.

In bulk materials, these excitonic peaks can only be observed in very pure samples at low temperature due to their rather small binding energy. The excitonic state can be ionized by applying an electric field or increasing the temperature causing the excitonic peaks to merge with band-to-band transition [67].

In the past few years, however, advances in material growth and processing techniques have made it possible to fabricate smeiconductor layers, like quantum wells, with unprecedented precision. For example, molecular beam expitaxy (MBE) [68] and metalorganic chemical vapor deposition (MOCVD) [69] have demonstrated the capability to grow high quality semiconductor heterostructures with nearly atomically smooth interfaces. In quantum wells, electrons and holes behave in a two dimensional fashion and they are tended to become localized or confined in the state where their potential energies are the lowest. Unlike in the bulk materials, this confinement of electrons and holes in the quantum wells greatly increases the exciton binding energy along with the oscillator strength. Thus, the excitonic transition can be preserved up to a high temperature without merging into the band-to-band transitions [67].

Now focus our attention to the cases of quantum wells in presence of an electric field. The electric field can ionize the exciton states by pulling apart the electron hole pair and causes a broadening of the exciton peak as well as peaks shifting. In general, the electric field can be either longitudinal (in the plane of the well) or transverse (in the growth direction). The logitudinal field case is similar to the bulk case and the excitonic transition essentially disappears at a fairly low field ($\leq$ 10kV/cm). The

transverse case, on the other hand, is of great interest since the exciton will not easily be ionized since the electron and hole states are well confined in the quantum well. As a result, this exciton transition peaks can persist to electric fields of greater than 100kV/cm. This effect is known as Quantum Confined Stark Effect (QCSE).

When electric fields are applied to quantum wells, the energy term eEz should be added to the exciton Hamiltonian, which can be written as

$$H = H_0 + eEz \tag{4.2}$$

where H_0 is the usual quantum well Hamiltonian under no bias, E is the electric field applied in the quantum well region. To simplify the problem, here we only consider one dimensional case. The eigenfunctions of H_0 are ψ_n and in the square quantum well, the ground state function ψ_1 has an even parity so that the first order correction to the subband energy

$$\Delta E^{(1)} = \langle \psi_1 | eEz | \psi_1 \rangle \tag{4.3}$$

is zero. The second order correction then becomes the dominant term in this problem. For an infinite barrier quantum well and small field case, i.e.,

$$|eEW| \ll \frac{\hbar^2 \pi^2}{2m^* W^2} \tag{4.4}$$

where W is the well width, the second correction can be calculated as

$$\Delta E_1^{(2)} = \frac{1}{24\pi^2} \left(\frac{15}{\pi^2} - 1 \right) \frac{m^* e^2 E^2 W^4}{\hbar^2} \tag{4.5}$$

It shows that the energy shift of an exciton resonance peak is proportional to the fourth power of the well width. This suggests that a wider well size is preferred to obtain a better modulation. However, as the well width increases, the exciton absorption decreases. The optimum well sizes are around 90–120Å for InP-based materials [67]. In addition, the exciton effective mass m^* plays an important role.

Introducing some strain in the quantum wells is an another option in engineering the device performance [71],[72].

4.3 Design Issues

There are several figures of merit commonly used to evaluate the modulator performance. These figures of merit are strongly affected by some factors which are important considerations in designing a modulator. Tradeoffs are therefore needed, to meet certain requirements, in designing a modulator. The following sections discuss some of these figures of merit [73],[70].

4.3.1 ON/OFF Ratio

ON/OFF ratio is the most important characteristics for the intensity modulators and is given by the relation below:

$$R = exp(\Gamma \Delta \alpha L) \tag{4.6}$$

where Γ is the light confinement factor, $\Delta\alpha$ is the change in the absorption coefficient, and L is the interaction length between the light and the electroabsorption materials. For the transverse type (normal incident) modulators, Γ=1. Obviously, a longer interaction length L is needed to achieve a larger ON/OFF ratio R. The most intuitive approach is to increase the number of quantum wells. However, this is undesirable in most of the cases. First, as the thickness of the MQW active region increases, the applied voltage increases correspondingly. Second, from the material growth point of view, it is very difficult to control the material quality if too many periods of quantum wells are deployed. Typically, 50 or even more periods of MQW's are required to achieve sufficient ON/OFF ratio in the transverse type QCSE electroabsorption modulators, whereas the interaction length is only about 1μm. To

overcome this problem, waveguide modulators are proposed since they provide much longer interaction length (L could be $\sim 100\mu$m long). Thus, even though the confinement factor in the quantum well active region is very small ($\sim$ 0.1–0.01), 10–20 periods of quantum wells are adequate to achieve a ON/OFF ratio of 10–20dB easily. In addition, larger $\Delta\alpha$ is preferrable to increase ON/OFF ratio. This needs a high quality material which has sharper excitonic resonance peaks.

4.3.2 Insertion Loss

Insertion loss, normally defined as the ratio of the optical power at the output of the device to the power at its input, is another key parameter for any modulator. There are many sources of insertion loss and the main components associated with QCSE electroabsorption modulators we are interested in are mirror reflection loss, residual absorption loss, waveguide loss, and coupling loss. Mirror reflection loss can be eliminated by employing anti-reflection (AR) coatings on both facets to obtain a 3dB reduction in insertion loss. Residual absorption arises from the absorption of band tails of the quantum wells and free carrier absorption in the doped cladding layers. The former factor can be minimized by operating the device at a wavelength significantly longer than the zero-field bandgap. However, this would decrease $\Delta\alpha$ and maximum ON/OFF ratio. The optimum choice is to design the zero-field bandgap 30–50meV larger than the photon energy. Free carrier absorption can be reduced by lowering the doping density in the cladding layers. Besides, a shorter length can reduce the loss somewhat. Coupling losses between optical fibers and semiconductor waveguides, in general, account for most of the the insertion loss. The reason is the mismatch of mode profiles in fibers and waveguides. Typically, the tapered or microlensed fiber, used in coupling light into and out of the waveguide,

has a numerial aperture (N.A.) around 0.1–0.3. However, the typical N.A. for a semiconductor waveguide is greater than 0.3. Therefore, careful control of the mode profile in the waveguide design is essential to reduce the loss from mode mismatch. Increasing the thickness of the waveguide core region reduces the coupling loss, too. Currently, the state-of-the-art waveguide modulators reported have the insertion loss as low as 6–8dB for a cavity length around 100μ long.

4.3.3 Modulation Bandwidth

The electroabsorption modulator is generally operated in reverse bias region and can be best represented as a capacitor in series with a 50Ω source impedance (R). The modulation bandwidth is basically limited by the equivalent circuit electrical bandwidth and this is given as $f_{-3dB} = 1/(2\pi RC)$. In some cases, it becomes $1/(\pi RC)$ when the modulator is shunted with a 50Ω load resistor. Therefore, the limiting factor is the modulator equivalent capacitance C. Here $C = \epsilon A/d_i$, where d_i is intrinsic region, or MQW, thickness and A is the device area. To achieve high modulation bandwidths, a shorter or smaller device is necessary.

4.3.4 Power Dissipation

The modulator DC power dissipation is defined by the product of the DC bias voltage and photogenerated current. In the latter part of this chapter, a novel approach to reduce the photocurrent responsivity will be discussed. The RF drive power is given by $P_{ac}=V_{pp}^2/8R_L$ and V_{pp} is the peak-to-peak voltage swing. Obviously, from the above definitions, operating a modulator at a low bias voltage is a goal for low power consumption applications. Since energy shift of the exciton resonance peak is proportional to the fourth power of the well thickness, a wider well is preferred in the design. A thinner intrinsic region also benefits in reducing the drive voltage

since a larger electric field can be obtained at the same bias voltage based on the relation $E = V/d_i$.

4.3.5 Optical Power Handling Capability

In the communication systems, it is desirable to have an optical switch, or modulator, which can handle higher optical input power (i.e, larger input dynamic range) so that a lower bit error rate (BER) could be obtained at the receiving end due to a better signal-to-noise (S/N) ratio. However, both bulk and MQW electroabsorption modulators exhibit absorption saturation, which limits their ON/OFF ratio at high optical input intensities. In addition, at high intensities devices suffer a degradation in modulation bandwidth. In the absence of an electric field [74], this absorption saturation arises primarily from phase-space filling by photogenerated electrons and holes. In the presence of an electric field [110], on the other hand, this saturation results from screening of the applied electric field by trapped carriers through photogeneration, especially holes because of their larger effective mass and slower speed.

The solution is to design the quantum wells with a smaller valence band discontinuity (ΔE_v) at the heterojunction interface (typically, $\Delta E_v \leq 0.2$eV) such that the holes can escape from the quantum wells more efficiently [75].

4.3.6 Polarization Sensitivity

Today applications for MQW electroabsorption modulators range from multigigabit WDM and TDM, long-haul terrestrial and submarine fiber transmission systems to optical demultiplexing stages. Most of these applications, especially demultiplexing applications, require the modulator transmission to be insensitive to polarization because optical polarization control is very difficult to control in fiber transmission lines.

The solution to achieve polarization-independent modulation is to introduce tensile strain into the wells, taking advantage of the degeneracy of a heavy-hole and light-hole exciton peak of the MQW materials [76],[77]. To assure the material quality after introducing the tensile strain, however, the compressive barriers are preferred to obtain a net zero-strain in the active region. That is why most of the state-of-the art modulators adopt strain-compensation design. Several examples have been successfully demonstrated both in InAlAs/InGaAs and InGaAsP/InP MQW systems.

4.4 Waveguide of InGaAs/InAlAs Waveguide QCSE EA Modulators

4.4.1 Design

Based on the previous design issues and the advantages mentioned in the beginning, a InAlAs/InGaAs QCSE modulator with 0.5% strained-compensated MQW was designed and the heterostructure grown by MBE on the n^+ (100) InP substrate is shown in Fig.4.1. The calculated fundamental mode profile supported in the waveguide along the transverse direction is given in Fig.4.2. The designed waveguide cross section is also shown in Fig.4.3. The quantum well is designed and calibrated with an effective bandgap $\lambda_{PL} \cong 1.49\mu$m, which is about 32meV higher than the operating wavelength $\lambda = 1.55\mu$m.

4.4.2 Fabrication

The device processing procedure is as follows: first, a 3μm wide p contact metal (Pd/Zn/Pd/Au/Ni) was deposited on the wafer. The top Ni layer is used as an RIE etch mask while forming the ridge waveguide. The waveguide is formed by etching through the MQW active region to the lower InAlAs cladding layer with reactive ion etching (BCl_3 : Ar =40 : 40, chamber pressure is maintained at 40mT, RF power is

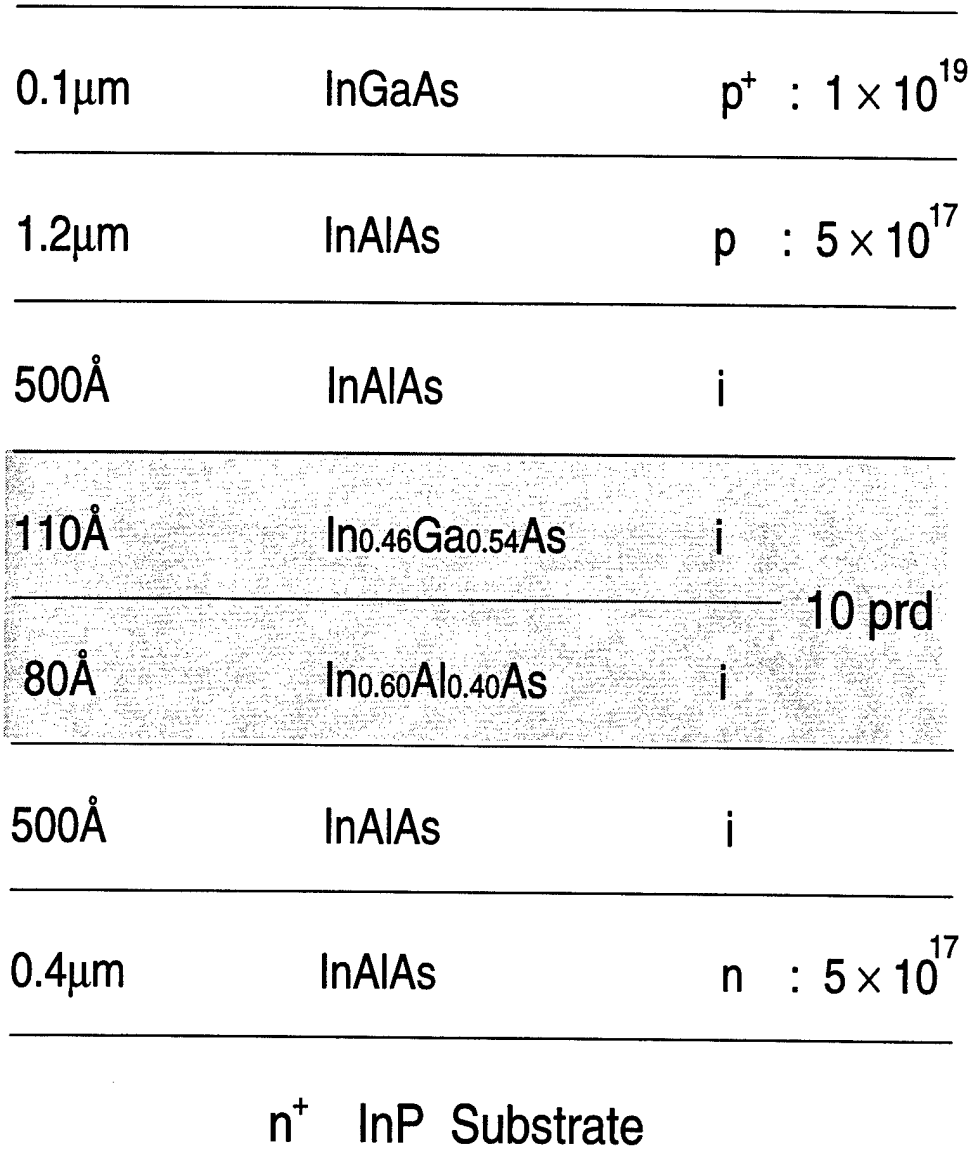

Note: All InGaAs and InAlAs layers are lattice matched to InP except labeled.

Figure 4.1: InAlAs/InGaAs p-i(MQW)-n QCSE electroabsorption modulator heterostructure.

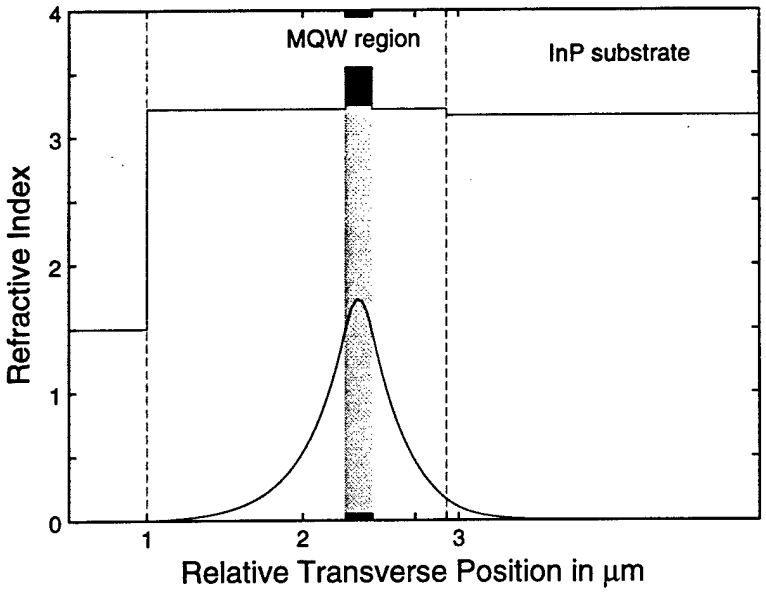

Figure 4.2: Calculated mode profile in the transverse direction.

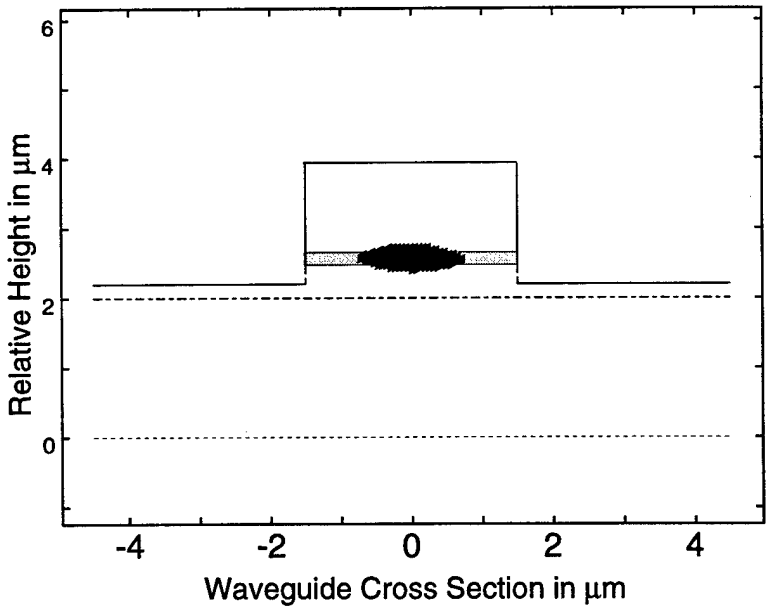

Figure 4.3: The cross section of the designed waveguide along with the calculated mode profile in the waveguide.

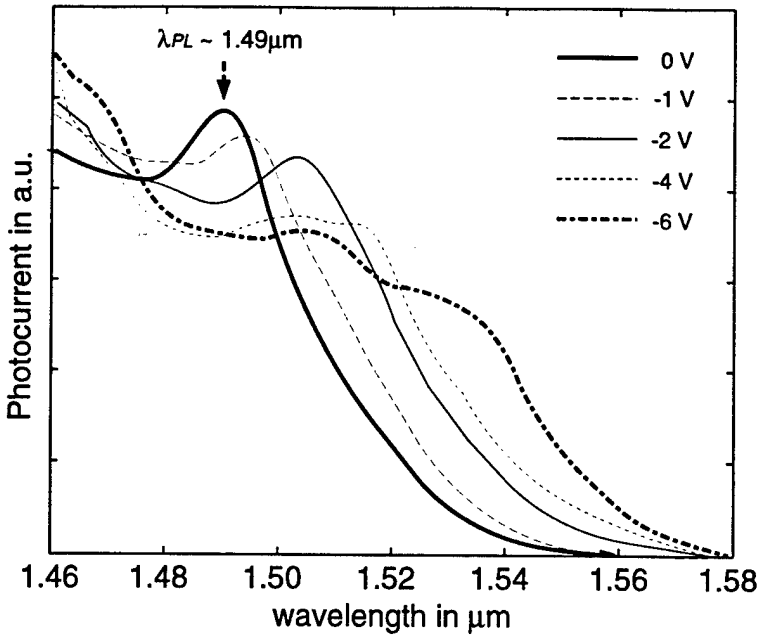

Figure 4.4: Measured InAlAs/InGaAs QCSE electroabsorption modulator photocurrent spectra.

set at 200W). Here note that most of the waveguide structure layers have Al content and the RIE etching gases used are BCl_3 and Ar mixtures. It is expected that Cl_2 instead of BCl_3 will produce similar or even better results. The n contact metal is deposited on the n^+ substrate and then annealed at 400°C for 60 seconds. A thick PECVD SiO_x ($\sim$ 0.8–1μm) is deposited as the passivation. The contact pad metal (Ti/Al/Ti/Au) is finally evaporated on the sample. The deivce is then cleaved into 400μm long for samples testing.

4.4.3 Device Characterization

The photocurrent spectra, shown in Fig.4.4, is measured by YAG pumped color center laser with the wavelength varying from 1.46μm to 1.58μm. The photocurrent peak position at zero-bias is around 1.49μm, which verifies the previous design. As the bias increases, the absorption peaks become broader and shift towards longer wavelength illustrating the Stark effect.

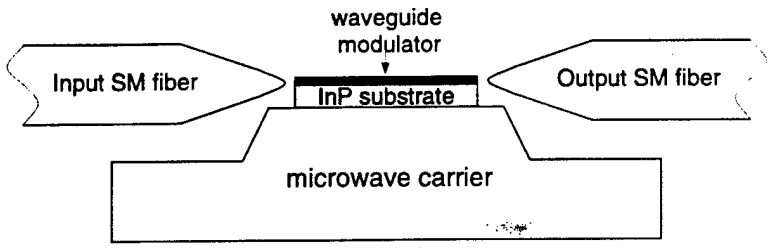

Figure 4.5: Schematic diagram of the fiber-in-fiber-out stage.

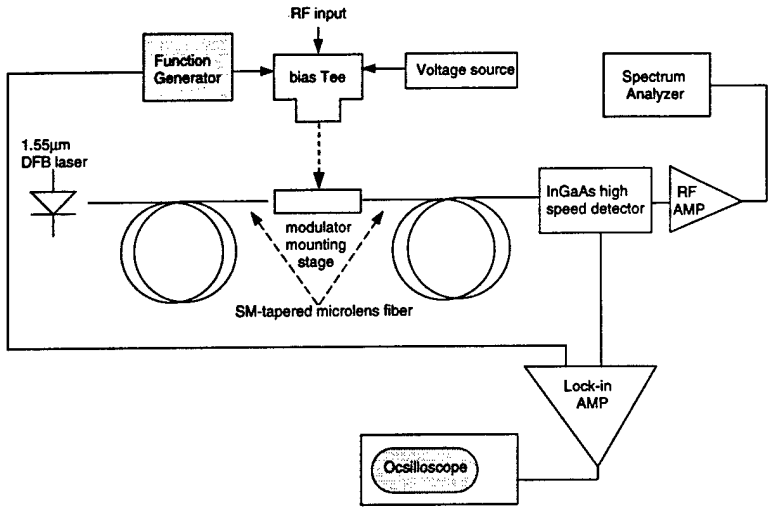

Figure 4.6: Experimental setup for measuring the waveguide modulators.

The device is mounted on a microwave carrier and wired bonded for DC and RF measurement. A fiber-in-fiber-out scheme, schematically shown in Fig.4.5, is adopted in this measurement. The entire experimental measurement setup is illustrated in Fig.4.6. A standard single-mode tapered fiber, see Fig.4.7, is used to couple the light into waveguide as well as out of the waveguide.

Since the waveguide core region is very small (3μm wide and 0.2μm thick), it is very difficult to couple the light into the waveguide. The technique used here is to bias the modulator into forward bias region first. Then to optimize the position of the fiber at input end through spontaneous emission light. This end is then pigtailed to a 1.55μm DFB laser. The fiber at the output end is then aligned through maximizing

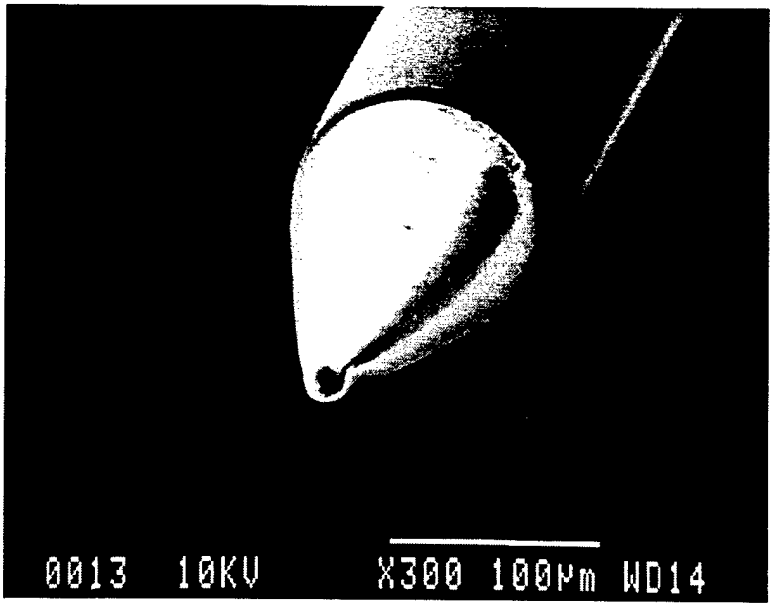

Figure 4.7: Enlarged picture showing the tip of a tapered fiber.

the detector output signal. Here the lock-in amplifier is used to enhance the signal-to-noise (S/N) ratio. A typical measured input modulation signal and modulated output signal are shown in Fig.4.8.

A measured optical transmission characteristics is shown in Fig.4.9. The input optical power is about 2mW and the insertion loss is typically between 13–15dB for an uncoated 400μm long modulator. The result in this measurement indicates that a serious background stray light affects the extinction ratio. This problem could be alleviated by using micropositioners in fiber alignment. A thick non-transparent passivation, such as polyimide film, would also help.

The measured RF modulation bandwidth for a 400μm long device, shown in Fig.4.10, indicated a $f_{-3dB} \sim$ 9GHz. Much higher modulation bandwidth can be obtained if a shorter device is used since the device equivalent capacitance is smaller. Here a 50Ω termination resistor is wire-bonded in parallel and the RF power is set at 5dBm. The equivalent circuit, depicted in Fig.4.11, with the lumped elements

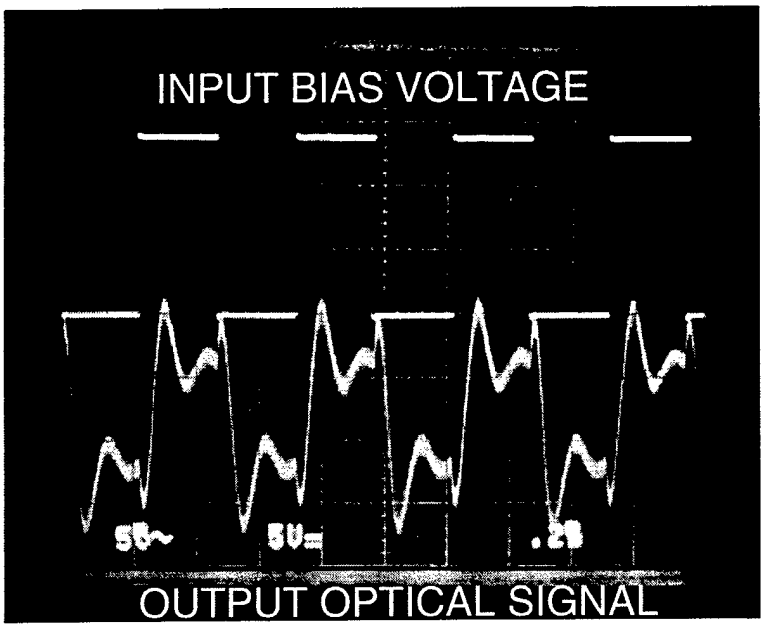

Figure 4.8: A typical measured input modulation signal and modulated output signal.

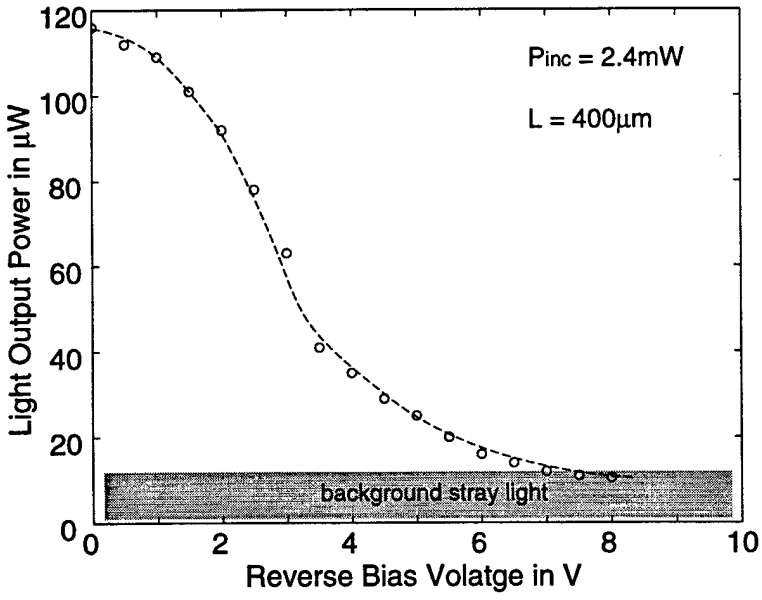

Figure 4.9: Measured optical transmission characteristics for a 400μ long modulator.

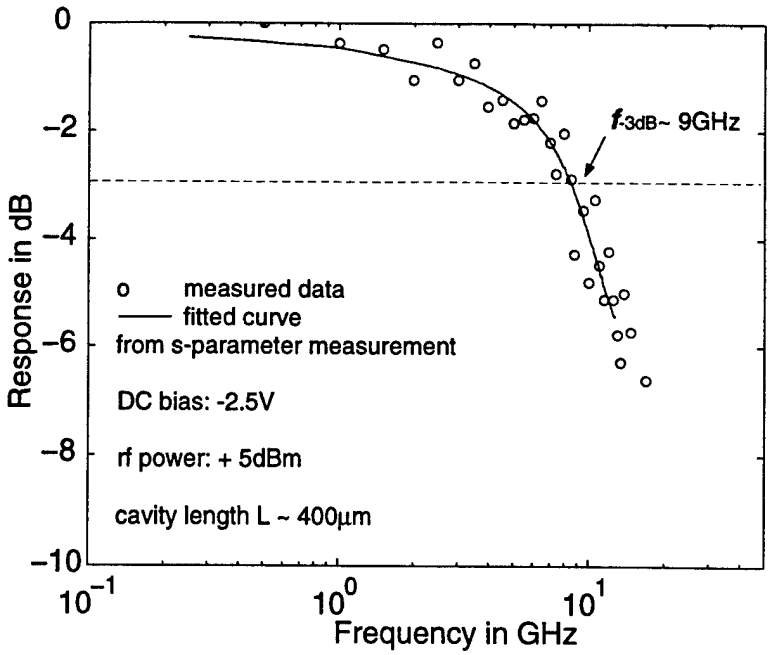

Figure 4.10: Measured small-signal modulation bandwidth for a 400μ long modulator.

extracted from S-parameter measurement indicates that the modulator has an equivalent capacitance around 0.56pF at a reverse bias voltage of 2V. This value gives a modulation bandwidth $f_{-3db} = \frac{1}{\pi RC}$ about 10–11GHz, which is in quite good agreement with the direct measurement. A fitted curve based on S_{11} is also shown in the figure.

4.5 Erbium-Doped QCSE Modulator

As mentioned before, power dissipation is a critical issue in designing electroabsorption modulators, especially in the realization of large area two-dimensional arrays of devices operating with light perpendicular to the device plane. These devices are attractive for potential use in highly-parallel optical interconnects and in spatial-light modulators. Generally, QCSE modulators have to sustain an intrinsic dissipation approximately equal to the absorbed optical power and an additional non-intrinsic

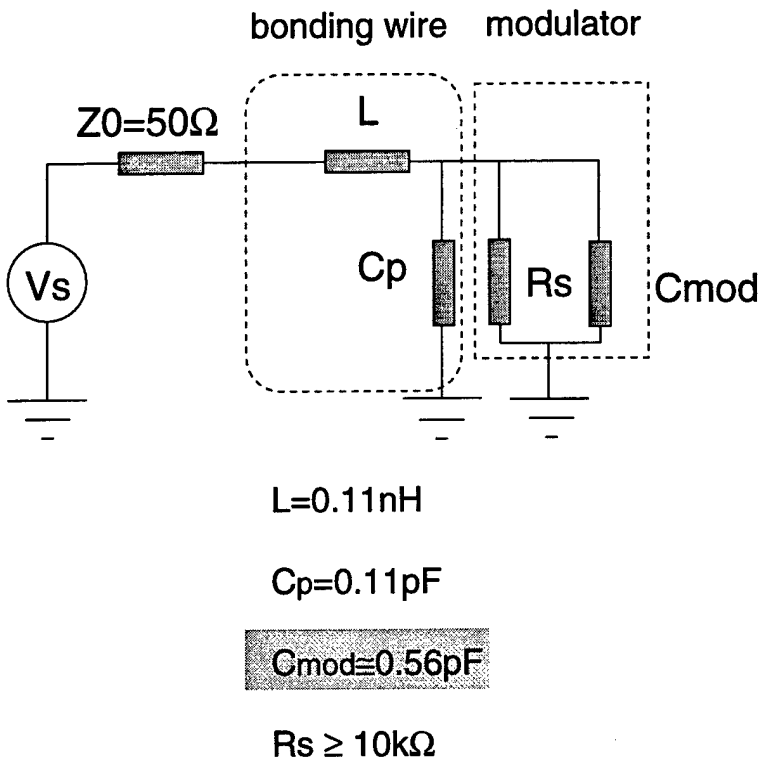

Figure 4.11: Equivalent circuit extracted from the S-parameter measurement of a 400μ long modulator. The DC bias voltage is -2.5V.

power dissipation derived from the addressing electrical (bias) power. The latter, which often dominates the intrinsic dissipation, becomes the chief source of device heating. The high photocurrent collection efficiency in the QCSE modulators, due to the large radiative recombination time ($0.6 - 1\ ns$), causes both intrinsic and non-intrinsic dissipation to derive from the photocurrent [78].

In this section, a novel technique by selectively doping quantum wells with erbium in the well region to reduce the non-intrinsic power dissipation will be described below.

4.5.1 Theory

QCSE MQW modulators are electrically-addressed devices whose operation requires control of the electric field in the intrinsic (MQW) region. Excitons are generated by absorption of near-bandedge photons and subsequently ionize into constituent electrons and holes. The electron and hole may escape from the quantum wells and drift in the electric field of the diode to the contact regions. During the course of this motion, the carriers interact with the lattice, depositing vibrational (thermal) energy there. The potential through which the carrier travel is

$$V = V_{bi} + V_a \tag{4.7}$$

where V_{bi} is the built-in voltage of the diode determined by the band-gap and the doping, and V_a is any externally-supplied potential. In this scenario even the intrinsic dissipation is electrical in nature and due to transport of photogenerated carriers through V_{bi}. The non-intrinsic part is due to the external applied bias V_a. The current (i_{ph}) generated by illumination with optical power (P_{inc}) may be expressed as

$$i_{ph} = P_{inc}\rho \tag{4.8}$$

where the responsivity (ρ) is

$$\rho = A\frac{\eta e}{\hbar\omega} \tag{4.9}$$

$\hbar\omega$ is the photon energy, e is the electronic charge, A=(1-exp(-αL)) is the absorbance of the material assuming an active thickness L with an absorption coefficient α, and η is the internal quantum efficiency, or the number of photogenerated carrier pairs collected per absorbed photon. For η=1, the quantity $\eta e/\hbar\omega$ has a value of 0.686 A/W at 850 nm. To illustrate the relative contributions to dissipation we consider the example of 5 mW of 850 nm light incident on a short-circuit device with V_{bi}=1.45 V and A=0.865 (this value is obtained for a MQW with a typical absorption of α=20,000 cm^{-1} and L=1μm). Thus, the flow of photogenerated carriers will dissipate entire absorbed power of 4.3 mW intrinsically. If a 5 V bias is applied, the total electrical dissipation increases to 20 mW, of which 15 mW is non-intrinsic and extracted from the power supply.

Fast recombination of the photogenerated carriers, of radiative or non-radiative nature, can provide an alternative to the photocurrent dissipation path. This can be understood as the suppression of ρ or η equivalently since the internal quantum efficiency is defined as a function of carrier lifetime. From the definition the shorter the lifetime is, the lower the internal quantum efficiency is. The resulting power dissipation, through photons or phonons, would be entirely non-electrical in nature. Hence, the limit is set by the intrinsic power dissipation due to the absorbed photons. Proton implantation of the quantum well region of QCSE modulators to reduce the carrier lifetime has been investigated [78], with some success. However, lack of control of the implant profile and the broadening and disappearance of the excitonic resonances at high implant doses can present problems. Furthermore, the series resistance of the diode, on the end from which the implantation is done, might

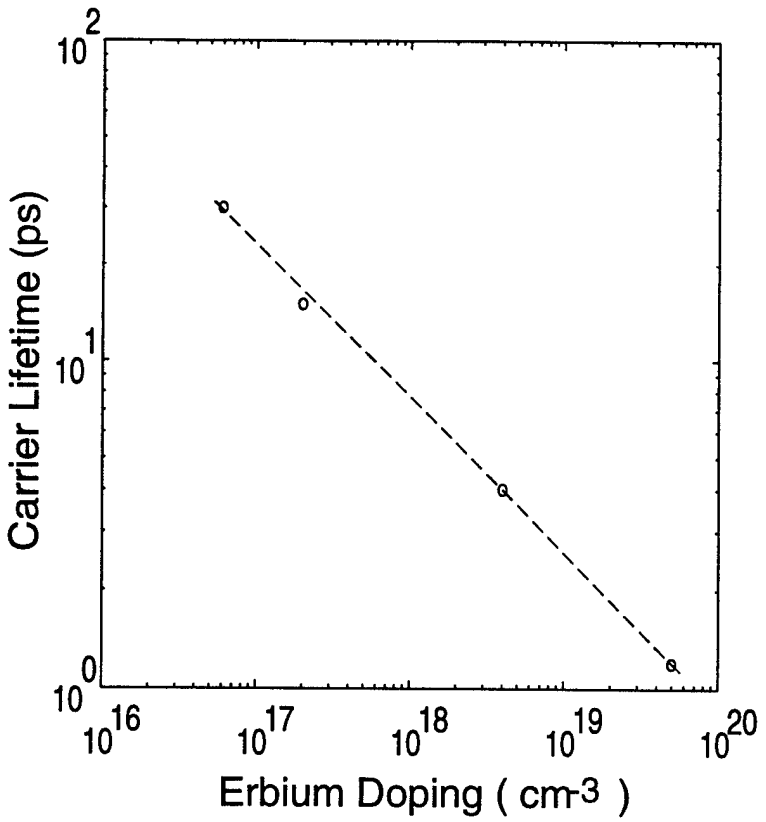

Figure 4.12: Dependence of carrier lifetime on Er doping concentrations. The lifetime was measured by electro-optic sampling.

increase and the high speed modulation properties will be degraded.

Recent studies have demonstrated the controlled and reproducible tuning of the carrier lifetime in GaAs in the range of 1.5 $ps - 50$ ps by co-doping with Er during molecular beam epitaxy [79]. Epitaxial layers of GaAs were doped in the range of 5×10^{16} - 5×10^{19} cm^{-3}, as measured by secondary ion mass spectrometry (SIMS). Electro-optic sampling was used to obtain the carrier lifetimes from the transient photoconductive current induced by a short-pulse laser. The measured data is shown in Fig.4.12. The Er-doped material also exhibits high resistivity [80]. High resolution transmission electron microscopy (TEM) indicates the formation of ErAs precipitates in Er-doped GaAs [80],[81]. We believe that depletion caused

by the formation of ErAs-GaAs Schottky diodes and the presence of midgap states at the ErAs/GaAs interface induced by the ErAs precipitates account for the high resistivity and the ultrashort carrier lifetimes, respectively [80]-[83]. In the present study we have selectively doped the well regions of GaAs/AlGaAs QCSE modulators with Er and have achieved a reduction of two orders of magnitude in the photocurrent responsivity of the devices.

4.5.2 Device Structure and Fabrication

$GaAs/Al_{0.3}Ga_{0.7}As$ p-i(MQW)-n modulators structures, as shown in Fig.4.13, were grown by molecular beam epitaxy and only the 100 Å well regions of 50 period MQW were selectively doped with Er. The Er doping level was varied in the range of 5×10^{17} to 1×10^{19} cm^{-3} in different samples and was confirmed by SIMS measurements. Low temperature (18 K) photoluminescence (PL) measurements indicate that the excitonic emission is present up to a doping of 1×10^{19} cm^{-3}, as shown in Fig.4.14. At room temperature the excitonic emission is preserved up to a doping of 1×10^{18} cm^{-3}. 250 μm diameter mesa-shaped diodes were fabricated by standard photolithographic techniques and wet and dry etching. The n- and p-type contacts were formed by evaporated Ni/Ge/Au/Ti/Au and Ti/Au, respectively. A backside hole was formed by using a combination of non-selective (H_3PO_4 : H_2O_2 : methanol = 1 : 1 : 2) and selective (NH_4OH : H_2O_2 = 1 : 24) etchants.

4.5.3 Experimental Results

To verify that the peak in the photocurrent versus voltage data arises from the excitonic resonance instead of the Fabry-Perot (FP) resonance, an undoped and unthined sample is prepared at the same time. The measured photocurrent-voltage characteristics from an un-thinned sample ($\sim$ 400μm thick) with 5×10^{17} cm^{-3}

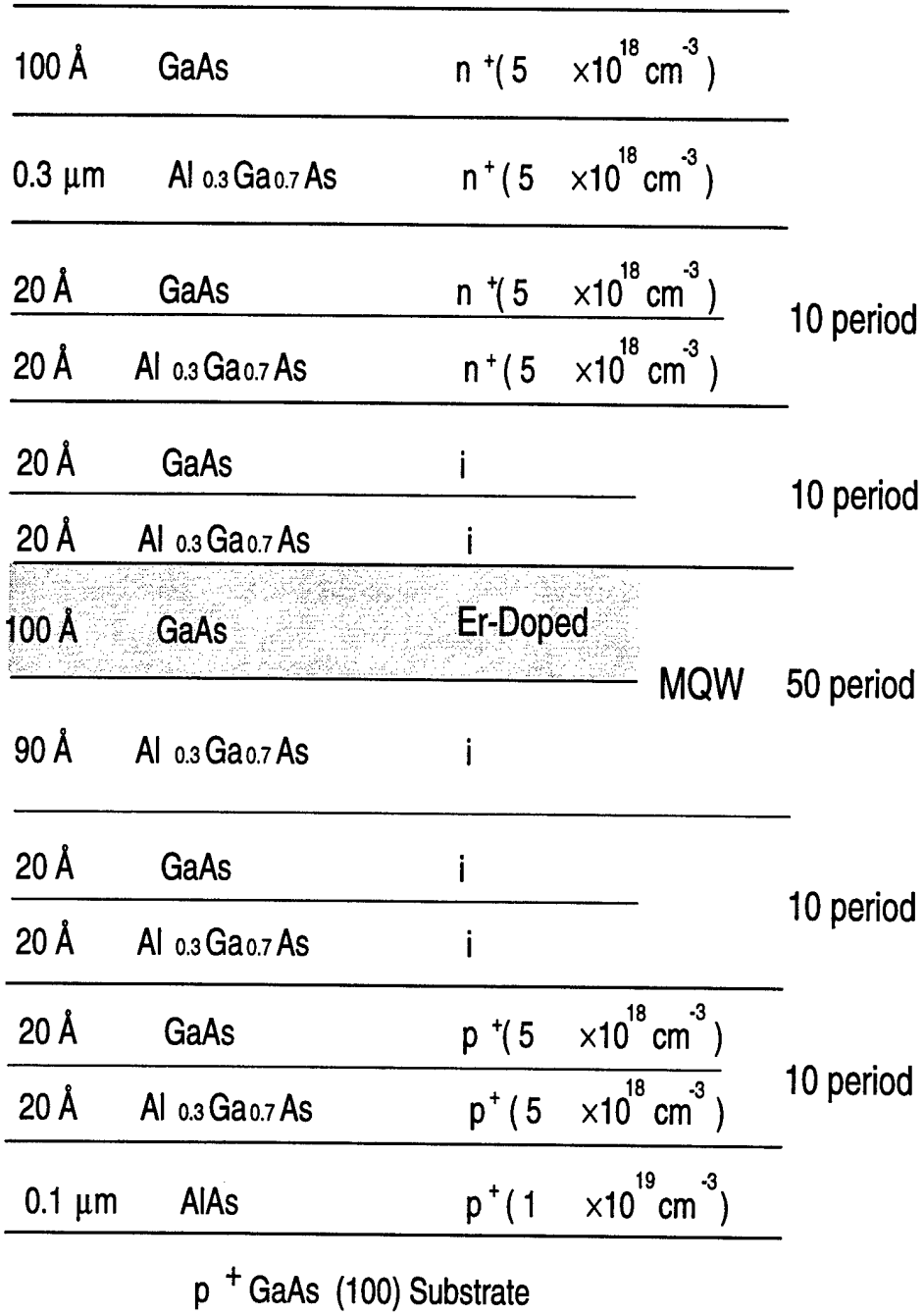

Figure 4.13: Epitaxial layer structure for QCSE modulator grown by MBE. The Er-doping level in the well regions are 5×10^{17}, 1×10^{18}, and 1×10^{19} cm^{-3}.

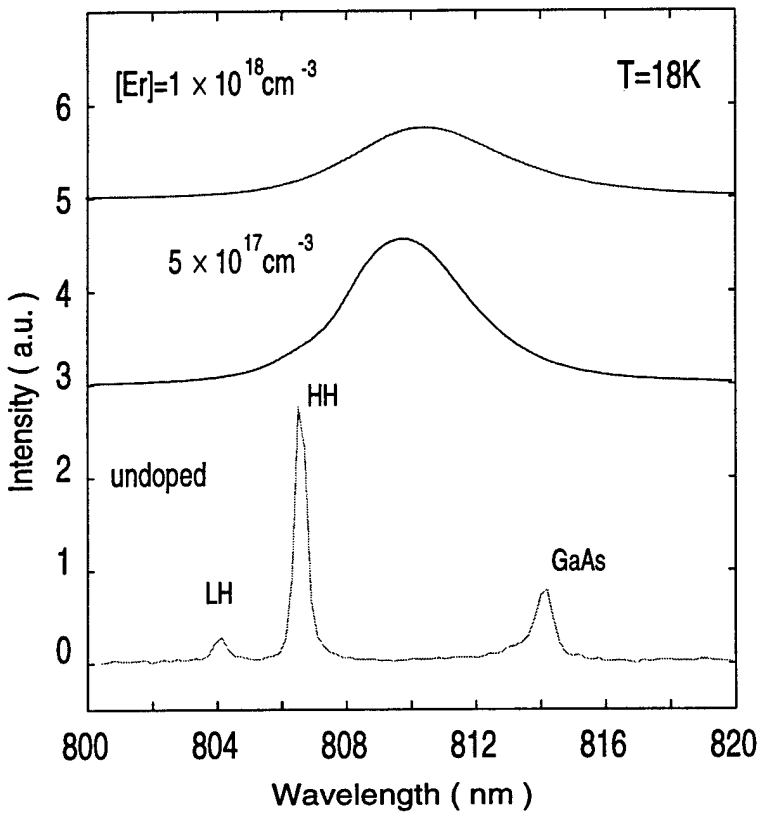

Figure 4.14: Low temperature excitonic spectra for undoped and Er-doped samples.

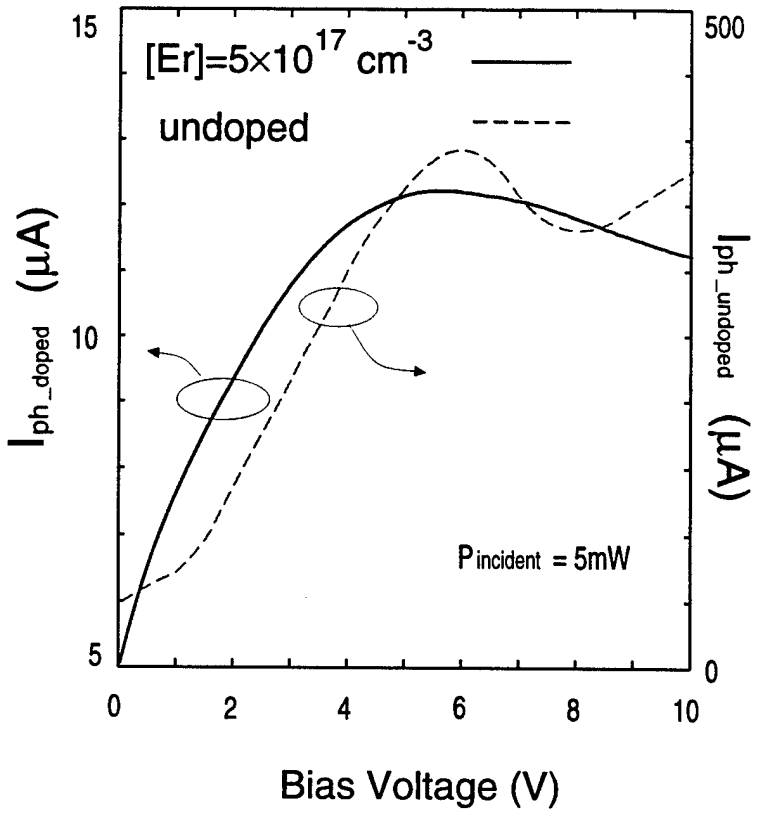

Figure 4.15: Dependence of photocurrent on bias for p-i(MQW)-n diodes with undoped and Er-doped (5×10^{17} cm^{-3}) quantum wells.

Er doping in the wells is compared to an undoped sample in Fig.4.15. A 855 nm GaAs/AlGaAs quantum well laser operated at 5 mW was used as the excitation source, which is approximately 15 nm above the heavy hole (HH) excitonic resonance. The peak due to the HH excitonic transitions is clearly observed in the photocurrent . The excitonic features are preserved even at higher doping levels. Figure 4.16 shows the dependence of photocurrent responsivity on bias for different doping level at λ=855 nm. In the doping range shown in the figure, the measured photocurrent exhibits a decrease of an order of magnitude, from 40 μA to 3.5 μA at a bias of 5 V. Compared to the photocurrent in the undoped sample, the improvement is approximately two orders of magnitude. The photocurrent responsivity for the device with [Er]=1×10^{19} cm^{-3} was measured to be 0.005 A/W, in contrast to 0.3-0.4 A/W

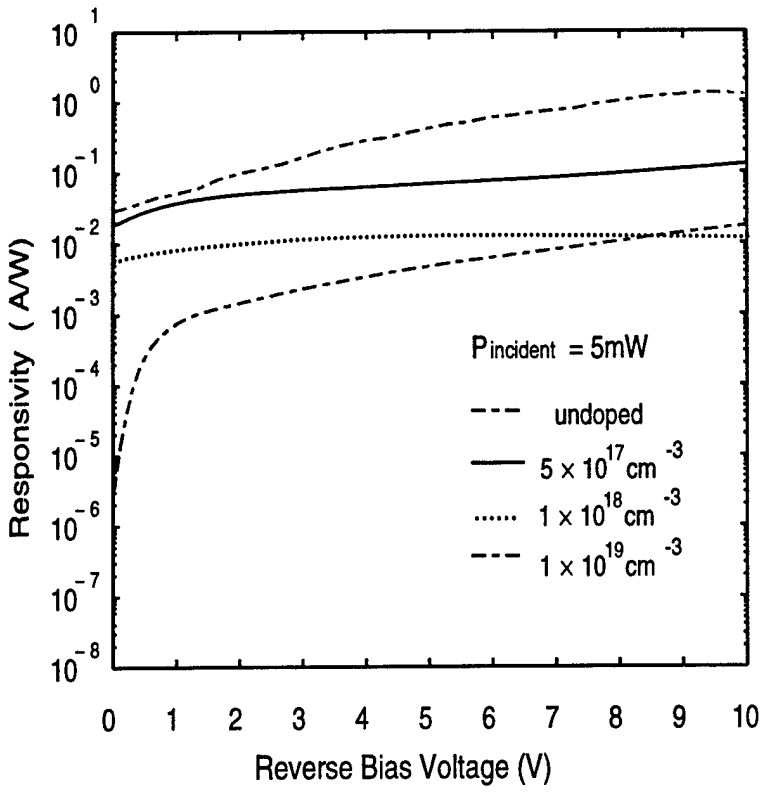

Figure 4.16: Dependence of photocurrent responsivity on bias in QCSE modulators at λ= 855 nm with different Er doping levels in the quantum wells. The incident light power is 5 mW.

in the undoped devices, at a bias of 5 V.

The dc modulation characteristics of the modulators were measured directly by illuminating the light on the top uncoated surface and collecting the transmitted light through the backside hole. A GaAs/GaAlAs laser diode ($\lambda = 884\ nm$) biased at 1 mW was used for photoexcitation. Figure 4.17 shows optical transmission data measured for the undoped device and the doped devices. An extinction ratio greater than 1:8 is obtained from these samples. It is obvious that the doped devices suffer larger absorption loss due to the exciton broadening and the red-shift of the excitonic peak as shown in Fig.14.14. Note that the higher modulation contrast ratios exhibited in the Er-doped devices contrary to expectation, since the exciton resonance

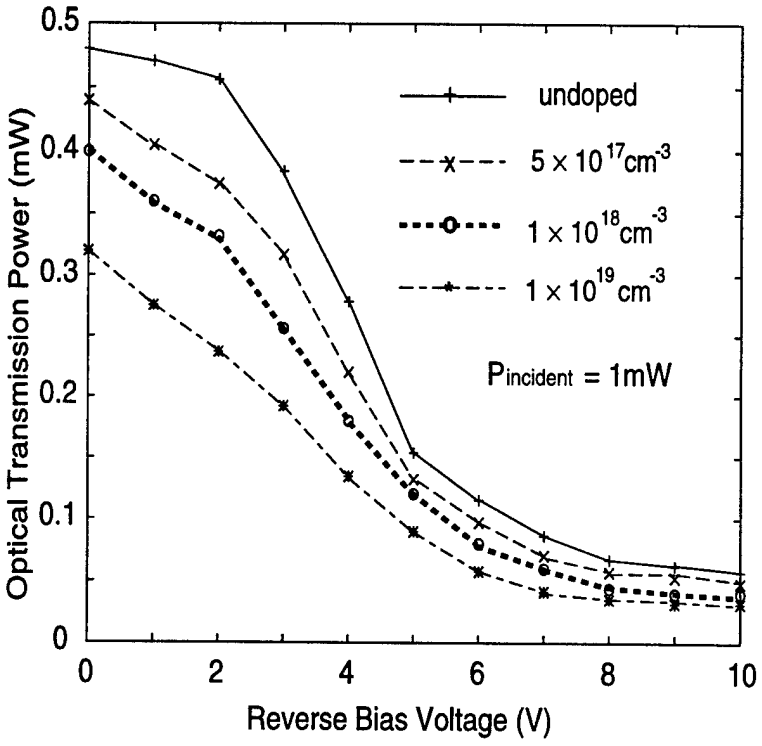

Figure 4.17: Optical transmission characteristics of undoped and Er-doped QCSE modulator for different Er doping levels in the quantum wells.

is broadened. It is believed that there may be some Fabry-Perot (FP) resonances existing in these transmission samples which apparently enhance the contrast ratios.

4.5.4 Discussion

The preliminary results presented here are by no means ideal, but indicate a simple and new technique of reducing carrier lifetimes and photocurrent dissipation in QCSE modulators. The doping is selectively done in the well regions during epitaxy and will therefore not degrade the external parasitics of high-speed devices. The doping parameters need to be optimized so that the optimum carrier lifetime is obtained. The latter involves a balance between responsivity and modulation index, determined by the exciton resonances. This work is in progress.

4.6 Summary

An InAlAs/InGaAs, with 0.5% strain-compensated MQW, waveguide modulator has been designed, fabricated, and characterized. The measured photocurrent spectra verifies the original design and the optical transmission characteristics demonstrate a good optical modulation. Further improvement in extinction ratio can be achieved by modifying the device fabrication and measurement techniques. The modulation bandwidth matches well with the extracted modulator equivalent circuit. Higher modulation bandwidth can be expected from a shorter device. However, it is very difficult to cleave or handle a very short device ($\sim 100\mu$m) in reality. Etching a facet or integrating the active device with another passive waveguide might be an effective approach to solve this problem. Also, developing new technologies to bias and package the device become a very crucial challenge in the near future, especially as the modulation bandwidth reaches beyond 20GHz. Wire-bonding suffers a serious inductance problem and loss and is not suitable in the high frequency applications.

A new scheme of reducing the photocurrent of a quantum confined Stark effect multiple quantum well modulator is demonstrated. The GaAs well regions of the 50 period $GaAs/Al_{0.3}Ga_{0.7}As$ multiple quantum well are selectively doped with Er during molecular beam epitaxy to reduce the carrier lifetime to the order of picoseconds. 250 μm diameter mesa-shaped devices have been characterized. The photocurrent responsivity is as low as 0.005 A/W and an extinction ratio greater than 1:8 is achieved at a bias voltage of 8 V.

CHAPTER V

COUPLED-CAVITY INTEGRATED LASER/MODULATOR

5.1 Introduction

Optoelectronic integrated circuits (OEIC) have been drawing a great deal of attention recently because of compactness, low loss, and low cost. Integrated transmitters are very promising sources for long-haul and high-speed optical communication links at 1.5 μm. Monolithically integrated coupled-cavity transmitter (laser/modulator) have advantages over other types of integrated transmitters because it can be achieved in one-step epitaxy. In addition, several specific properties such as longitudinal-mode selectivity and optical bistability can be realized by choosing appropriate bias points for different waveguides [84]–[86].

In this chapter, the study of a coupled cavity laser/active waveguide [87]–[89] fabricated with the *same* InP-based heterostructure grown by one-step epitaxy is described. This is the first step to successful laser-modulator integration. The active waveguide can operate as an electroabsorption modulator, or amplifier. This approach makes use of dry reactive ion etching (RIE) to achieve electrical isolation between these two waveguides as well as to form the high quality laser mirrors for feedback and coupling between the two devices. This study represents the first

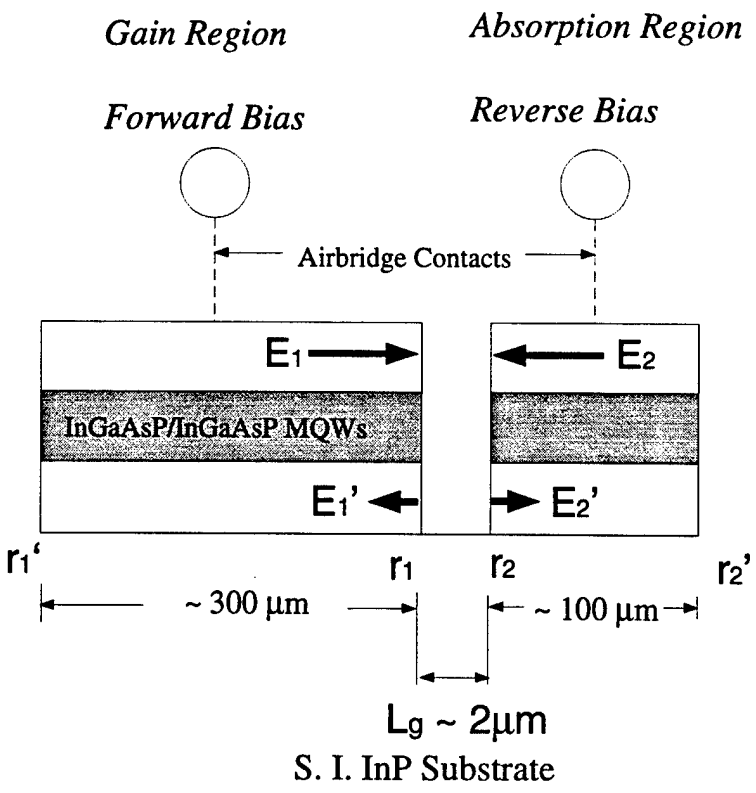

Figure 5.1: Device schematic.

investigation of such coupled-cavity systems.

5.2 Determining the Coupling Coefficient

The schematic of this coupled cavity laser/active waveguide studied here is shown in Fig.5.1. Two waveguides are aligned by optical lithography and separated by an air gap. Contrary to the single-cavity laser for which the facet reflectivity (loss) is wavelength-independent, in a coupled-cavity laser the effective facet reflectivity becomes different for different Fabry-Perot (FP) modes, i.e., it depends on the air gap distance. Hence, it is important to determine the coupling coefficient in this structure first. Two methods were considered in this work.

5.2.1 Scattering-matrix approach

Referring to Fig.5.1 [90]–[92] and using the same notation, the electric fields in the coupled cavity are related by:

$$\begin{pmatrix} E_1' \\ E_2' \end{pmatrix} = \begin{pmatrix} S_{11}S_{12} \\ S_{21}S_{22} \end{pmatrix} \begin{pmatrix} E_1 \\ E_2 \end{pmatrix} \tag{5.1}$$

Here

$$S_{11} = r_1 - \frac{r_2(1-r_1^2)t_g}{1-r_1r_2t_g} \tag{5.2}$$

$$S_{22} = r_2 - \frac{r_1(1-r_2^2)t_g}{1-r_1r_2t_g} \tag{5.3}$$

$$S_{12} = S_{21} = \frac{[t_g(1-r_1^2)(1-r_2^2)]^{1/2}}{1-r_1r_2t_g} \tag{5.4}$$

where t_g, which accounts for the phase shift and the loss experienced by the optical field during a round trip in the air gap, is given by

$$t_g = exp(2ik_0L_g)exp(-\alpha_gL_g) \tag{5.5}$$

Here $r_{1,2}$ are the reflectivities of the electric field at the single etched facet, k_0 is the wave number in the air gap, L_g is the air gap length, and α_g is the loss in the air gap. In this equation, we assume that there is no reflected wave from the other end of the coupled waveguide. In addition, we can assume there is no loss in the air gap, i.e., α_g=0. Assuming $r_{1,2} \simeq 0.3$ and from the dependence of S_{11} on L_g, we can choose $L_g \sim 2\mu$m to give a good S_{11} in considering the device fabrication feasibility.

5.2.2 Finite-difference time domain (FDTD) approach

Finite difference numerical techniques are well known and well established in the microwave domain [93] and, more recently, in the optical domain [94],[95]. Since finite difference techniques are simple to implement and can be coded efficiently, they are

suitable for waveguide structure designs and device performance evaluations. The detailed modeling has been done by R. Jambunathan and J. Singh [96], and is not described here. A wave with the mode profile shown in Fig.5.2(a) is launched in the laser section of the integrated structure, which is assumed to have the slab waveguide configuration. The optical mode profile is obtained by solving slowly-varying time dependent Maxwell equation.

$$\frac{\partial}{\partial t}\mathcal{E}_y(x,z,t) = \frac{i\omega_0}{2}\Big[\mathcal{E}_y(x,z,t) + \frac{1}{\omega_0^2\mu_0\epsilon_0 n^2(x,z)}\Big(\frac{\partial^2}{\partial x^2} + \frac{\partial^2}{\partial z^2}\Big)\mathcal{E}_y(x,z,t)\Big]. \qquad (5.6)$$

As time evolves, the wave first impinges upon the first etched facet where some of the energy is reflected and the rest transmitted into the air gap. From the transmitted energy, a part is reflected at the second etched surface and the remainder propagates within the second guide. It is assumed that the scattering loss is small as long as the etched surface is smooth and vertical. Furthermore, since the distance between the two guides is very small ($\sim$2 μm), most of the power is non-divergent. The summation of the incident and reflected waves from the two facets is shown in Fig.5.2(b). After sufficient time has elapsed we can clearly see the final reflected wave in the first guide as shown in Fig.5.2(c). From the simulation, the effective reflectivity obtained is 0.56.

5.3 Device Design

5.3.1 Layer Structure

The laser heterostructure is grown by metal-organic vapor phase epitaxy (MOVPE) on a semi-insulating InP substrate. The active region consisting of 8 undoped strain-compensated quantum wells [80 Å InGaAsP (with a strain of +0.38 %, λ_g=1.63 μm) wells and 100 Å InGaAsP (with a strain of –0.3 %, λ_g=1.20 μm) barriers] is sandwiched by 500 Å undoped InGaAsP (λ_g=1.20 μm) inner cladding layers and 1.1 μm

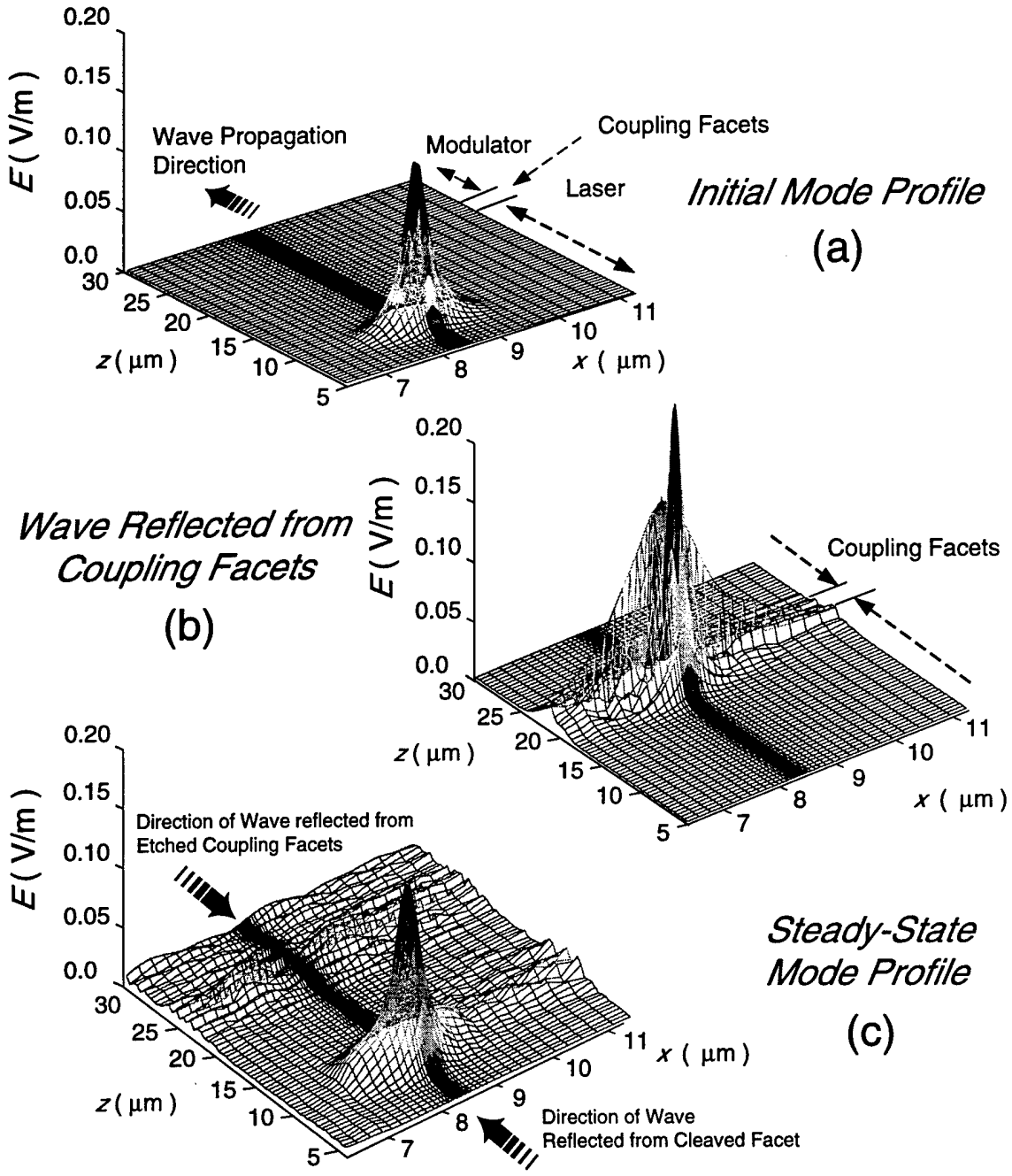

Figure 5.2: Wavepacket propagation in the ridge waveguide laser cavity: (a)initial mode profile excited in the laser cavity; (b) mode profile of wave reflected from the coupling facets; (c) steady-state mode profile of light wave propagation in the laser cavity after reflection (from R. Jambunathan with permission).

0.1 μm	$In_{0.53}Ga_{0.47}As$	p^+ ($3\times10^{19}cm^{-3}$)
0.1 μm	InGaAsP	p ($2\times10^{18}cm^{-3}$)
0.9 μm	InP	p ($2\times10^{18}cm^{-3}$)
0.2 μm	InP	p ($2\times10^{17}cm^{-3}$)
500 Å	InGaAsP (λ=1.2 μm)	i
8 Period MQW's	InGaAsP Well, (L_w=80 Å, λ_{PL}=1.54 μm,	i ε=+0.38%)
	InGaAsP Barrier, (L_b=100 Å, λ_g=1.2 μm,	i ε=-0.303%)
500 Å	InGaAsP (λ=1.2 μm)	i
1.1 μm	InP	n ($5\times10^{17}cm^{-3}$)
0.1 μm	InGaAsP	n ($5\times10^{17}cm^{-3}$)
0.2 μm	$In_{0.53}Ga_{0.47}As$	n^+ ($5\times10^{18}cm^{-3}$)
	S. I. InP (100) Substrate	

Figure 5.3: Epitaxial layer structure grown by MOVPE.

InP (p-doped and n-doped) outer cladding layers on both sides. The top and bottom contact layers are formed with highly doped InGaAs layers. The multiple quantum well (MQW) is designed for emission at 1.54 μm. Fig.5.3 shows a schematic of the heterostructure.

Here the strain-compensated structure was adapted because by introducing some strain in the quantum well regions, the reduction of the effective mass for the top heavy-hole subband leads to reduce the density of state and, therefore, lowers the

threshold carrier density as well as increase the differential gain. The relations can be derived from

$$g_{max} \propto \frac{m_c m_v}{m_c + m_v} \tag{5.7}$$

$$\frac{dg}{dN} \propto \frac{\sqrt{m_c m_v}}{m_c + m_v} \tag{5.8}$$

here g_{max} is the modal gain and $\frac{dg}{dN}$ is the differential gain. m_c and m_v are the electron and hole effective mass, respectively [?]. Besides, the quasi-net zero strain in the whole active region improves materials quality without generating misfit dislocations.

5.3.2 Electronic Properties and Absorption Spectra

The absorption for an individual well in a MQW laser can be obtained by first calculating the bandstructure using a 4×4 $\mathbf{k} \cdot \mathbf{p}$ Hamiltonian [98] to describe the confined valence band states; the conduction band is described using the parabolic approximation with an electron of effective mass m^*[99],[100]. The effect of strain due to lattice mismatch is included [100]. We also assume uniform charge injection into the MQW system. The Fermi Golden Rule is then applied and for an individual well the subband-to-subband optical absorption and spontaneous emission rates were obtained [101]:

$$\alpha_{nm}(E) = -\frac{4\pi^2 e^2 \hbar}{n_0 c m_0^2 W E} \frac{1}{(2\pi)^2} \int d\mathbf{k} \sum_{\sigma} |\hat{\epsilon} \times \mathbf{P}^{\sigma}_{nm}(\mathbf{k})|^2 \times \delta(E^e_n(\mathbf{k}) - E^h_m(\mathbf{k}) - E), \tag{5.9}$$

where $\alpha_{nm}(E)$ is the optical absorption at photon energy E in the well from the n^{th} electron subband and m^{th} hole subband, e is the electron charge, n_0 is the refractive index of the active region, c is the vacuum speed of light, m_0 is the free electron mass, W is the active region width, $\hat{\epsilon}$ is the polarization of the light, and $\mathbf{P}^{\sigma}_{nm}$ is the optical matrix element coupling electrons and holes in the n^{th} and m^{th} subbands with momentum $\mathbf{k}$ and energies $E^e_n(\mathbf{k})$ and $E^h_m(\mathbf{k})$, respectively.

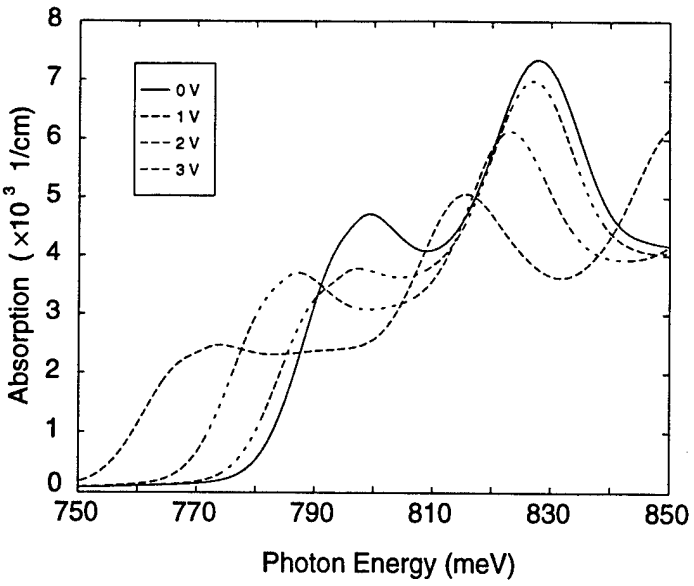

Figure 5.4: Calculated quantum well absorption spectra under different bias conditions (from R. Jambunathan with permission).

To get the total absorption, α, we sum over all subbands n, m and convolve with a Lorentz broadening function, $\Delta(E)$, to account for collision broadening due to carrier-phonon, carrier-carrier, and carrier-alloy scattering. The result is

$$\alpha(E) = \int dE' \sum_{nm} \alpha_{nm}(E')\Delta(E - E'). \tag{5.10}$$

In these lasers the quantum well width is less than 2 orders of magnitude smaller than the lasing wavelength. Since the light experiences absorption only in the well regions, we characterize the laser optical absorption by an optical confinement factor per well, Γ. This excitonic absorption spectra of the MQW was calculated by my co-worker R. Jambunathan and the calculated results are reprinted in Fig.5.4.

5.4 Device Fabrication

The integrated device is fabricated as follows: a 3 μm wide Pt/Ti/Pt/Au layer is first evaporated for p-contact formation. Since the mirror and coupling facet formation by RIE is a critical step for the ultimate success of this integration scheme,

it is described in the following in some detail. A 6000 Å SiO_2 film is formed over the wafer by plasma enhanced chemical vapor deposition (PECVD) and then patterned by RIE (using CHF_3/CF_4=1:1). In order to simultaneously achieve good isolation between the laser and the modulator and a high reflectivity mirror for the laser feedback, a vertical and smooth wall is required. The InP-based heterostructure is etched with a $Ar/CH_4/H_2$ mixture. The etch depth is approximately 3.5 μm, down to the semi-insulating substrate to ensure an electrical isolation between the two devices. The gap between the laser and modulator is 2 μm. To reduce the undercut introduced from the fast reaction of CH_4 with In, the concentration of CH_4 should be low and that of Ar should be high. Optimum results were achieved with a $4CH_4$: $56H_2$:$8Ar$ mixture under conditions of low pressure (10mTorr), high RF power (180W) and a highly depleted CH_4 environment. These conditions ensured nearly vertical walls and good isolation between the two sections. A scanning electron micrograph image of the etched mirror is shown in Fig.5.5. A 6000 Å thick high pressure PECVD conformal SiO_2 layer is next deposited to protect the facets from damage during the subsequent etching steps. Subsequently, the ridge waveguide is formed by the combination of RIE and wet chemical etching. A mesa, down to the bottom contact layer is formed by wet chemical etching and this is followed by evaporation of Ni/Ge/Au/Ti/Au as the n-contact metal. The ohmic contact is formed by annealing at $\sim$ 400°C. Finally, a 3 μm thick Au film is electroplated on a Ti/Au/Ti airbridge pillar for interconnection. Fig.5.6 is a micrograph showing the airbridge connected to the ridge waveguide. Here the reason to use airbridge contact pad is to reduce the parasitic capacitance. The fabricated device is shown in Fig.5.7 and the overall process flow is illustrated in Fig.5.8. The wafer is then cleaved to 400 μm lengths having a laser 300 μm long and the active waveguide $\sim$ 100 μm long.

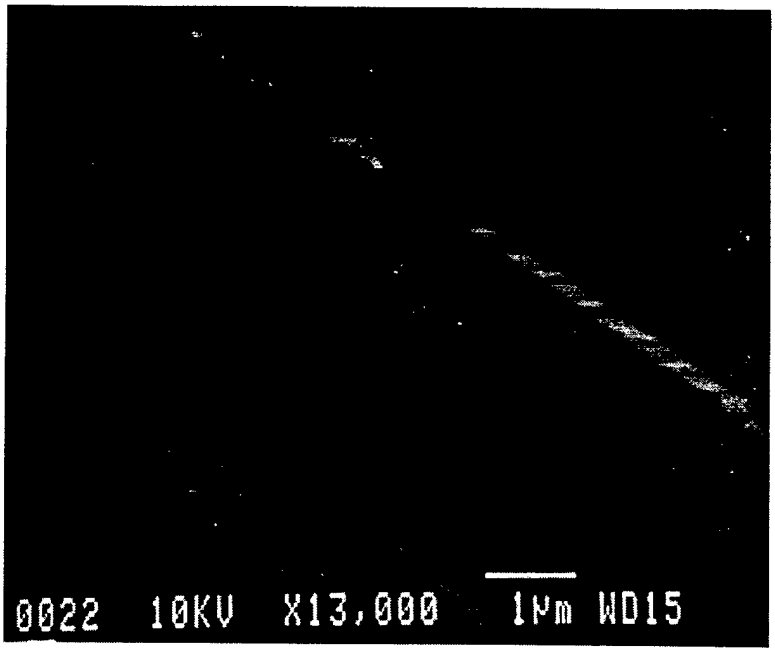

Figure 5.5: Scanning electron micrograph of RIE etched facet.

5.5 Evaluation of the Etched Facets

5.5.1 Deriving Effective Reflectivity

The effective reflectivity of the coupling region is a function of the air gap distance, and moves from maximum to minimum as the gap distance changes by a quarter-wavelength. Based on the modeling study presented previously we plot reflectivity versus gap distance in Fig.5.9. Fine variation in the gap distance is generally not controllable by optical lithography and RIE etching processes. From SEM examinations, we measure a range for the gap size d_g as $d_1 < d_g < d_2$, where d_1=2.05μm and d_2=2.15μm. The effective reflectivity for this range in gap distance is found to be between 0.45 and 0.55, and is represented as the dashed portion of the effective reflectivity curve in Fig.5.9.

To measure the reflectivity of the etched mirrors from experimental data, the

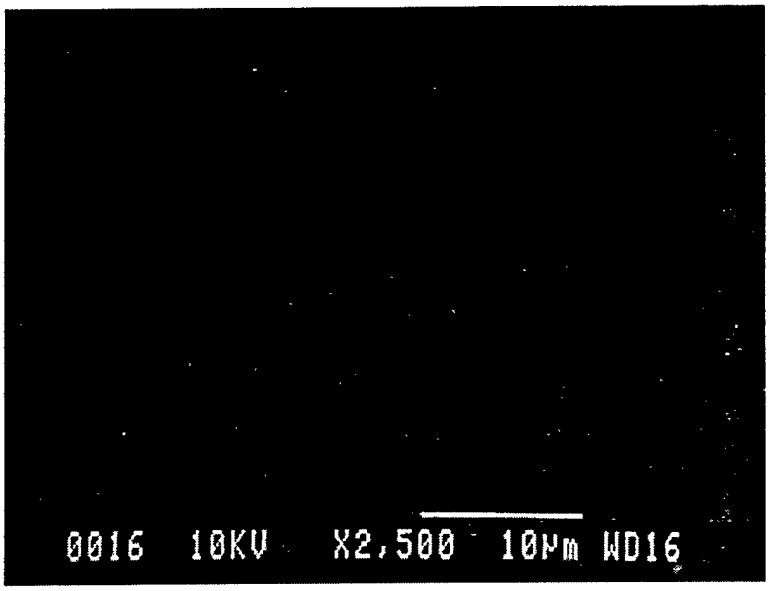

Figure 5.6: Scanning electron micrograph of airbridge contacted to the waveguide ridge.

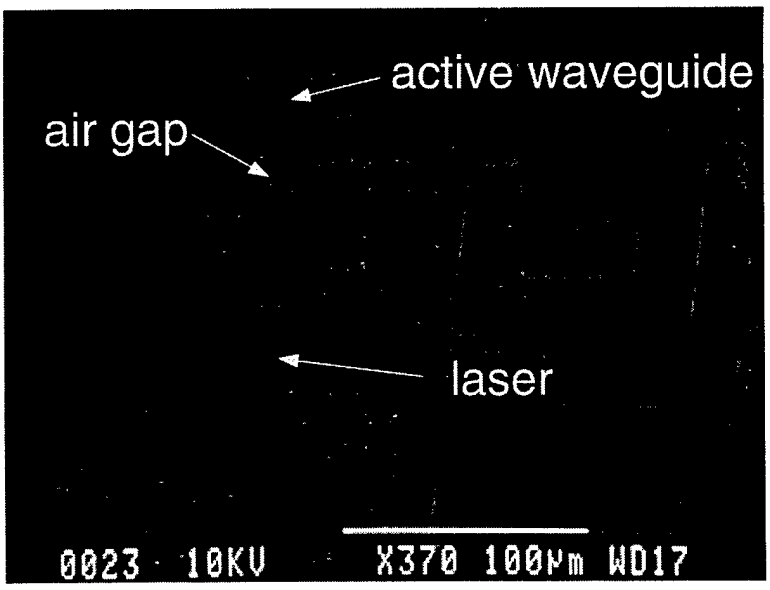

Figure 5.7: Scanning electron micrograph of fabricated device overview.

1. p-contact metal & PECVD SiOx
(6000Å) for RIE etch mask

2. RIE etch coupling facets
(CH4 : Ar : H2 = 8: 4: 56, 10mT, 180W)

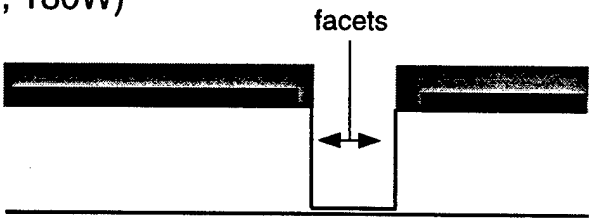

3. PECVD SiOx deposition
(250mT) to protect facets

4. Ridge waveguide formation by RIE and wet etch

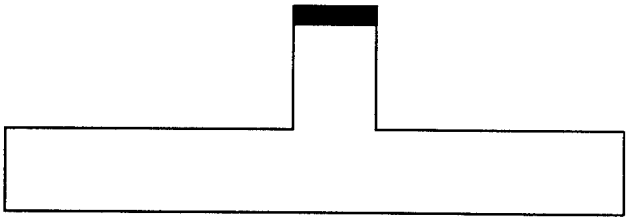

5. n-contact formation by wet etch

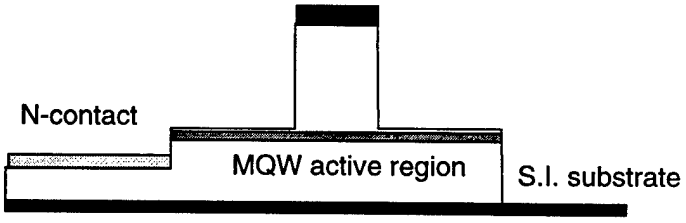

6. Pillar and airbridge for contact pads

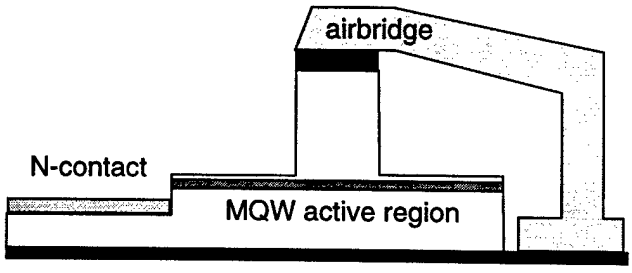

Figure 5.8: Device process procedures.

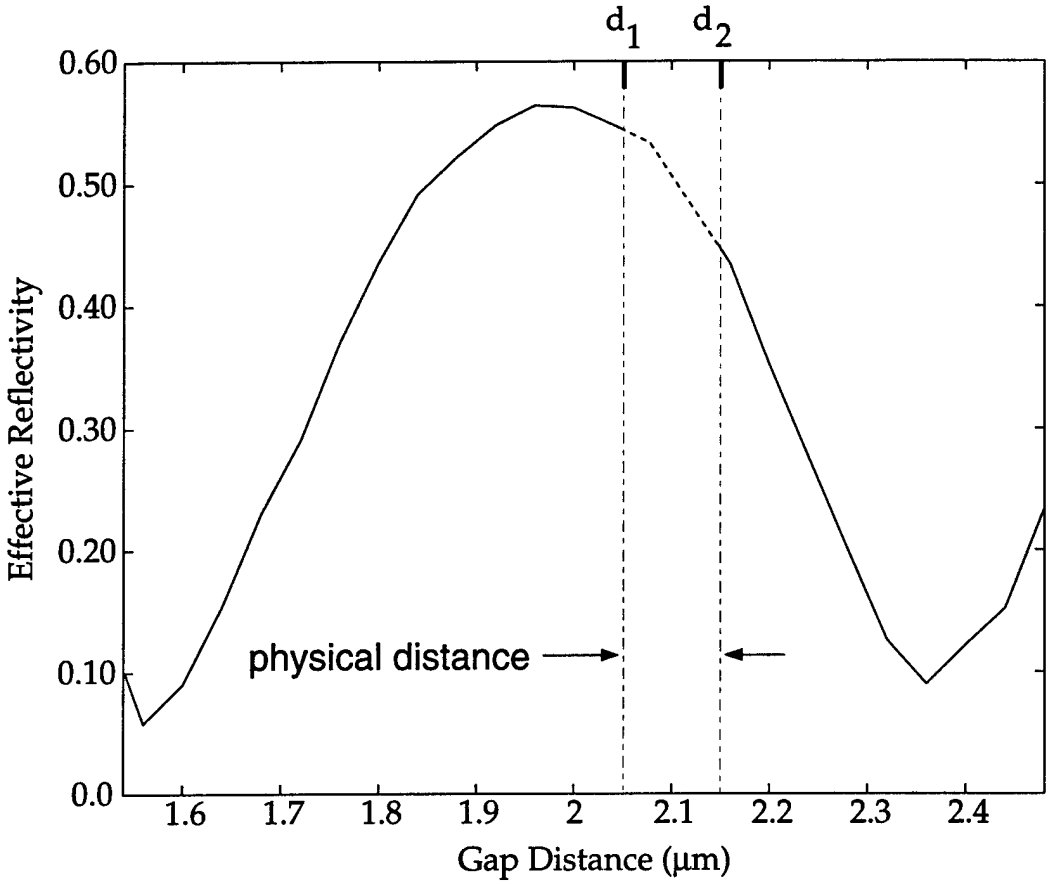

Figure 5.9: Calculated effective reflectivity versus gap distance. The effective reflectivity for the fabricated gap distance is between d_1 and d_2 and is represented by the dashed portion of the curve (from R. Jambunathan with permission).

logarithmic dependence of the laser gain on the threshold current density is utilized [102],[103]. Accordingly,

$$J_{th} = \frac{J_0}{\eta_{in}} exp\{\frac{1}{\Gamma\beta J_0}[\alpha_{in} + \frac{1}{2l} ln(\frac{1}{R_{cleave} R_{etch}})]\} \tag{5.11}$$

where J_0 is the transparency current density, η_{in} is the internal quantum efficiency, α_{in} is the cavity loss, Γ is the confinement factor, β is the gain coefficient near the transparency current density, l is laser cavity length, R_{cleave} is 0.32, and R_{etch} is the effective reflectivity of the etched and coupled facets. Fig.5.10 shows a threshold current density versus inverse cavity length measured for a ridge waveguide lasers with both cleaved facets and one cleaved and one etched facet in the integrated structure. From the slope of the latter dependence, the effective reflectivity is estimated to be in the range 0.5 – 0.55, which is very close to the value obtained from the simulation described above. It is found that there is a range of cavity lengths, which is around 200-250 μm, that can give a smaller threshold current density due to this reflectivity improvement. The reflectivity of a single etched facet can be derived from the method mentioned in previous section and is governed by

$$R_{etch} = r - \frac{r(1 - r^2)t_g}{1 - r^2 t_g} \tag{5.12}$$

Here R_{etch}=0.5 is the value we obtain from the measurements and simulation of the coupled structure. By substitution of the appropriate values of these parameters we in the equations, we calculate the optical power reflectivity of the etched facet, $R_{etched-facet} = r^2 \simeq 0.3$. This value is very close to the value of 0.32 measured for a cleaved facet and is further evidence of the high degree of perfection achieved during RIE.

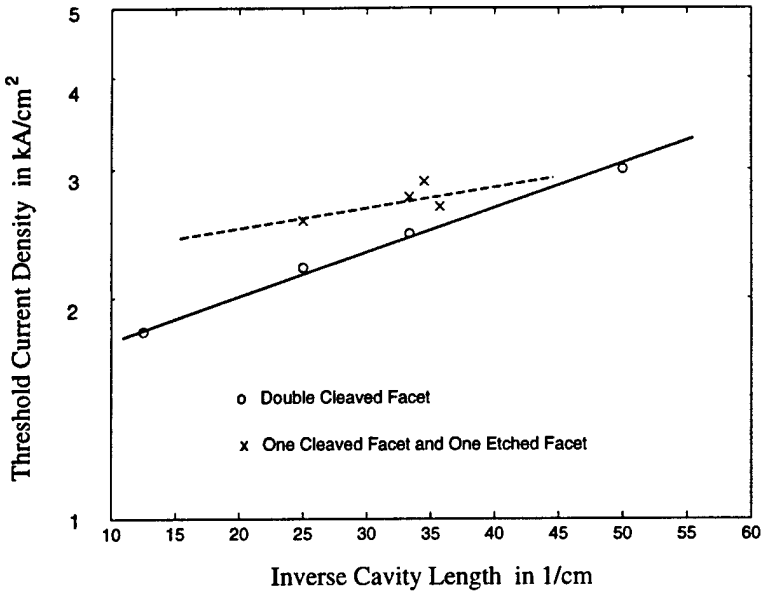

Figure 5.10: Measured threshold current density versus inverse cavity length.

5.6 Evaluation of Surface Damage

We investigate the possibility of surface damage caused by RIE, by fitting the parameters in Eq.5.11 with the experimental data. The data reveals that the cavity loss is $\sim 40\text{cm}^{-1}$ for both the double cleaved facet laser and the one RIE-etched facet and one cleaved facet laser. This implies that RIE did not significantly degrade the device performance. Therefore, we believe the high internal cavity loss measured is primarily due to the material quality instead of degradation introduced in the processing.

5.7 DC Characteristics of Coupled Devices

Figure 5.11 depicts the measured light versus current (L-I) characteristics of a 300 μm long laser diode coupled to the waveguide with the light exiting from the cleaved facet of the laser. The laser has a threshold current of 24 mA and a slope efficiency of 0.22 mW/mA per uncoated facet, which is a bit low because of the wide

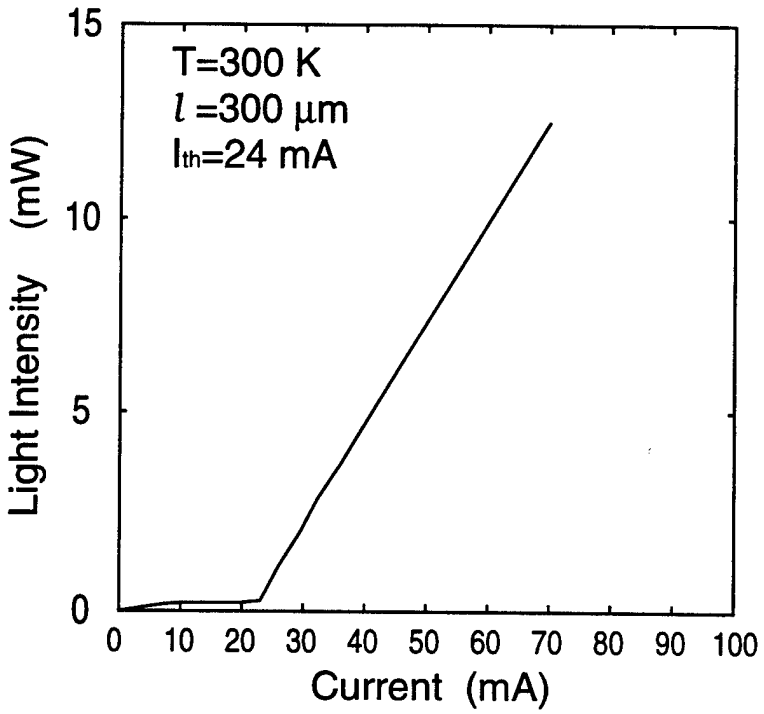

Figure 5.11: Measured L-I characteristics of a 300 μm long integrated laser with cleaved and etched facets.

wells used in the gain region. The extinction, or modulation, characteristics of a coupled waveguide 120 μm long are shown in Fig.5.12. The output power corresponds to light exiting from the cleaved facet of the modulator. The integrated laser is biased with a drive current of 40 mA. An extinction ratio (8 dB) is obtained for a bias swing of 4 V. In most integrated laser-modulator structures [105]–[109], the modulator is biased under reverse bias conditions. In our case, we use a modulating range that takes the diode to forward bias conditions as well as reverse bias conditions. The reason for the modulating voltage swing to positive values is obvious upon calculation of the quantum well absorption characteristics, shown in Fig.5.4. The absorption at room temperature and under zero bias is quite high. There are two reasons for this. First, for an ideal electroabsorption modulator, the heavy-hole excitonic absorption

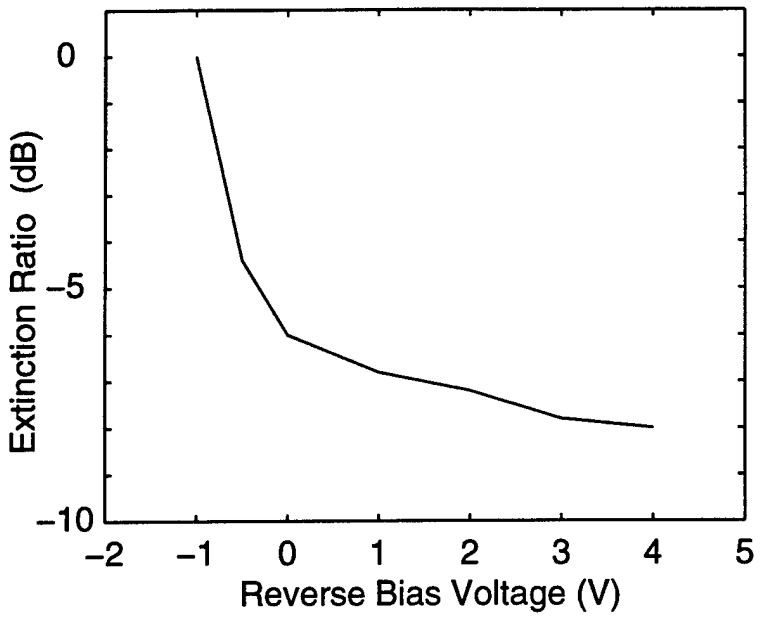

Figure 5.12: Extinction characteristics of a 120 μm long integrated waveguide operated with forward and reverse bias.

should be blue shifted from the energy of the incident photons by about $30-50\ meV$. This much of a shift is not obtained in using the same structure for both laser and modulator, in spite of the bandgap narrowing in the laser. Second, since the active region contains quarternary InGaAsP wells, the alloy broadening of the excitonic resonances is large. Therefore, with the application of any appreciable reverse bias, phase space filling and screening of the electric field by photoexcited carriers [110] will dominate the normal electroabsorption behavior. The positive bias reduces this effect and drives the waveguide towards transparency. However, this positive bias will increase the frequency chirp as well as the power consumption. Also, it should be pointed out that for better chirp performance, an antireflection (AR) coating on the output facet of the active waveguide is necessary to prevent the optical reflected back to the laser cavity.

5.8 Small-Signal Modulation Characteristics

The high-frequency small-signal modulation characteristics of the integrated modulator were measured by mounting the integrated devices on a microwave carrier with a 50 Ω terminating resistor wire bonded in parallel with the modulator. The modulator is biased at a dc bias of $-0.5\ V$ with a 2 V peak-to-peak swing. The laser driving current is 70 mA, giving a coupled optical power of about 5 mW in the modulator waveguide. A microlensed fiber is used to couple light out of the cleaved modulator facet and is pigtailed to a high-speed 40 GHz InGaAs detector. The output signal from the detector is fed to a spectrum analyzer (HP 8593A). We have measured the direct modulation characteristics of 300 μm long discrete ridge waveguide lasers made with the same heterostructure. A value of $f_{-3dB} = 11\ GHz$ is measured and is shown in Fig.5.13. The measured modulation characteristics of a 120 μm coupled modulator with input from the integrated laser is shown in Fig.5.14. A bandwidth of $f_{-3dB} \geq 14\ GHz$ is obtained. This compares favorably with the best values of $\geq$ 20GHz reported recently [19].

The equivalent circuit of the modulator, treating it as a discrete element, is shown in Fig.5.15. First, a lumped-element circuit model based on the device configuration was built, where r is the series resistance, C_i is the capacitance of the undoped active and inner cladding regions, and C_p and L are the capacitance and inductance introduced from the wire bonding and airbridge interconnection pads, respectively. I_p represents the induced photocurrent from the absorption layer. The values of the circuit elements are determined by analyzing the measured S-parameters with the microwave circuit simulator, $LIBRA$, and then optimizing each element individually. The resistance r can be neglected compared to the impedance of C_i and C_p shows

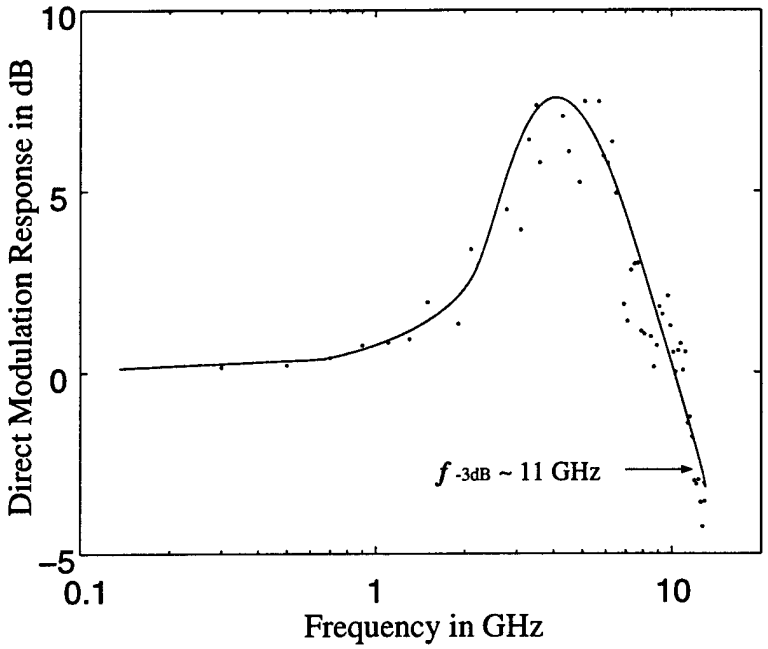

Figure 5.13: Direct modulation response of a 300 μm long laser.

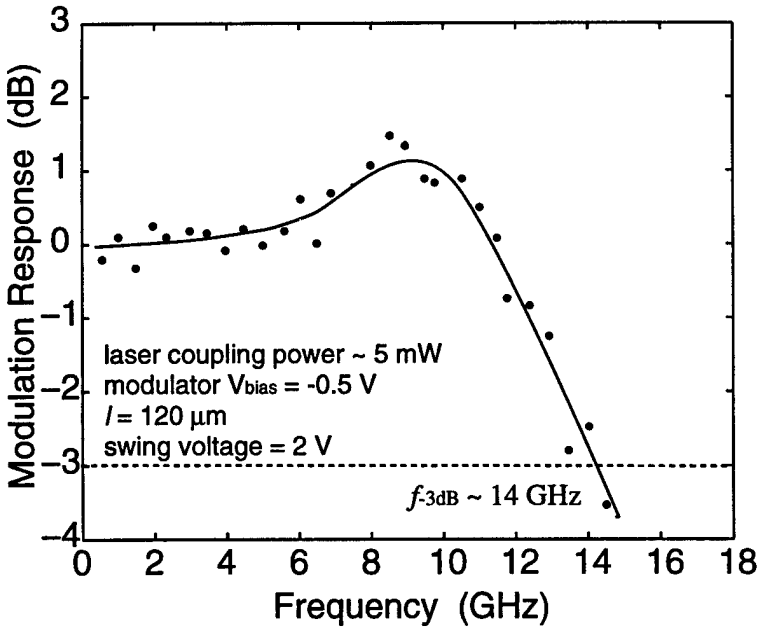

Figure 5.14: Frequency response of the 120 μm long MQW modulator.

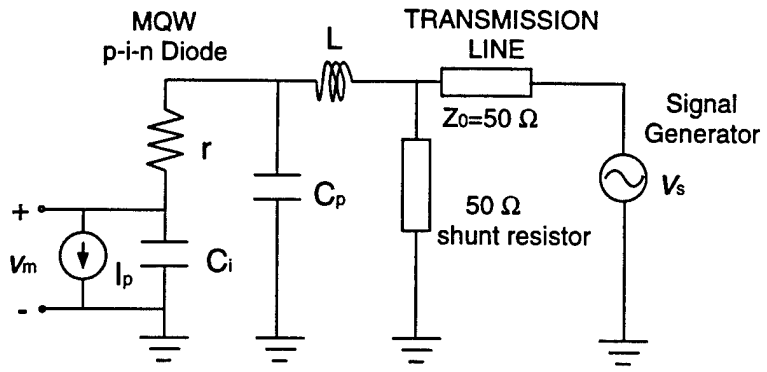

Figure 5.15: Equivalent lumped-element circuit model of the modulator.

a high impedance in this operation frequency range. The electrical bandwidth of the circuit derived from the RC time constant is approximately 20 GHz, which is higher than the value obtained from the optical modulation measurements. The photocurrent, I_p, generated by the strong absorption is quite large and it causes the bias V_m to decrease due to the device impedance. Physically, the large number of photogenerated holes which accumulate in the quantum wells under high-frequency modulation are trapped and degrade the device high-frequency performance. It is also important to note that the high frequency performance will degrade since the diode is driven to a forward bias, where the diffusion capacitance becomes important. The device frequency response may be improved by designing shallower wells in the absorption region and patterning the substrate to optimize the energy difference between the laser light and the excitonic absorption peak.

5.9 Summary

The performance characteristics of a coupled cavity InGaAsP / InP MQW laser / active waveguide made by one step expitaxy and well-controlled reactive ion etching (RIE) have been studied. The calculated effective reflectivity of the coupling region

consisting of two facets and an air gap is between 0.45 and 0.55, which is in a good agreement with the experimentally measured value of 0.5. The reflectivity of a single etched mirror derived from this value is estimated to be 0.3. A 120 μm long monolithically integrated active waveguide when biased as a modulator and excited by the laser shows a maximum extinction ratio of 8 dB and a modulation bandwidth $\geq$ 14 GHz at a dc bias of -0.5 V with a bias swing of 2 V.

CHAPTER VI

DESIGN AND ANALYSIS OF INTEGRATED TRANSMITTERS

6.1 Introduction

The InP-based optoelectronic devices are of great interest for operations at wavelengths between 1.3–1.55μm. Monolithic integration of electronic and opto-electronic devices, forming optoelectronic integrated circuits (OEIC), to achieve high functionality, low optical or electrical insertion loss, small size, and cost-effectiveness is always a goal for researchers to pursue. So far most of the works conducted on integrated optical transmitters are either the laser/modulator integration [19]–[24] or laser diode and driver circuits integration [111],[112].

In this work, the integration is extended to integrate laser diode, external modulator, and driver circuit monolithically. Contrary to producing discrete devices, which allows much more freedom to optimize the design of individual device, realizing integration, however, encounters several constraints among the design and fabrication of different devices. Therefore, tradeoffs are necessary in general. This chapter starts with the fabrication and modeling of single heterojunction bipolar transistors (SHBT) followed by the design and characterization of two simple circuits for driving the laser and modulator. A coupled-cavity integrated laser/modulator with different

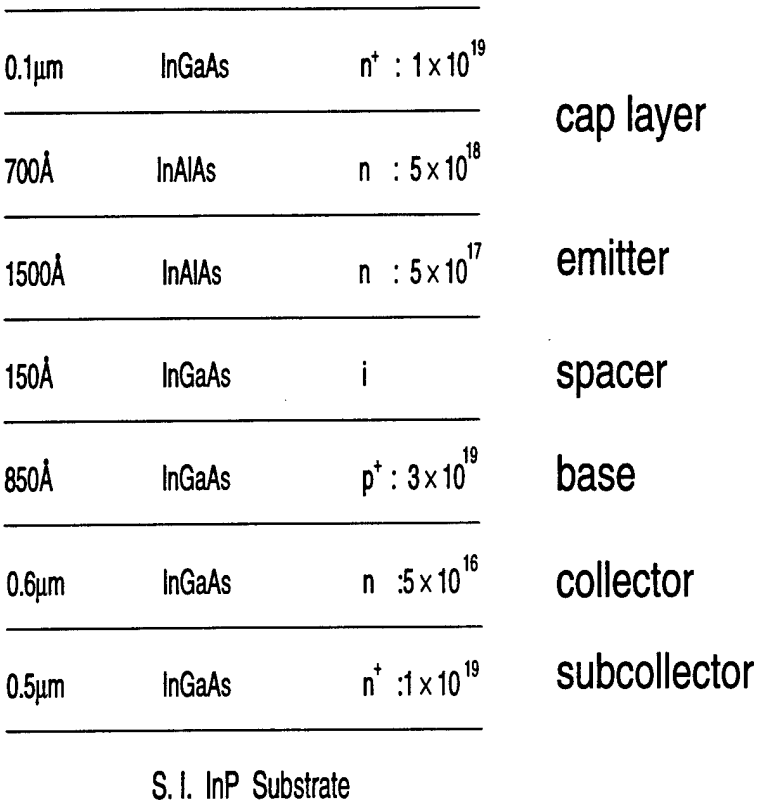

Figure 6.1: HBT epilayer structure grown by MBE.

active regions grown in butt-coupling scheme is described later. Finally, a design of an integrated optical transmitter is addressed.

6.2 Single Heterojunction Bipolar Transistors

HBT's are known to have wide bandwidth, high current gain, and high output power [116] and are suitable for laser driver applications, whose operation generally requires a large amounts of current. In this work, the InAlAs/InGaAs SHBT is used and its heterostructure grown by MBE is shown in Fig.6.1. The transistors are fabricated by standard HBT processing procedures, shown in Fig.6.2.

Since the device high frequency performance characteristics and the power handling capability are mainly determined by transistors' emitter sizes, the rule-of-thumb

1. Emitter metal (Ti/Pt/Au) &
   RIE selectively etch InGaAs cap layer
   (CH_4 : H_2 = 6 : 34, @ 50 W, 15 mT)

2. Wet etch down to base layer
   (using selective etchant = H_3PO_4 : H_2O_2
   or nonselective etchant = HCl)
   & base metal (Pt /Ti /Pt/Au) + short RTA
   (375 °C for 7 sec)

3. Cap emitter-base junction with photoresist
   & etch down to subcollector.

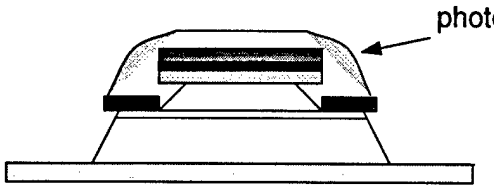

4. Collector metal (Ti/Pt/Au)
   & isolation etch down to S.I. InP substrate

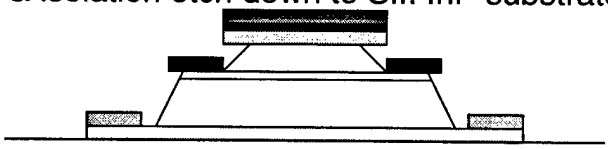

5. PECVD SiOx passivation + via hole
   & Ni/Cr resistor deposition
   (25 Ω/□, □ = 10μm × 10μm)

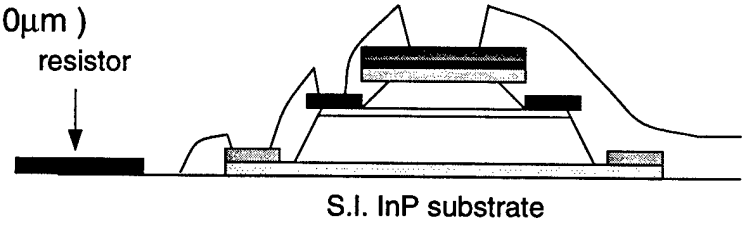

6. Interconnection metal (Ti/Al/Ti/Au)

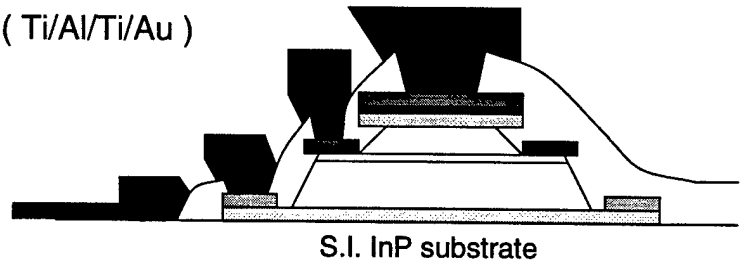

Figure 6.2: HBT's circuits processing flow.

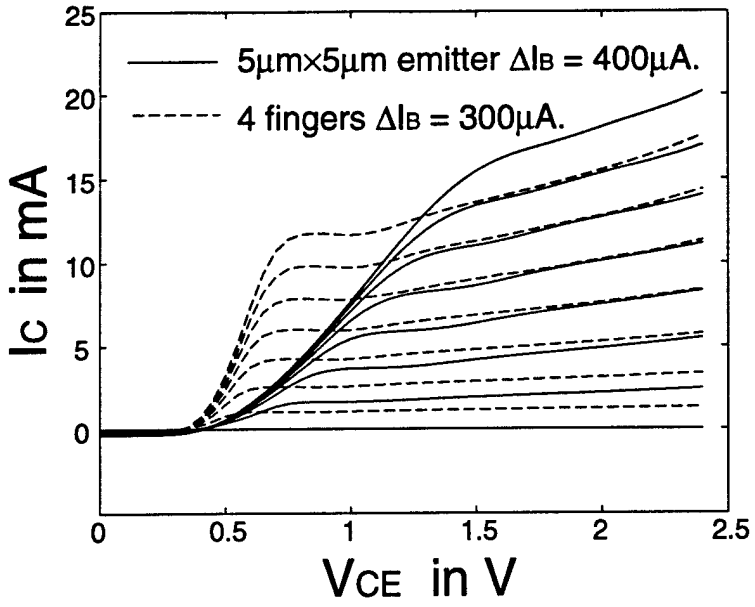

Figure 6.3: HBT's common-emitter configuration I-V characteristics.

is to adopt different kinds of transistors for different applications. Two kinds of transistors with different emitter sizes are of interest here. Figure 6.3 shows the transistors' I-V characteristics. The small emitter size (5 μm $\times$ 5 μm) transistors are used for high-speed applications, while the large emitter size (4 fingers, with the finger size of 5 μm $\times$ 10 μm) transistors are used for high power applications. The typical DC current gain β is around 50–60 and the ideality factor η is around 1.5–1.7. The offset voltage ΔV_{CE} is 0.5V, BV_{CEO}=4.5V, and BV_{CBO} is around 7–9V. The fabricated devices are shown in Fig.6.5 and Fig.6.6, respectively.

The high-frequency performances of small area devices are shown in Fig.6.7 and Fig.6.8, respectively. A untiy current gain cutoff frequency f_T of 50GHz and a maximum oscillation frequency f_{max} were measured at a collector current of 18mA.

The discrete transistor is modeled by an equivalent circuit shown in Fig.6.9 with the parameters extracted from the S-parameters measurement [116]. The SPICE parameters used in DC simulations are also provided.

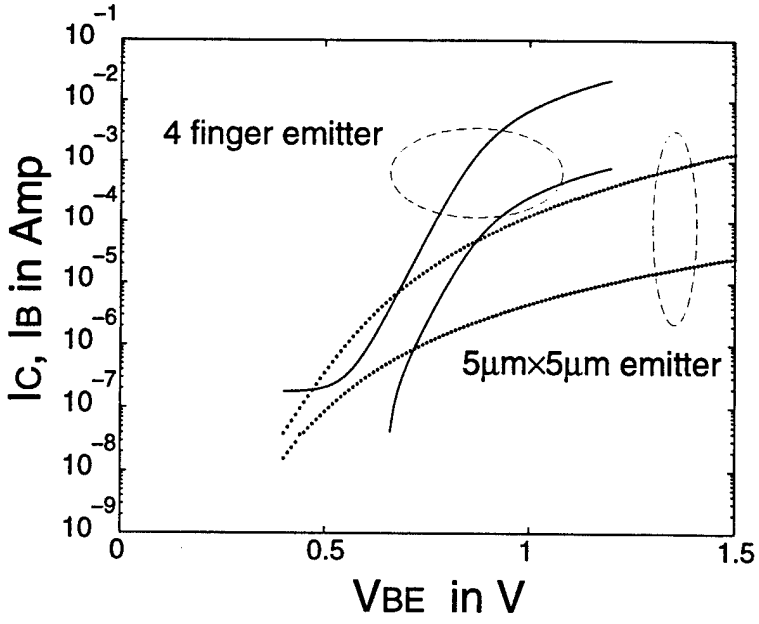

Figure 6.4: HBT's Gummel-Poon plot.

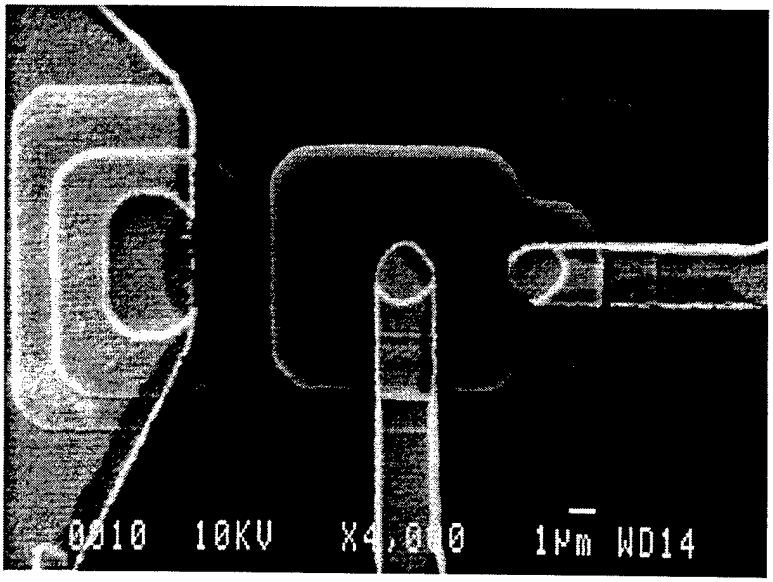

Figure 6.5: SEM picture of fabricated $5\mu m \times 5\mu m$ emitter HBT.

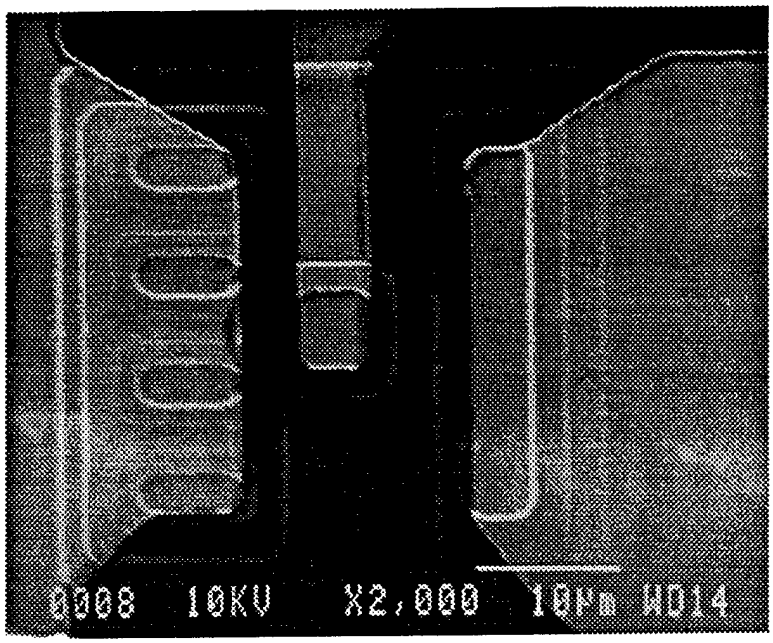

Figure 6.6: SEM picture of fabricated 4 fingers emitter HBT.

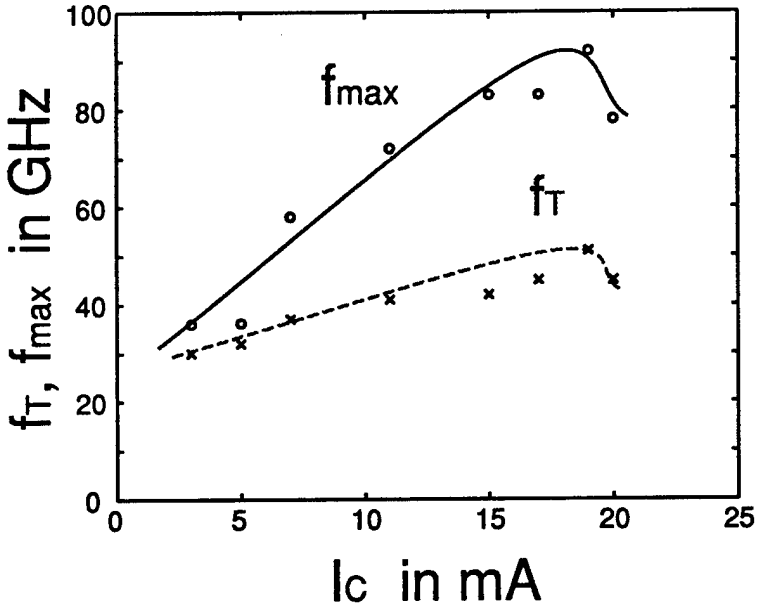

Figure 6.7: High frequency current gain and maximum available gain of a discrete 5μm $\times$ 5μm emitter HBT.

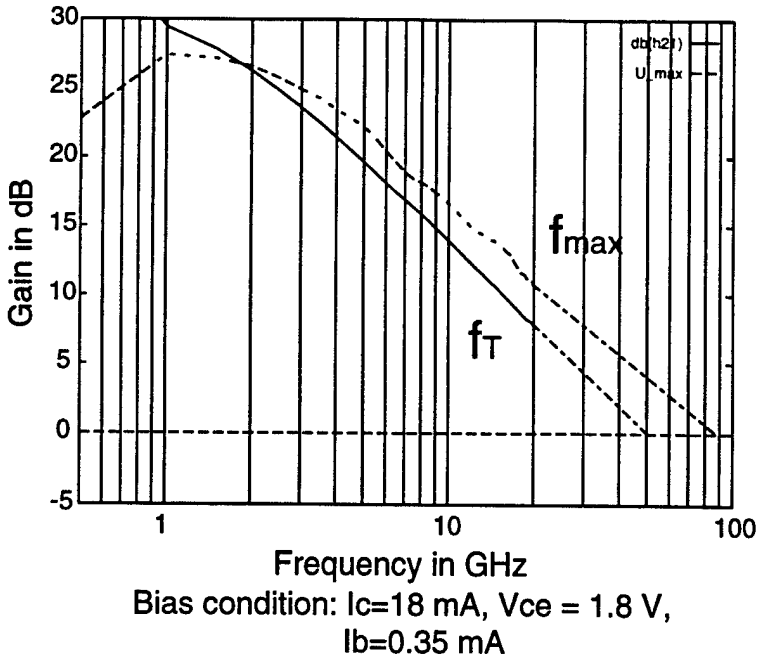

Figure 6.8: Relation of f_T and f_{max} versus I_C.

6.3 HBT's Circuits

6.3.1 Driver Circuits for Laser Diodes

Figure 6.10 illustrates the operation principle of the designed laser driver. The laser is biased at a constant DC bias point (D_Q) plus a time-varying AC signal, which modulates the laser diode if the direct modulation is used. The laser operation point is chosen right above the threshold current so that the chirp problem will not be severe. However, it cannot be too close to the threshold current since it will cause serious chirp problem and the laser output power may change if considering the laser aging problem. Suppose the laser has a threshold current around 20–30mA, which is the case in Chapter 3, the optimum bias point is around 40–50mA. The designed driver circuit shown in Fig.6.11. It consists of a current mirror (Q_5–Q_8), which sets the bias point I_Q, and a differential amplifier (Q_1 and Q_2), which translates a small voltage signal to an amplified current signal for modulating the laser diode. The rest

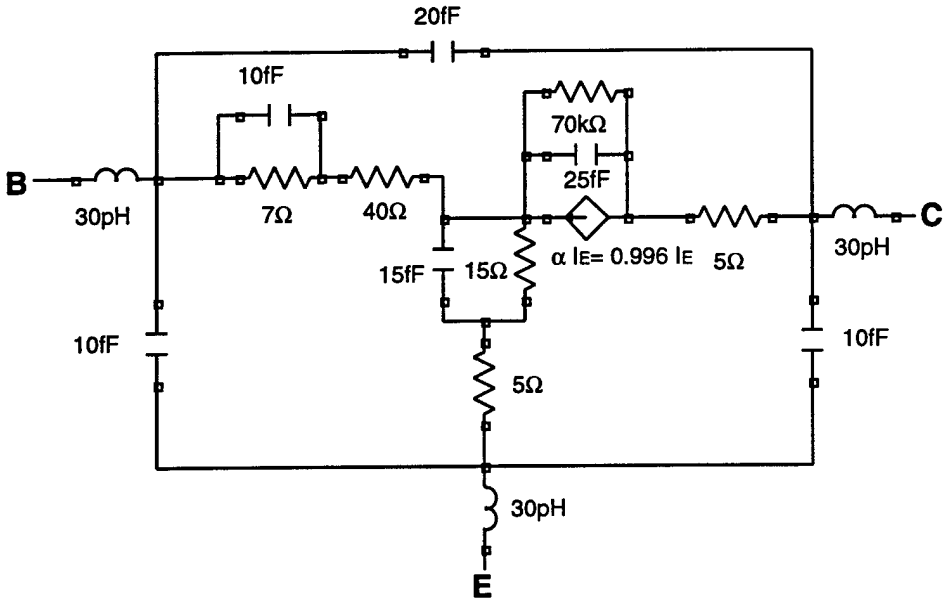

SPICE Model-

IS=1e-16 A	RE=5 Ω
ISE=1.5e-15 A	RB=7Ω
ISC=7.5e-12 A	RC=5 Ω
IKF=1e-5 A	NF=1.35
IKR=5.8e-7 A	NE=1.55
BF=50	NR=1.06
BR=0.1	NC=1.18
NKF=0.096	

Figure 6.9: 5 μm $\times$ 5μm HBT's equivalent circuit model.

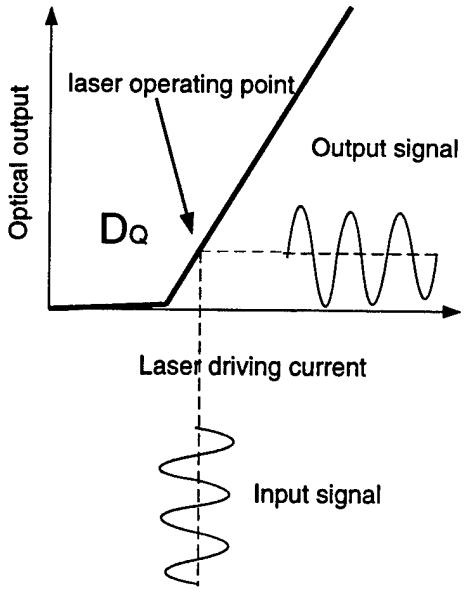

Figure 6.10: The laser driver circuit operation principle.

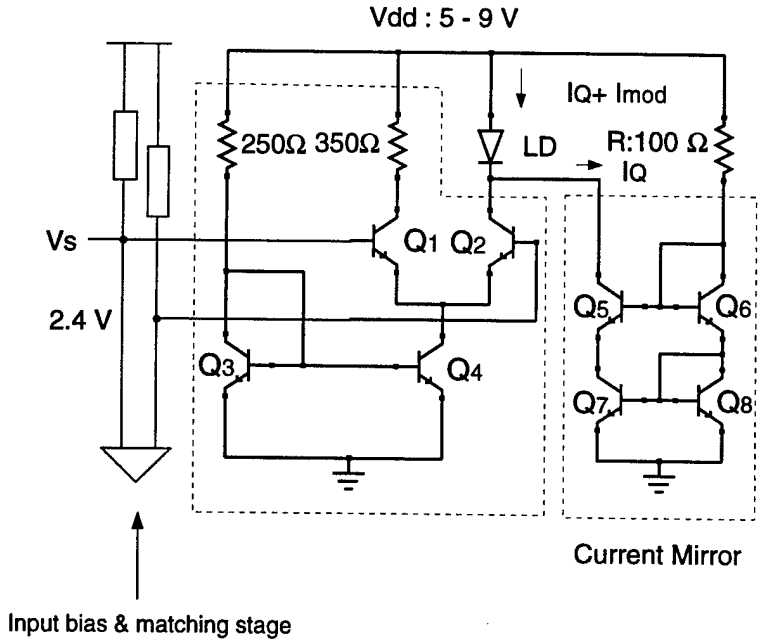

Vs = 2.4 V + small signal (fed in through bias tee and an 50Ω termination resisitor in parallel).
LD is in series with a 20Ω thin film (Ni-Cr) resistor.

Figure 6.11: Designed laser driver circuit.

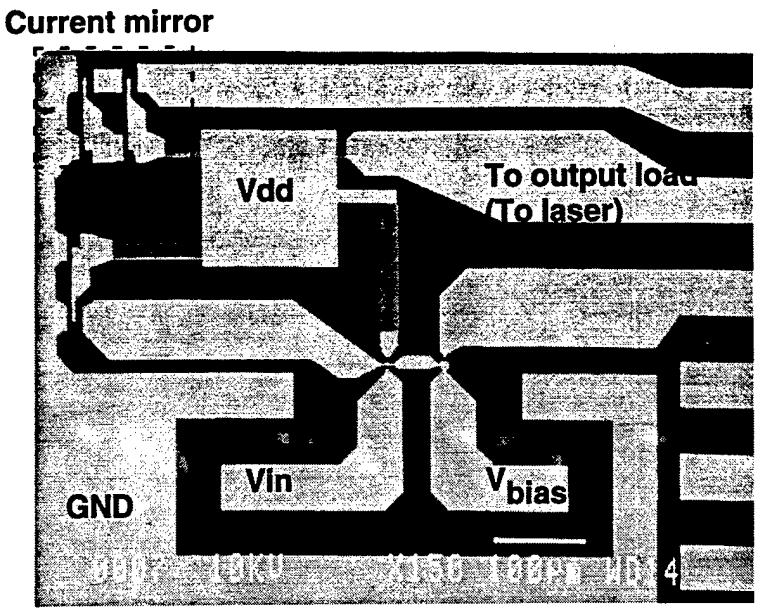

Figure 6.12: Fabricated laser diode driving circuit.

of elements are biasing circuits. Since the current mirror provides the laser DC bias point large area (4 fingers) devices are used in this case. Meanwhile, the differential amplifier does not need to drive too much current but requires good high-frequency performance characteristics, the small area (5μm $\times$ 5μm) devices are employed and the bias points are set around 12mA in this design. The laser diode (LD) is in series with a 20Ω Ni-Cr thin film resistor for short-circuit protection.

The fabricated circuit microphotograph is shown in Fig.6.12. The circuit DC driving capability with a 10 Ω surface mounting technology (SMT) thin film resistor, which is in place of a real laser diode, wire-bonded to the load is shown in Fig.6.13. The current level can be set either by the resistor R or by Vdd in this case. The circuit high-frequency modulation characteristics will not be measured until the laser is included in this integration.

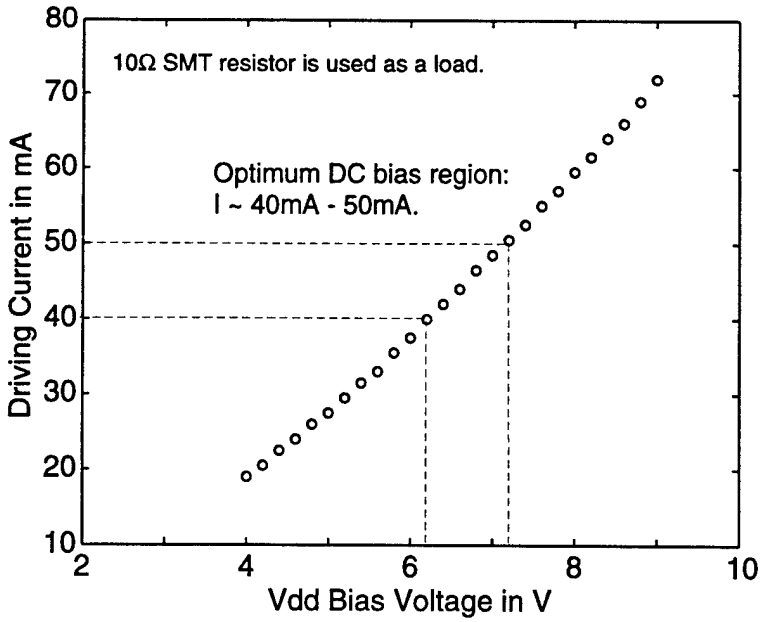

Figure 6.13: Measured circuit driving capability with a 10Ω load resistor.

6.3.2 Feedback Amplifier Circuits

The QCSE electroabsorption modulator is normally reversed biased at the point where the slope of $\Delta P_{out}/V_{bias}$ is the largest, as depicted in Fig.6.14. From Chapter 4, this biase point is around -1.5~3V. In this work, a series-shunt feedback amplifier circuit, shown in Fig.6.15, is designed to transform a small voltage signal into a large voltage swing ($V_{p-p} \sim$ 1–1.5V). The first two stages (Q_1, Q_2) are the gain stages and the output stage (Q_3) provides a small output impedance. The output DC level is set at -1.5V. The feedback resistor R_f offers a high input impedance and a flat output response. The amplifier gain is decided by R_f and R_{E1}, according to the relation:

$$A_v = \frac{v_{out}}{v_{in}} \simeq \frac{R_{E1} + R_f}{R_{E1}} \tag{6.1}$$

and is estimated to be 17dB in this design.

Figure 6.16 shows a microphotograpg of a fabricated circuit. To measure the circuit high-frequency characteristics, the RF signal is combined with a DC bias

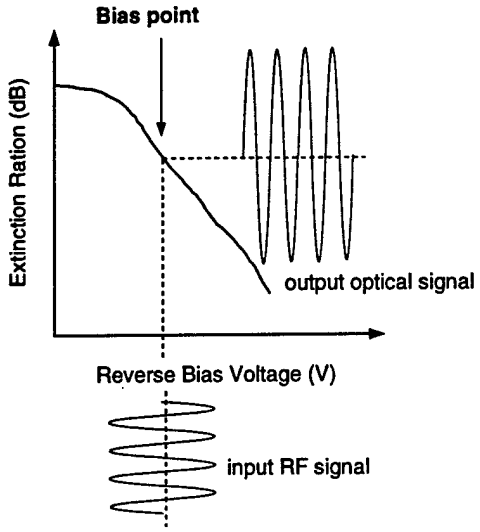

Figure 6.14: QCSE electroabsorption modulator operation principle.

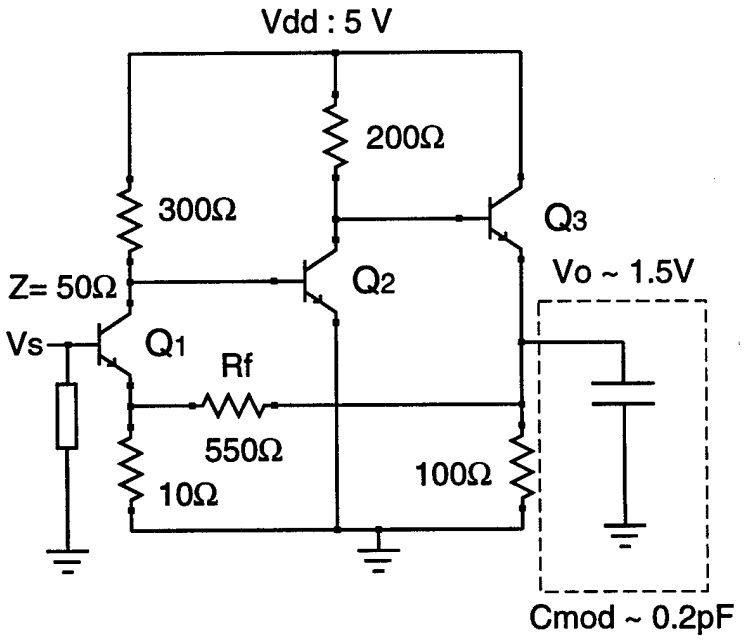

Vs =1.25V + small signal (fed in through bias tee).

Total power consumption = 210mW

Figure 6.15: Designed Feedbak amplifier circuit for driving a modulator.

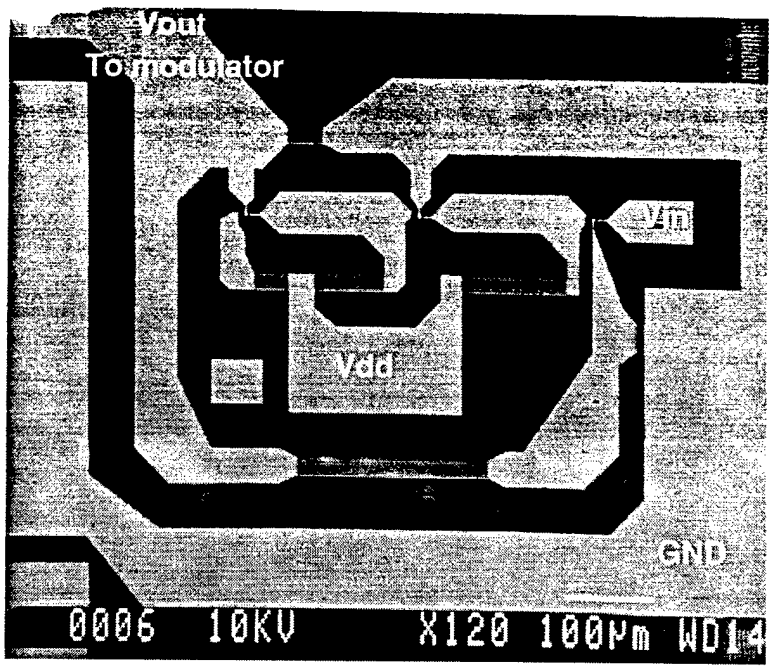

Figure 6.16: Fabricated feedback amplifier circuit.

voltage through a bias-Tee. A 50Ω termination is in shunt with the input port. The measured bandwidth of this circuit without resistance or capacitance load is shown in Fig.6.17. The circuit shows a flat low frequency gain of 15dB and a -3dB bandwidth about 2.5–3GHz. The poor bandwidth performance is believed due to the mismatches at the input port and output port. The amplifier shows a linear gain from -10dBm– +5dBm at the input port. The total power consumption of this amplifier is about 210mW.

6.4 Coupled-Cavity Integrated Transmitters with Different Active Regions

The results obtained in Chapter 5 indicates that the ON/OFF ratio (only $\sim$ 8dB) of a coupled-cavity integrated transmitter using the same active resgion is not large enough due to severe absorption loss. This is because the laser wavelength is too close to the MQW excitonic peak. The solution is to use different active

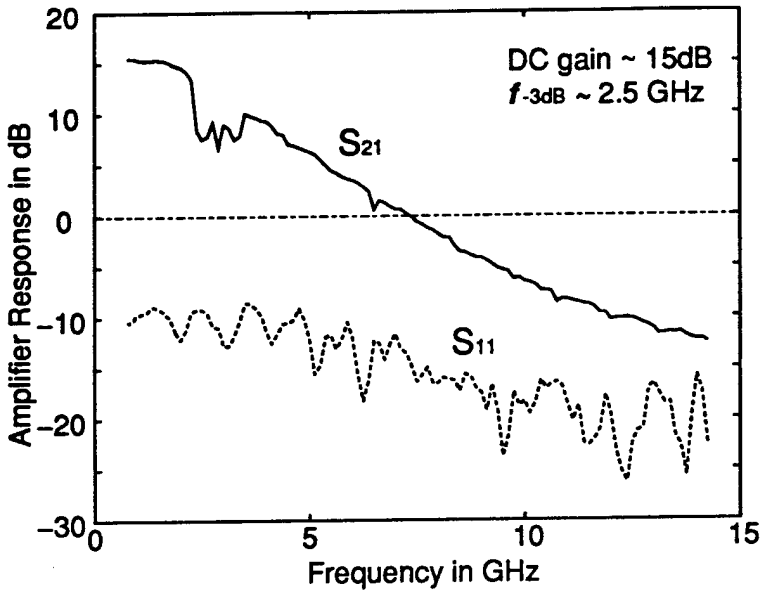

Figure 6.17: Frequency response from the feedback amplifier circuit.

regions for the laser gain region and modulator absorption region. In this work, the butt-coupling scheme is adopted to achieve the integration of a laser and modulator.

First, a tunneling injection laser structure is grown on an InP substrate and the heterostructure grown by MOCVD is shown in Fig.6.18. The laser active region is then patterned with photoresist and the rest areas are selectively etched to the lower cladding layer, as pointed in Fig.6.18. The modulator heterostructure, shown in Fig.6.19, is regrown next on top of the entire wafer by MBE. The thickness of each layer is carefully controlled so that the laser active region is precisely aligned with the modulator active region. Figure 6.20 shows the cross section of the regrown sample.

The device processing procedures are as follows: first, the redundant regrowth material on top of the laser active region has to be removed before the process. The 3μm wide waveguide metal (Pd/Zn/Pd/Au/Ni) is then deposited to form the p^+: contact. A thick SiO_x ($\sim$ 6000Å) is deposited and patterned as a RIE etching mask.

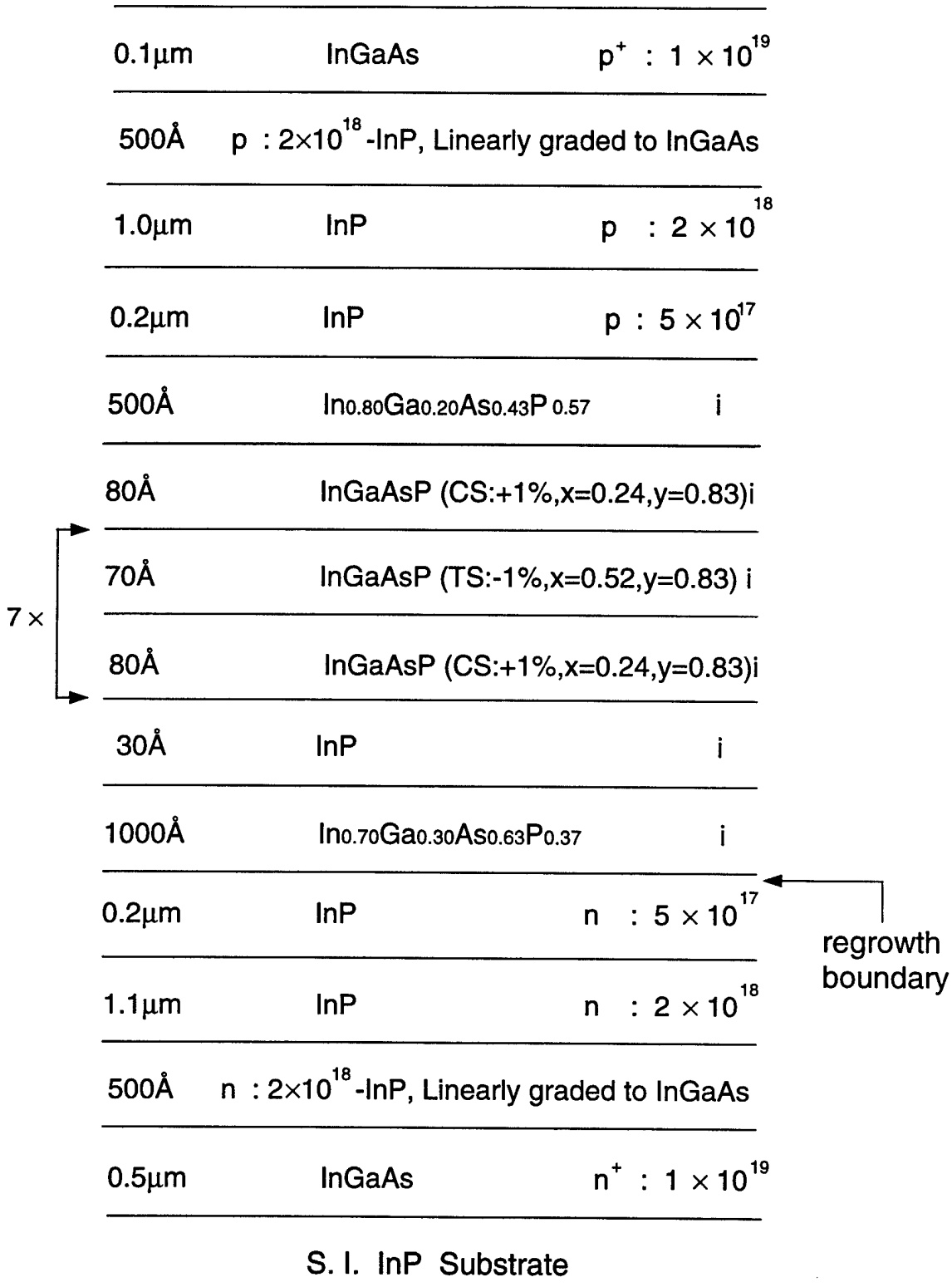

Figure 6.18: Tunneling injection laser heterostructure grown by MOCVD.

p-i-n InGaAs/InAlAs QCSE EA Modulator
(Regrowth Part)

0.1μm	InGaAs	$p^+ : 1 \times 10^{19}$	
1.2μm	InAlAs	$p : 5 \times 10^{17}$	
500Å	InAlAs	i	
110Å	InGaAs(-0.5% strain)	i	12 prd
80Å	InAlAs (+0.5% strain)	i	
500Å	InAlAs	i	
Regrowth Boundary			

Figure 6.19: Modulator heterostructure regrown by MBE.

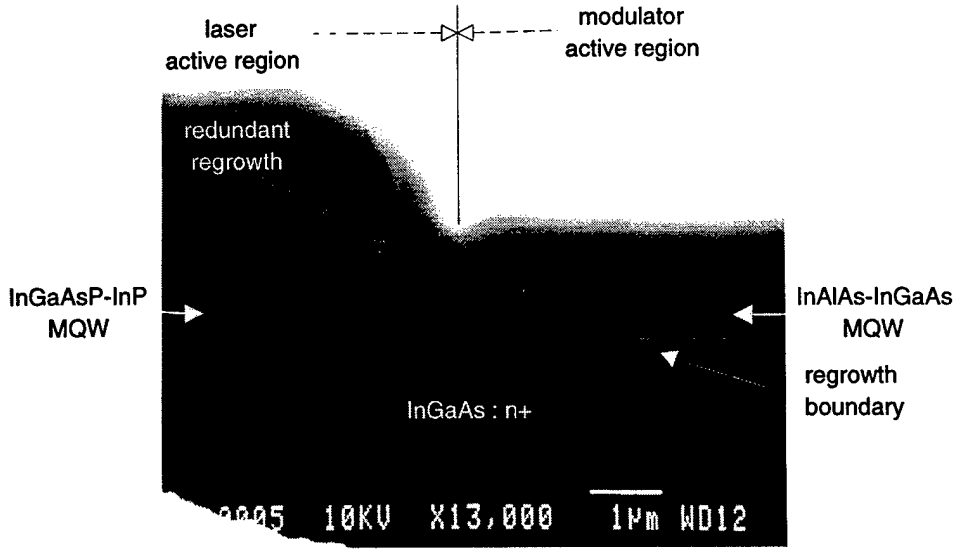

Figure 6.20: SEM picture showing the cross section of the regrown sample.

The coupling facets is formed by the RIE with $Ar/CH_4/H_2$ (8:6:56) mixture at 200W. Next, the ridge waveguides for the laser and modulator are separately formed by the combination of RIE etch and wet chemical etch. A mesa, down to the the bottom contact layer is formed by wet chemical etching and this is followed by evaporation of Ni/Ge/Au/Ti/Au as the n-contact metal. A thick SiO_x ($\sim$ 8000Å) is deposited as a passivation and a thick contact metal pad (Ti/Al/Ti/Au) is evaporated finally.

The primary etching gases for the InGaAsP/InP systems are the CH_4/H_2 mixtures, however, these gases are not a good choice for the InAlAs/InGaAs systems. Instead, the BCl_3:Cl_2:Ar mixtures are more appropriate. Since the coupling facets are located at the boundary of these two different material systems and the etching gases used here are the CH_4/H_2 mixtures, which cause serious etching problems in the modulator active regions, and the devices did not work at the first time. Further investigation is required to optimize this integration process.

6.5 Integration Design

Chirp performance is one of the most important figures-of-merit in evaluating the characteristics of a transmitter, especially for long-distance data transmissions. The light source in the coupled-cavity integrated transmitter is from a conventional F-P laser and the linewidth is in general too wide to satisfy the requirement in modern communication systems. Incorporating a DFB laser in the integration becomes essential for the design. One thing has to be noticed is that a good electrical and optical isolation between the DFB laser and the modulator are indispensible for a high performance integrated laser/modulator transmitter.

If the isolation resistance between the two devices is small, the injection current to the laser is decreased considerably as the bias voltage to the modulator increases.

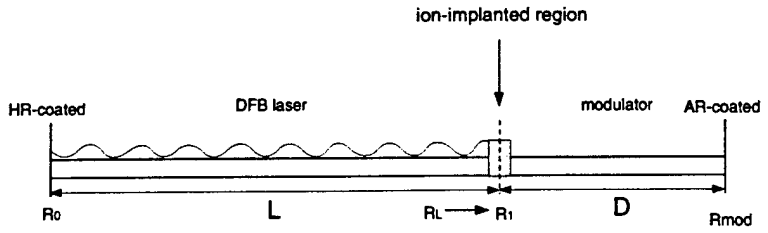

Figure 6.21: Schematic of proposed integrated DFB laser and electroabsorption modulator.

This will result in an increase of the threshold current, a decrease of the laser output power, and a change of lasing wavelength [113]. The effective voltage applied to the modulator will also be reduced. In addition, the small isolation resistance creates a large capacitance between the forward-biased laser and reverse-biased modulator, which obviously will affect the transmitter's high frequency performance.

The optical interaction bewteen the the two devices arises mainly from the reflection light from the modulator output facet. This modulated light when feedback into the laser cavity will alter the lasing properties, such as increasing chirp, and the laser output power [114]-[115].

Figure 6.21 shows the schematic of the laser-modulator integration. In this case, R_0 should be high-reflection (HR) coated to reduce the laser threshold current and R_{mod} should be anti-reflection (AR) coated to prevent the modulated light reflected back from the facet. Ino-implantation at the boundary between the two devices to provide a good electrical isolation is essential. The entire integrated transmitter layout design is also shown in Fig.6.22. This design includes a 600μm long waveguide for the laser, 100–200μm long waveguide for the modulator, and two HBT's driving circuits. Since the sample is subject to cleave once processed, the sizes of the circuits are limited by the laser cavity length. This limitation prohibits a complicate design in these circuits.

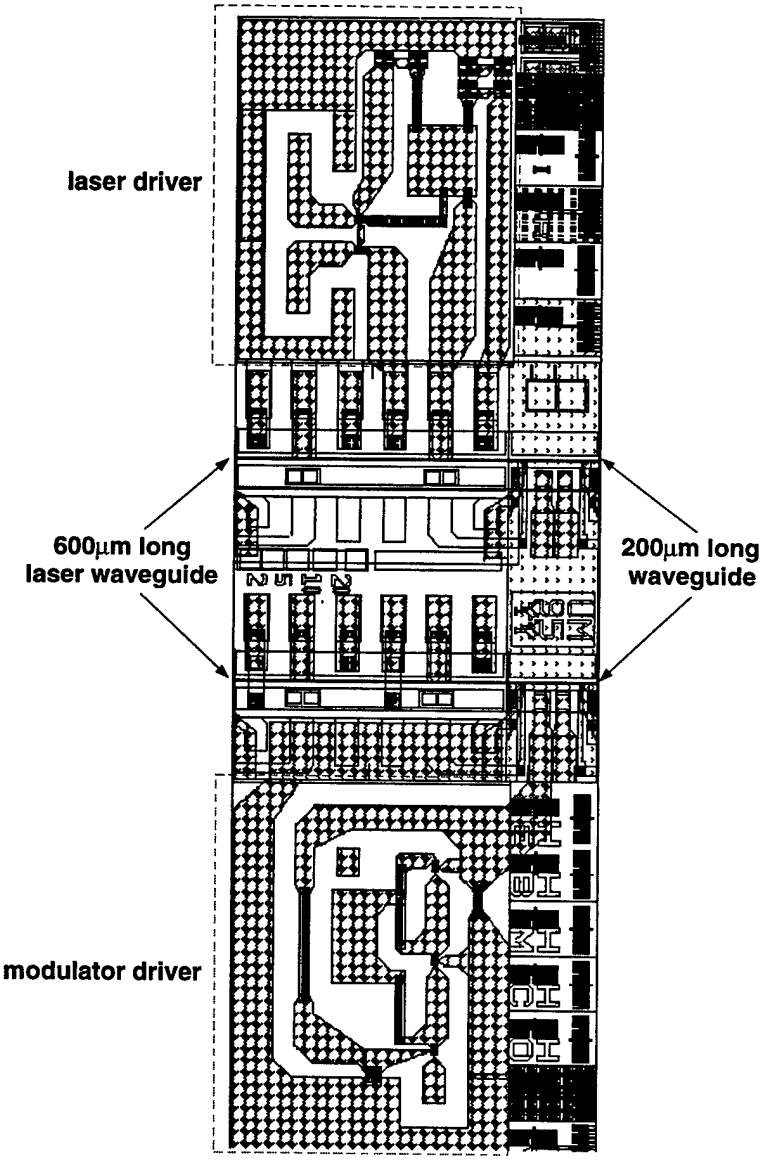

Figure 6.22: Integrated transmitter layout.

1. Grow DFB laser structure (including, gratings etch & regrowth.). Pattern the laser region, using SiOx as dry etch mask and RIE technique, $CH_4 : H_2 : Ar = 6: 56: 6$, @ 15mT, 150 W.

2. Regrow QCSE EA modulator and HBT structures. Inbetween an InAlAs - i buffer layer is inserted. The regrowth layers on top of laser and HBT structure on top of modulator is selectively etched away.

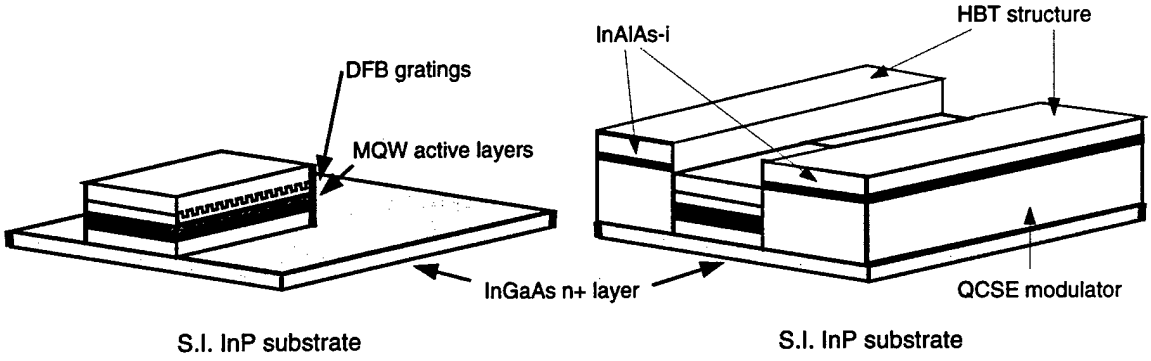

3. Process laser & waveguide modulator altogether.

   p+ contact annealing temperature is 450°C,
   n+ contact annealing temperature is 400°C.

4. Process HBT circuits.

   contact annealing temperature is 375°C.

❑ Process flow : Thermal budget consideration.

Figure 6.23: Proposed processing flow for the integrated transmitter.

The entire monolithically integrated transmitter processing flow is illustrated in Fig.6.23. Here the strategy is to fabricate the laser and modulator before HBT's circuits. The consideration is the process thermal budget. Usually, the laser and modualtor require higher anealing temperature to obtain good ohmic contacts. High anealing temperature might cause short circuits between HBT's base and collector (B-C) junctions.

6.6 Summary

High performance single heterojunction bipolar transistors (HBT's) have been characterized and modeled. A laser drivier circuit and a feedback amplifier circuit

based on these transistors are made. The laser driver shows a high current driving capability and the feedback amplifier shows 15dB gain at low frequency and a 3dB bandwidth of 2.5–3GHz. Incorporating the input and output matching circuits design is needed to improve the cirucit high frequency performance.

A coupled-cavity integrated transmitter with different active regions is investigated. Further improvement in the entire process is required to realize this integration. In addition, a design of a monolithic integration of a DFB laser, an electroabsorption modulator, and HBT's driver circuits are discussed. Detailed layout design and process flows are provided as well.

CHAPTER VII

CONCLUSION AND FUTURE WORK

7.1 Review of Current Work

With the motivation of developing and producing high performance light sources and integrated transmitters that would be useful in the next generation telecommunication systems, I have investigated the modeling and design, fabrication and characterization of the individual components and the integration among these devices. Some new device concepts and designs are proven and some of the state-of-the-art performance characteristics are achieved.

Short-cavity edge-emitting distributed Bragg reflector (DBR) lasers, realized by deep reactive ion etching (RIE) etched DBR mirrors, make $\sim 10\mu$m long devices feasible and lead to the possibility of realization of true gain-compression limited bandwidth. A reliable and reproducible device processing technique has been developed. A low threshold current (4.5mA) and reasonable high modulation bandwidth ($\sim$ 30GHz) 100μm long device is demonstrated for the first time. In addition, the far-field pattern emanating from these DBR mirrors shows a great potential in spatial filter applications.

The tunneling injection mechanism in a quantum well laser, which is known to minimize hot-carrier effects, was incorporated into the design of a distributed

feedback (DFB) laser for the first time. A series of device processing techniques have also been developed. By fitting the experimental data with the empirical relation for temperature dependence of threshold current, a characteristic temperature T_0 of 70–120K is obtained at room temperature. This is the highest value obtained for a 1.55μm laser. Other characteristics of these lasers have also been measured. For a 300μm long device, the lowest threshold current is 22 mA and the highest small-signal modulation bandwidth is 7.5 GHz. The temperature tunability is about 1Å/°C. The $\lambda/4$-shifted DFB laser preserves a single-mode operation up to 120mA.

An InAlAs/InGaAs, with 0.5% strain-compensated MQW, waveguide modulator has been designed, fabricated, and characterized. The measured photocurrent spectra verifies the original design and the optical transmission characteristics demonstrate a good optical modulation. A 9GHz modulation bandwidth from a 400μm long device has been obtained. A new scheme of reducing the photocurrent of a quantum confined Stark effect multiple quantum well modulator is demonstrated. The GaAs well regions of the 50 period GaAs/$Al_{0.3}Ga_{0.7}As$ multiple quantum well are selectively doped with Er during molecular beam epitaxy to reduce the carrier lifetime to the order of picoseconds. 250 μm diameter mesa-shaped devices have been characterized. The photocurrent responsivity is as low as 0.005 A/W and an extinction ratio greater than 1:8 is achieved at a bias voltage of 8 V.

Monolithic integration of laser/modulator by coupled-cavity scheme is carried out in the cases of identical and different active regions. This study represents the first detailed investigation of such a scheme. High performance HBT's (β= 50-60, f_T= 50GHz, f_{max}= 90GHz) has been characterized and successfully implemented in the driver circuits design. The design and analysis of monolithically integrated laser, modulator, and HBT driver circuits are described and discussed at the same time.

7.2 Suggestions for Future Work

7.2.1 DFB Lasers

The DFB lasers presented in Chpater 3, have demonstrated some promising results, as it is the first attempt to make a DFB device here at the University of Michigan. However, the relatively higher threshold current and poorer modulation bandwidth indicate that further improvement in device structure design and processing techniques have to be performed. In real WDM applications, furthermore, the lasing wavelengths have to be precisely controlled within 2nm $\sim$ 4nm. Many experimental results [1] concludes that it is almost impossible to uniformly control the lasing wavelengths throughout the entire wafer even though the device process is near perfect. This suggests that for the future WDM light sources, the DFB laser arrays with multielectrodes, which have a great controllability of lasing wavelengths in static and dynamic operations, are essential and worth being investigated. In addition, DFB lasers with chirped gratings attract considerable attention recently as they reveal higher single-longitudinal mode stability, higher output power, and narrower linewidth. A complete theoretical model is required to understand the physics and operation principles behind this concept. Developing an effective and a reliable process in achieving high quality DFB gratings is indispensible as well.

7.2.2 Monolithically Integrated Transmitters

In Chapter 6, I proposed a design to realize the integration of a DFB laser, modulator, and the driver circuits. Several considerations have to be taken to ensure a successful integration. These include an effective and reliable DFB laser fabrication technique, an optimized modulator structure, and appropriate matching circuits between the driving circuits and the laser diode or modulator. In addition, a good

electrical and optical isolation between the laser and the modulator is important, as addressed previously.

From the device application point of view, the device packaging technology has been becoming an important issue as the operation frequency reaches to 20GHz or even beyond. Conventional bonding wires cannot provide effective electrical connections due to severe loss and serious inductance. Flip-chip bonding techniques along with properly designed microstrip lines appear to be a good approach to solve these problems.

BIBLIOGRAPHY

BIBLIOGRAPHY

[1] T.P.Lee, *et al.*, "Multiwavelength DFB laser array transmitters for ONTC reconfigurable optical network testbed", *IEEE J. Lightwave Tech.*, vol. 14, no. 6, pp.967-975, 1996.

[2] S.J.B.Yoo, "Wavelength conversion technologies for WDM network applications", *IEEE J. Lightwave Tech.*, vol. 14, no. 6, pp.955-966, 1996.

[3] C.A.Brackett, "Dense wavelength division multiplexing networks:Priciples and applications", *IEEE J. Select. Areas Commun.*, vol. 8, p.948, 1990.

[4] S.Johansson, "Transparent optical multicarrier networks", in *Proc. ECOC'92*, 1992, vol. We A9.1.

[5] G.P.Agrawal, N.K.Dutta, *Long-wavelength semiconductor lasers*, Van Nostrand Reihold, 1986, chap. 1.

[6] R.I.Laming, *et al.*, "High sensitivity optical pre-amplifier at 10Gb/s employing a low noise composite EDFA with 46dB gain", post-deadline papers, in *Optic. Amplifiers Appli. Topic. Meet., 1992*, Washington, DC, 1992, paper PD 13.

[7] R.E.Enstrom, *et al.*, *Electrochem. Soc. Ext. Abstr.*, **78-1**, p.504, 1978.

[8] A.Y.Cho, *J. Appl. Phys.*, **41**, p.2780, 1970.

[9] H.Kogelnik and C.V.Shank, "Stimulated emission in a periodic structure", *Appl. Phys. Lett.*, **18**, 152, 1971.

[10] U.Koren, *et al.*, "Wavelength division multiplexing light source with integrated quantum well tunable lasers and optical amplifiers", *Appl. Phys. Lett.*, 54, pp.2056-2058, 1989.

[11] F.Koyama, *et al.*, "Frequency chirping in external modulators", *IEEE J. Lightwave Tech.*, vol.6, no.1, pp-87-93, 1988.

[12] H.Naitoh, *et al.*, "Mirror type optical branch and switch", *Appl. Opt.*, vol.17, pp.101-104, 1978.

[13] W.E.Martin, "A new waveguide switch/modulator integrated optics", *Appl. Phys. Lett.*, vol.26, pp.562-563, 1975.

[14] K.Tada, *et al.*, "A new light modulator using perturbation of synchronism between two coupled guides", *Appl. Phys. Lett.*, vol.25, pp.561-562, 1974.

[15] G.E.Stillman, *et al.*, "Electroabsorption in GaAs and its application to waveguide detector and modulator", *Appl. Phys. Lett.*, vol.28, pp.544-546, 1976.

[16] D.S.Chemla, *et al.*, "Electroabsorption by Stark effect on room temperature exciton in GaAs/AlGaAs multiquantum well structure", *Appl. Phys. Lett.*, vol.42, pp.864-866, 1983.

[17] I.Kotaka, *et al.*, "High-speed InGaAlAs/InAlAs multiple quantum well optical modulators with bandwidths in excess of 20GHz at 1.55μm", *IEEE Photon. Technol. Lett.*, vol.1, no.5, pp.100-101, 1989.

[18] T.Ido, *et al.*, "High-speed MQW electroabsorption optical modulators integrated with low-loss waveguides", *IEEE Photon. Technol. Lett.*, vol.7, no.2, pp.170-172, 1995.

[19] A.Ramdane, *et al.*, "Monolithic integration of multiple-quantum-well lasers and modulators for high-speed transmission", *IEEE J. Select. Topics in Quantum Electron.*, vol.2, no.2, pp.326-335, 1996.

[20] T.P.Lee, *et al.*, *Electron. Lett.*, vol.20, p.625, 1984.

[21] T.Kato, *et al.*, "DFB-LD/modulator integrated light source by bandgap energy cintrolled selective MOVPE", *Electron. Lett.*, vol.28, pp.153-154, 1992.

[22] Y.Kawamura, *et al.*, "Monolithic integration of a DFB laser and an MQW optical modulator in the 1.5μm range", *IEEE J. Quantum Electron.*, vol.23, pp.915-918, 1987.

[23] A.Ramdane, *et al.*, "Very simple approach for high performance DFB laser-electroabsorption modulator monolithic integration", *Electron. Lett.*, vol.30, pp.1980-1981, 1994.

[24] A.Ramdane, *et al.*, "Monolithic integration of InGaAsP/InP strained layer distributed feedback laser and external modulator by selective quantum well diffusion", *IEEE Photon. Technol. Lett.*, vol.7, pp.1016-1018, 1995.

[25] C.Q.Xu, *et al.*, "1.5μm band efficient broadband wavelength conversion by difference frequency generation in a periodically domain-inverted $LiNbO_3$ channel waveguide", *Appl. Phys. Lett.*, vol.63, p.3559, 1993.

[26] E.Sano, *et al.*, "Lightwave-communication Ics for 10Gb/s and beyond", *OFC'95 Technical Digest*, pp.36-37, 1995, paper Tul1.

[27] K.Y.Lau and N.Bar-Chaim, "High speed digital modulation of ultralow threshold ($< 1mA$) GaAs single quantum laser without bias," *Appl. Phys. Lett.*, **51**(2), pp.69-71, 1987.

[28] K.Shin, M.Tamura, A.Kasukawa, N.Serizawa, S.Kurihashi, S.Tamura, and S.Arai, " Low thershold current density operation of GaInAsP-InP laser with multiple reflector microcavities," *IEEE Photon. Technol. Lett.*, vol. 7, no. 10, pp.1119-1121, 1995.

[29] S.Weisser, E.C.Larkins, K.Czotcher, W.Benz, J.Daleiden, I.Esquivias, J.Fleissner, J.D.Ralston, B.Romero, R.E.Sah, A.Schönfelder, and J.Rosenweig, "Damping-limited modulation bandwidths up to 40 GHz in undoped short-cavity $In_{0.35}Ga_{0.65}As$-GaAs multiple-quantum-well lasers," *IEEE Photon. Technol. Lett.*, vol. 8, no. 5, pp.608-610, 1996.

[30] R.E.Sah, J.D.Ralston, S.Weisser, and K.Eisele, "Characteristics of a two- component chemically-assisted ion-beam etching technique for dry-etching of high-speed multiple quantum well laser mirrors," *Appl. Phys. Lett.*, **67**(7), pp.927-929, 1995.

[31] T. Baba, M. Hamasaki, N. Watanabe, P. Kaewplung, A. Matsutani, T. Mukaihara, F. Koyama, and K. Iga, "A novel short-cavity laser with deep-grating distributed Bragg reflectors," *Jpn. J. Appl. Phys*, vol. 35, pp.1390-1394, 1996.

[32] X.Zhang, A.L.Gutierrez-Aitken, D.Klotzkin, P.Bhattacharya, C.Caneau, and R.Bhat, "0.98μm multiquantum well tunnelling injection lasers with ultra-high modulation bandwidths," *Electron. Lett.*, vol. 32, no. 18, pp.1715-1716, 1996.

[33] A.Yariv, P.Yeh, *Optical Waves in Crystals*, Chap 6, 1984.

[34] R.Jambunathan and J.Singh, "Design studies for distributed Bragg reflectors for short cavity edge emitting lasers," submitted to *IEEE J. Quantum Electronics.*

[35] P.Bhattacharya, J.Singh, H.Yoon, X.Zhang, A.Gutierrez-Aitken, and Y.Lam, " Tunnelling injection lasers: A new class of lasers with reduced hot carrier effects," *IEEE J. Quantum Electron.*, vol. 32, No. 9, pp.1620-1629, 1996.

[36] R.Olshansky, P.Hill, V.A.Lanzisera, and W.Powazinik, "Frequency response of 1.3μm InGaAsP high speed semiconductor lasers," *IEEE J. Quantum Electron.*, vol. QE-23, p.1410-1418, 1987.

[37] R.Nagarajan, T.Fukushima, M.Ishikawa, J.Bowers, R.Geels, L.Coldren, "Transport limits in high-speed quantum well lasers: experiment and theory," *IEEE Photon. Technol. Lett.*, vol. 4, pp.121-123, 1992.

[38] R.Cameron and K.A.McGreer, "Integrated external cavity for tunable devices," *IEEE Photon. Technol. Lett.*, vol. 8, no. 9, pp.1205-1207, 1996.

[39] S.Wang, "Principles of distributed feedback and distributed Bragg reflector lasers", *IEEE J. Quantum Electron.*, vol.10, pp.413-427, 1974.

[40] H.Kogelnik and C.V.Shank, "Coupled mode theory of distributed feedback lasers", *J. Appl. Phys.*, vol.43, no.5, pp.2327-2335, 1972.

[41] H.A.Haus, and C.V.Shank, *IEEE J. Quantum Electron.*, vol.12, p.532, 1976.

[42] K.Sakai, *et al.*, "1.5μm range InGaAsP/InP distributed feedback lasers", *IEEE J. Quantum Electron.*, vol.18, no.8, pp.1272-1278, 1982.

[43] P.J.A.Thijs, *et al.*, "Improved performance 1.5μm wavelength tensile and compressively strained InGaAs/InGaAsP quantum well lasers", in *Tech. Dig. ECOC/IOOC*, Paris, France, Sept. 1991, vol.2, pp.31-38.

[44] J.S.Osinski, *et al.*, "Evidence for gain enhancement in long wavelength strained quantum well laser diodes", *Electron. Lett.*, vol.27, pp.469-470, 1991.

[45] J.S.Osinski, *et al.*, "Low-threshold-current-density 1.5μm lasers using compressively strained InGaAsP quantum wells", *IEEE Photon. Technol. Lett.*, vol.4, pp.10-13, 1992.

[46] C.E.Zah, *et al.*, "1.5μm compressively-strained multiple-quantum-well 20-wavelength distributed feedback laser arrays", *Electron. Lett.*, vol.28, pp.824-826, 1992.

[47] H.Okuda, *et al.*, "Five-wavelength integrated DFB laser arrays with quarter-wave-shifted structures", *IEEE J. Quantum Electron.*, vol.23, pp.843-848, 1987.

[48] C.E.Zah, *et al.*, "1.5μm tensile-strained single quantum well 20-wavelength distributed feedback laser arrays", *Electron. Lett.*, vol.28, pp.1585-1587, 1992.

[49] M.Nakao, *et al.*, "Distributed feedback laser arrays fabricated by synchrotron orbital radiation lithography", *IEEE J. Select. Areas Commun.*, vol8, pp.1178-1182, 1990.

[50] M.Tennant, *et al.*, "Multiwavelength distributed Bragg reflector laser array fabricated using near field holographic printing with an electron-beam generated phase grating mask", *J. Vac. Sci. Technol.*, vol.B11, pp.2509-2513, 1993.

[51] C.E.Zah, *et al.*, "Integration of a multi-wavelength compressively-strained multi-quantum-well distributed feedback laser array with a star coupler and optical amplifier", *Electron. Lett.*, vol28, pp.2361-2362, 1992.

[52] J.Werking, *et al.*, "Methane/hydrogen-based reactive ion etching of InAs, InP, GaAs and GaSb", *Appl. Phys. Lett.*, vol.58, pp.2003-2005, 1991.

[53] H.Soda, *et al.*, "Design of DFB lasers for high power single-mode operation", *Electron. Lett.*, vol.22, no.20, pp.1047-1049, 1986.

[54] H.Soda, *et al.*, "Stability in single longitudinal mode operation in GaInAsP/InP phase-adjusted DFB lasers", *IEEE J. Quantum Electron.*, vol.23, pp.804-814, 1987.

[55] S.Hanamann, "Transfer matrix analysis of the spectral properties of complex distributed feedback laser structures", *IEEE J. Quantum Electron.*, vol.28, pp.2589-2595, 1992.

[56] H.Millmer, *et al.*, "Tailored DFB laser properties by individulally chirped gratings using bent waveguides", *IEEE J. Select. Quantum Electron.*, vol.1, no.2, pp.356-362, 1995.

[57] S.Ogita, *et al.*, "FM response of narrow-linewidth multielectrode $\lambda/4$ shift DFB lasers", *IEEE Photon. Technol. Lett.*, vol.2, pp.165-166, 1990.

[58] M.Tohyama, *et al.*, "Wavelength tuning mechanism in three-electrode DFB lasers", *IEEE Photon. Technol. Lett.*, vol.5, pp.616-618, 1993.

[59] G.C.Wilson, *et al.*, "Integrated electroabsorption modulator/DBR laser linearized by RF current modulation", *IEEE Photon. Technol. Lett.*, vol.7, no.10, pp.1154-1156, 1995.

[60] K.Kawano, *et al.*, "Design of InGaAs-InAlAs multiple-quantum-well (MQW) optical modulators", *IEEE J. Quantum Electron.*, vol.28, no.1, pp.224-230, 1992.

[61] T.Ido, *et al.*, "Performance of strained InGaAs/InAlAs multiple-quantum-well electroabsorption modulators", *IEEE J. Lightwave Tech.*, vol.14, no.10, pp.2324-2331, 1996.

[62] Y. Yuan, X. Zhang, and P. Bhattacharya, "Low Photocurrent GaAs/$Al_{0.3}Ga_{0.7}As$ Multiple Quantum Well Modulators with Selective Erbium Doping", *IEEE Photonics Technology Letters*, **vol.8, No.12**, *pp.1638-1640*, December, 1996.

[63] T.Ido, *et al.*, "Ultr-high-speed multiple-quantum-well electro-absorption optical modulators with integrated waveguides", *IEEE J. Lightwave Tech.*, vol.14, no.9, pp.2026-2034, 1996.

[64] I.K.Czajkowski, *et al.*, "Strained-compensated MQW electroabsorption modulator for increased optical power handling", *Electron. Lett.*, vol.30, no.11, pp.900-901, 1994.

[65] M.Suzuki, *et al.*, "Effect of hole plie-up at heterointerface on modulation voltage in GaInAsP electroabsorption modulators", vol.25, no.2, pp.22-23, 1989.

[66] P.K.Bhattacharya, *Semiconductor Optical Devices*, Prentice Hall, 1994.

[67] J.Singh, *Physics of Semiconductors and Their Heterostructures*, McGraw-Hill, 1993.

[68] A.C.Gossard, "Growth of microstructures by molecular beam epitaxy", *IEEE J. Quantum Electron.*, vol.22, p.1649, 1986.

[69] M.J.Ludowise, "Metalorganic chemical vapor deposition of III-V semiconductors", *J. Appl. Phys.*, vol.58, vol.R31, 1985.

[70] T.Wood, "Multiple quantum well modulators", *IEEE J. Lightwave Tech.*, vol.6, no.6, pp.743-757, 1988.

[71] R.Sahara, *et al.*, "Engineering of barrier band structure for electroabsorption MQW modulators", *Electron. Lett.*, vol.30, no.9, pp.698-699, 1994.

[72] K.Sato, *et al.*, "Strained InGaAsP multiquantum wells for optical electroabsorption waveguide modulators", *Electron. Lett.*, vol28, no.7, pp.609-610, 1992.

[73] M.Chin, *et al.*, "Theoretical design optimization of multiple-quantum-well electroabsorption modulators", *IEEE J. Quantum Electron.*, vol.29, no.9, pp.2476-2488, 1993.

[74] S.Schmitt-Rink, D.S.Chemla, and D.A.B.Miller, *Phys. Rev.*, **B32**, p.6601, 1985; *Adv. Phys.*, **38**, p.89, 1989.

[75] K.Wakita, *et al.*, "High-speed InGaAlAs/InAlAs multiple quantum well optical modulators", *IEEE J. Lightwave Tech.*, vol.8, no.7, pp.1027-1031, 1990.

[76] K.Satzke, *et al.*, "Ultrahigh-bandwidth (42GHz) polarisation-independent ridge waveguide electroabsorption modulator base[on tensile strained InGaAsP MQW", *Electron. Lett.*, vol31, no.23, pp.2030-2032, 1995.

[77] S.Kondo, *et al.*, "Fabrication of a polarization insensitive electroabsorption modulator with strained InGaAs/InAlAs MQW by MOVPE", *IPRM 1995*, paper WA2.4, pp.61-64.

[78] T. K. Woodward, W. H. Knox, B. Tell, A. Vinattieri, and M. T. Asom,"Experimental studies of proton-implanted GaAs-AlGaAs multiple-quantum-well modulators for low-photocurrent applications", *IEEE J. Quantum Electron.*, **30**, pp.2854-2865, 1994.

[79] S. Sethi, S. Gupta, and P. K. Bhattacharya,"Picosecond carrier lifetime in erbium-doped -GaAs", *Appl. Phys. Lett.*, **62**, pp.1128-1130, 1993.

[80] S. Sethi, and P. K. Bhattacharya,"Characteristics and device applications of erbium doped III-V semiconductors grown by molecular beam epitaxy", *J. Electron. Mater.*, **25**, pp.467-477, 1996.

[81] S. Sethi, *Ph.D. Dissertation*, **Univ. of Michigan**, 1995.

[82] C. J. Palmstrom, S. Mounier, T. G. Finstad, and P. F. Miceli,"Lattice-matched $Sc_{1-x}Er_xAs$/GaAs heterostructures: A demonstration of new systems for fabricating lattice-matched compounds to semiconductors", *Appl. Phys. Lett.*, **56**, pp.382-384, 1990.

[83] A. R. Peaker, H. Efoglu, J. M. Langer, A. C. Wright, I. Pool, and K. E. Singer," Erbium doped gallium arsenide a self-organizing low dimensional system", *Proceedings of the 1993 Materials Research Society Spring Meeting*, San Francisco, April, pp.337-345, 1993.

[84] M.B.Chang and E.Garmire, *IEEE J. Quantum Electron.*, **QE-16**, 997, 1980.

[85] L.A.Coldren, B.I. Miller, K.Iga, and J.Renstshler, *Appl. Phys. Lett.*, **38**, 315, 1981.

[86] W.T.Tsang, N.A.Olsson, R.A.Linke, and R.A.Logan, *Electron. Lett.*, **19**, 415, 1983.

[87] T. P. Lee, C. A. Burrus, W. B. Sessa, and P. Besomi, "Q-switching cleaved-coupled- cavity laser with an integrated intracavity modulator", *Electron. Lett.*, **20**, 1, 1984.

[88] T. P. Lee, C. A. Burrus, G. Eisenstein, W. B. Sessa, and P. Besomi, "Amplifier-modulator integrated with a cleaved-coupled-cavity injection laser", *Electron. Lett.*, **20**, 625, 1984.

[89] W. T. Tsang, *Semiconductors and Semimetals.* New York: Academic Press, 1985.

[90] L.A.Coldren, F.Furuya, B.I.Miller, and J.A.Rentschler, *IEEE J. Quantum Electron.*, **QE-18**, 1679, 1982.

[91] G. P. Agrawal,N. K. Dutta, *Semiconductor Lasers*, 2nd Edition Van Nostrand-Reinhold, 1993.

[92] K.Kurokawa, *IEEE Trans. Microwave Theory Tech.*, **MTT-13**, 194, 1965.

[93] K. S. Yee, "Numerical solution of initial boundary value problem, involing Maxwell's equations", IEEE Trans. Antennas Propag., **AP-14**, 302, 1966.

[94] S. T. Chu and S. K. Chandhuri, "A finite difference time-domain method for the design and analysis of guide-wave optical structures", *IEEE J. Lightwave Tech.*, **7**, 2033, 1989.

[95] R.Y. Chan and J.M. Liu, "Time-domain wave propagation in optical structures", *IEEE Photon. Technol. Lett.*, **6**, 1001, 1994.

[96] Y.Yuan, R. Jambunathan, P. Bhattacharya, and J. Singh, "Finite Difference Time Domain Analysis and Experimental Examination of the Performance of a Coupled Cavity MQW Laser/Active Waveguide at 1.54μm", *IEEE Journal of Quantum Electronics*, pp.408-415, March, 1997.

[97] P.J.A.Thijs, L.F.Tiemeijer, J.J.M.Binsma, and T.Dongen, "Progress in long-wavelength strained-layer InGaAs(P) quantum-well semiconductor lasers and amplifiers", *IEEE J. Quantum Electron.*, **30**, pp.477-499, 1994.

[98] J. M. Luttinger and W. Kohn, "Motion of electrons and holes in perturbed periodic fields", *Physical Review*, **97**, pp. 869-883, 1955.

[99] P. Lawaetz, "Valence-band parameters in cubic semiconductors", *Phys. Rev. B*, **4**, pp. 3460-3467, 1971.

[100] J. Singh, *Physics of Semiconductors and Their Heterostructures*, Chapter 7. New York: McGraw-Hill (1993).

[101] J. P. Loehr and J. Singh, "Theoretical studies of the effect of strain on the performance of strained quantum well lasers based on GaAs and InP technology", *IEEE J. Quantum Electron.*, **27**, pp. 708-716, 1991.

[102] P. McIloy, K. Kurobe, and Y. Uematsu, "Analysis and application of theoretical gain curves to the design of multi-quantum well lasers", *IEEE J. Quantum Electron.*, **21**, 1958, 1985.

[103] J. Wilcox, G. Peterson, S. Ou, J. Yang, M. Jansen, and D. Schechter, "Gain- and threshold-current dependence for multiple-quantum-well lasers", *J. Appl. Phys.*, **64**, 6564, 1988.

[104] G. P. Agrawal,N. K. Dutta, *Semiconductor Lasers*, 2nd Edition Van Nostrand-Reinhold, 1993.

[105] K. Wakita,and I. Kotaka, "Multiple-quantum-well optical modulators and their monolithic integration with DFB lasers for optical fiber communications", *Microwave and Optical Technol. Lett.*, **7**, 120, 1994.

[106] M. Aoki, M. Suzuki, M. Takahashi, H. Sano, T. Ido, T. Kawano, and A. Takai, "High speed and low drive voltage InGaAs/InGaAsP MQW electroabsorption modulator integrated DFB laser with semi-insulating buried heterostructure", *Electron. Lett*, **28**, 1157, 1992.

[107] M. Allovon, S. Fouchet, J. Harmand, A. Ougazzaden, B. Rose, A. Gloukhian, and F. Devaux, "Monolithic integration on InP 1.55 μm laser", *IEEE Photon. Technol. Lett.*, **7**, 185, 1995.

[108] M. Aoki, M. Suzuki, H. Sano, T. Kawano, T. Ido, T. Taniwatari, K. Uomi, and A. Takai, "InGaAs/InGaAsP MQW electroabsorption modulator integrated with a DFB laser fabricated by band-gap energy control selective area MOCVD", *IEEE J. Quantum Electron.*, **29**, 1993.

[109] I. Kotaka, K. Wakita, M. Okamoto, H. Asai, and Y. Kondo, "A low-drive-voltage, high-speed monolithic MQW modulator/DFB laser light source", *IEEE Photon. Technol. Lett.*, **5**, 61, 1993.

[110] T. Wood, J. Pastalan, C. Burrus, B. Johnson, B. Miller, J. deMiguel, U. Koren, and M. Young, "Electric field screening by photogenerated holes in multiple

quantum wells: A new mechanism for absorption saturation", *Appl. Phys. Lett.*, **57**, 1081, 1990.

[111] K.Y.Liou, *et al.*, "A 5Gb/s monolithically integrated lightwave transmitter with 1.5μm multiple quantum well laser and HBT driver circuit", *IEEE Photon. Technol. Lett.*, vol3, no.10, pp.928-930, 1991.

[112] D.B.Slater Jr., *et al.*, "Monolithically integrated SQW laser and HBT driver via selective OMVPE regrowth", *IEEE Photon. Technol. Lett.*, vol.5, no.7, pp.791-794, 1993.

[113] M.Suzuki, *et al.*, "Electrical and optical interactions between integrated InGaAsP/InP DFB lasers and electroabsorption modulators", *IEEE J. Lightwave Tech.*, vol.6, no.6, pp.779-784, 1988.

[114] D.Marcuse, *et al.*, "Time-dependent simulation of a laser-modulator combination", *IEEE J. Quantum Electron.*, vol.30, no.12, pp.2743-2755, 1994.

[115] D.Marcuse, *et al.*, "Simulation of a laser modulator driven by NRZ pulses", *IEEE J. Lightwave Tech.*, vol.14, no.5, pp.860-866, 1996.

[116] D.R.Pehlke, *Ph.D. Dissretation*, The University of Michigan, 1994.